Environmental & Engineering Geoscience

EDITORS

Abdul Shakoor
Kent State University
Kent, OH 44242
ashakoor@kent.edu

Eric Peterson
Department of Geography, Geology, and the Environment
Illinois State University
Normal, IL 61790
309-438-5669
ewpeter@ilstu.edu

Karen E. Smith, Editorial Assistant, kesmith6@kent.edu

Submitting a Manuscript

Cover photo

Looking southwest towards Trinidad, CA (Trinidad Head can be seen in the upper left corner), narrow strips of tree retention, known as Watercourse Lake Protection Zones (WLPZ) or Riparian Management Zones (RMZ), are intended to protect and preserve wildlife habitat. Coincidently, these areas are typically located in the most landslide-prone areas on the landscape and, thus, help prevent management-related mass wasting. Riparian buffers were first implemented as part of the Forest Practice Act in 1973 and have evolved over time. Photo by Jason Woodward, June 20, 2019. See article on page 115.

Environmental & Engineering Geoscience

Table of Contents

Using an Inventory of Unstable Slopes to Prioritize Probabilistic Rockfall Modeling and Acid-Base Accounting in Great Smoky Mountains National Park

THOMAS O'SHEA

Bunnell Lammons Engineering, 6004 Ponders Court, Greenville, SC 29615

SAMANTHA FARMER

Virginia Department of Transportation, 870 Bonham Road, Bristol, VA 24201

ARPITA NANDI*

Department of Geosciences, East Tennessee State University, Johnson City, TN 37614

ERIC BILDERBACK

National Park Service, Geologic Resources Division, P.O. Box 25287, Denver, CO 80225

INGRID LUFFMAN
ANDREW JOYNER

Department of Geosciences, East Tennessee State University, Johnson City, TN 37614

Key Terms: *Unstable Slope Management Program, Kernel Density Estimation, Probabilistic Rockfall Simulations, Acid-Base Accounting, Great Smoky Mountains National Park*

ABSTRACT

An important first step in the geotechnical asset management of Great Smoky Mountains National Park (GRSM) is the creation of an unstable slope inventory along major transportation corridors. Slope-stability problems are frequent in GRSM, often initiated in highly weathered and fractured metasedimentary rocks. In this study, an unstable slope inventory was created using the Unstable Slope Management Program for Federal Land Management Agencies protocols. Hazards and risks were evaluated for 285 unstable slopes along 243.67 km of roadway. Kernel density estimation was used to identify unstable slope hotspots and establish 14 sites for site-specific investigations to evaluate potential impacts of discrete unstable slopes along major roadways. Two-dimensional probabilistic rockfall simulations and acid-base accounting tests were used to predict rockfall pathways and evaluate the acid-producing potential of rocks. Simulations indicated that rock material would likely enter the roadway at all 14 sites. Acid-base accounting test results indicated that slaty rocks of the Anakeesta Formation and graphitic schist of the Wehutty Formation are primary acid-producing rocks in rockfall-prone areas. This research illustrates an approach for prioritizing areas for site-specific investigations towards the goal of improving safety in GRSM, including developing mitigation strategies for rockfall by widening ditches, installing barriers, and encapsulating acidic rockfall material.

INTRODUCTION

The terms slope failure and landslide are often used interchangeably to describe a wide variety of natural geomorphic processes that result in downward movement of earth materials, including rock, soil, artificial fill, or a combination of these (Varnes, 1978; Turner and Schuster, 1996). The different types of slope failures can be distinguished based on the nature of materials involved and their movement. Failures occur frequently in the mountainous terrains of the United States (e.g., Colorado Plateau, Appalachian Mountains, Coastal Ranges of California, Southern Rocky Mountains, Pacific Northwest Coast Range of Oregon and Washington, Olympic Mountains, and Cascade

*Corresponding author email: nandi@etsu.edu
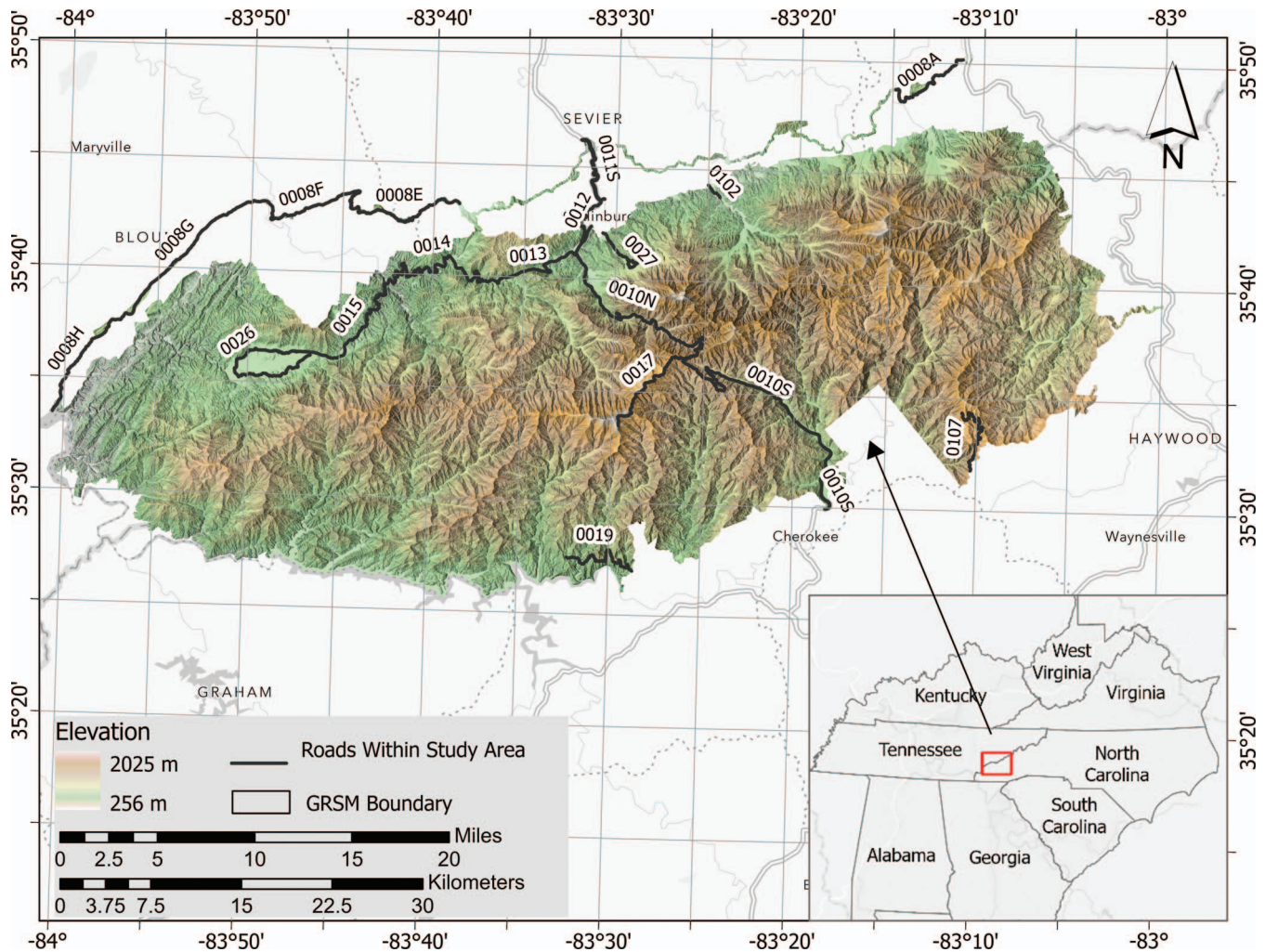
Figure 1. Major transportation corridors in Great Smoky Mountains National Park, TN and NC.

Range) and range from small rockfalls or slope creep to complex landslides, rock avalanches, and debris flows. The behaviors and outcomes of slope-failure events will vary based on their location and many underlying factors. For example, in the Pacific Northwest region, failure events are mostly triggered by rainfall, earthquakes, or volcanic activities (Wieczorek and Leahy, 2008). In the Appalachian Mountains, including the Great Smoky Mountains National Park (GRSM), slope failures result from complex interactions among various rock and soil types, joint geometries, precipitation duration and intensity, topographic profiles, and hydrological conditions (Wieczorek et al., 2000; Moore, 2004; and Nandi and Shakoor, 2017).

Unstable Slope Failures in GRSM

Great Smoky Mountains National Park straddles the border of North Carolina (NC) and Tennessee (TN), covering an area of more than 500,000 acres (Figure 1) (NPS, 2019). The park is the most visited park of the 62 national parks in the United States, accommodating more than 14 million visitors in 2021 (NPS, 2021). The park generates more than $1.05 billion in visitor spending and provides employment for more than 15,000 people in local communities (Cullinane and Koontz, 2020). Each year, unanticipated road closures due to slope-failure events occur within the park. These events interfere with park objectives and have a significant negative economic impact on the regional economy (Anderson and Cuelho, 2017). For example, in 2013, heavy rainfall in the GRSM resulted in a landslide needing about $4 million for repair. Smaller-scale slope failures related to maintenance costs are frequent and range from $25,000 to $200,000, excluding added vehicle and emissions costs, travel time, and maintenance of detour routes (according to correspondence with GRSM maintenance personnel).

Large-scale landslides are not common along the GRSM transportation corridors, but when they do oc-

cur, they can completely or partially close the road network, causing economic loss as well as social costs. When the ground conditions are favorable, rainfall from cloudbursts, hurricanes, and storms can trigger fast-moving flows (Wieczorek et al., 2000). Bogucki (1976) identified numerous rockslides and debris flows in GRSM during a September 1951 rainstorm. About 50 percent of the debris flows from those slides occurred in the Mount Le Conte–Sugarland Mountain area and Alum Cave Creek watershed, significantly damaging the roads and hiking trails. More than 60 percent of the debris flows happened on slate and phyllite of the Anakeesta Formation, and the rest occurred on metasandstone of the Thunderhead Formation (Bogucki, 1976). In 2010, three rockfall events occurred on roads that serve GRSM park visitors. The largest and most disruptive failure event occurred on January 25, 2010, along a southbound section of Route 0011S (Gatlinburg Spur), an arterial access route within the park. As a result, both southbound lanes of the spur were closed for more than 30 days (TDOT, 2010a). Though the Tennessee Department of Transportation (TDOT) was responsible for $700,000 in emergency expenditure and cleanup for the January 25, 2010, rockslide, each event also posed a risk to GRSM park visitors who frequently travel along this route (TDOT, 2010b). A recent slide, close to the Trout Branch tributary of Little Pigeon River, transformed into a debris flow in August 2012 and damaged the Alum Cave trail (Nandi and Shakoor, 2017). A heavy rainfall event in January 2013 triggered a large cut-slope embankment slope failure and created a large landslide that destroyed about 200 m (~600 ft) of Route 0010S (Newfound Gap Road or U.S. Route 441) in the GRSM towards NC, a major economic commerce corridor for communities on either side of the park (USGS, 2013). Regrettably, slope-failure events in the park have led to fatalities. On August 1, 2019, a man was killed by a fallen tree on the Gatlinburg Spur where multiple rockslides occurred following heavy rainfall. According to a local news station, more than 10 cm (4 four in.) of rain fell in just over 1 hour, which triggered the event (Cherokee One Feather, 2019).

In 2008, the National Park Service (NPS) published its most recent *Great Smoky Mountains National Park Geologic Resource Evaluation Report*. The report compiled information related to geologic issues (e.g., erosion and slope processes, abandoned mines, air and water quality) as well as geologic features and processes (e.g., major faults, views, tectonic windows). The report was designed to be used by park officials, scientific researchers, conservation and environmental constituencies, and the public. A section related to geohazards can be found in the report. However, it does not provide a usable database for tracking potential geo-

Table 1. *Paved roads at GRSM, within the study area, where route ID corresponds to the road designations.*

Road Name	Route ID	Total Route Length in km (mi)
Foothills Parkway	0008A,E,F,G,H	60.11 (37.35)
Newfound Gap Road or U.S. 441	0010N,S	51.43 (31.96)
Gatlinburg Spur Road	0011N,S	13.53 (8.41)
Gatlinburg Bypass Road and Ramps	0012ZZ	7.48 (4.65)
Fighting Creek Gap Road and Spur	0013ZZ	8.07 (5.02)
Little River Gorge Road	0014	20.31 (12.62)
Laurel Creek Road	0015	12.54 (7.79)
Clingmans Dome Access Road	0017	11.15 (6.93)
Elkmont Road	0018	2.46 (1.53)
Lakeview Drive East	0019	9.48 (5.89)
Cades Cove Loop Road	0026	16.24 (10.09)
Cherokee Orchard Road	0027	5.83 (3.62)
Greenbrier Road	0102	7.83 (4.87)
Heintooga Ridge Road	0107	8.59 (5.34)
Roaring Fork Motor Nature Trail	0150	8.59 (5.34)
Total Mileage in Study Area:		243.67 (151.41)

hazard sites along park routes (Thornberry-Ehrlich, 2008).

The NPS is responsible for operating and maintaining 510 km (315 mi) of roadway within GRSM boundaries, 243.67 km (151.41 miles) of which are paved (NPS-GRSM, 2014, Figure 1 and Table 1. Significant roads within the park include: Route 0008 A, E, F, G, and H (Foothills Parkway), Route 0010 N and S (Newfound Gap Road or U.S. Route 441), Route 0011 N and S (Gatlinburg Spur), Route 0014 (Little River Gorge Road), Route 0015 (Laurel Creek Road), Route 0017 (Clingmans Dome Access Road), Route 0019 (Lakeview Drive East), Route 0026 (Cades Cove Loop Road), Route 0105 (Cherokee Orchard Road), and Route 0107 (Heintooga Ridge Road). Figure 2 shows the current conditions of some representative slopes in the park. Several paved roads that traverse mountainous terrain serve not only park visitors, but also local and regional traffic. After nearly 80 years of use on some roads, GRSM's transportation corridors require effective long-term management (Anderson, 2016). NPS has recognized the need to implement a proactive, risk-based strategic unstable slope management approach for GRSM transportation routes in the face of fluctuating annual budgets and aging geotechnical assets that become more unstable as they are continually exposed to the environment.

Transportation Corridor Risk Assessment

Roadway and trail slopes are transportation or geotechnical assets, and their reliable performance

Figure 2. Current slope condition photos in (a) Newfound Gap (0010N), (b) Little River Gorge (0014), (c) Gatlinburg Spur (0011S), and (d) Clingmans Dome (0017).

helps the transportation system to operate safely. These assets have a life cycle; if the slopes fail, the cost of repair can be much greater than periodically intervening with risk-reduction improvements. Unfortunately, the slope assets are often overlooked until they directly damage and impact the transportation system. Risk-based geotechnical asset management (GAM) is fundamental for slope maintenance; it reduces risk, improves system performance, and, if actively managed, can reduce slope life-cycle costs and improve safety (Stanley, 2011; Anderson, 2016). To help foster GAM, federal and various state departments of transportation have developed roadway unstable slope, landslide hazard, and/or rockfall rating systems to rate high- and low-hazard areas. This information allows departments to prioritize areas of concern for slope failure. At the federal level, a platform introduced in 2019 known as the Unstable Slope Management Program for Federal Land Management

Agencies (USMP for FLMA) has gained much recognition (Beckstrand et al., 2019). USMP for FLMA is designed to guide efforts by federal land management agencies (FLMAs) and lower-traffic-volume transportation departments to assess slope hazards and risks along transportation corridors in order to achieve their own transportation maintenance goals and objectives (Anderson and Cuelho, 2017; Stanley and Anderson, 2017; and Beckstrand et al., 2019). USMP includes management tools that are important components of any GAM program, such as: condition assessments, examples of performance measures, and quantitative risk assessment (QRA) prioritization techniques (Beckstrand et al., 2019). The program was formulated by adopting and adapting methods from accepted transportation asset management practices used for bridges, pavement, etc., as well as existing GAM programs such as Oregon's rockfall hazard rating system (RHRS) and Alaska's USMP (Thompson,

2017). Alaska's USMP, which built upon progress made by programs like Oregon's RHRS, was completed in 2009 and provided a model for stakeholders (NPS, U.S. Forest Service [USFS], Bureau of Land Management [BLM], Bureau of Indian Affairs [BIA], and Western Federal Lands Highway Division [WFL]) to develop the USMP for FLMA (Beckstrand et al., 2019).

National parks, including Acadia, Crater Lake, Denali, GRSM, Hawaii Volcanoes, Olympic, Yellowstone, Yosemite, and Zion, have begun utilizing USMP for FMLA by performing slope condition hazard and risk assessments. Additional NPS units such as Vicksburg National Military Park, Delaware Water Gap National Recreation Area, and the Heritage Partnerships Program of the NPS Intermountain Region have also begun using the USMP for FMLA. Positive outcomes from proactively managing geotechnical assets are becoming clearer as growing numbers of organizations utilize the program. Recently, Bauer et al. (2021) and Banks et al. (2021) utilized the USMP to rate the unstable slopes along the Blue Ridge Parkway and suggested best practices based on the experiences gained from the extensive mapping. Researchers in Zion National Park concluded that reactive management can be four to five times more expensive for rockfall events than proactive management (FHWA, 2020). Additionally, Capps et al. (2017) concluded that QRAs are critical to understanding where funds should be allocated to avoid the common mistake of fixing the "worst first" reconstruction-only policy, which occurs when funding is spent without careful consideration of the exposure to associated risks. This conclusion was supported by the findings of Beckstrand et al. (2017), which estimated a value of $19.7 billion for the state of Alaska's geotechnical assets, i.e., more than three times greater than the value of their bridge inventory based on current reconstruction costs. The technical report estimated that managing these assets using a preservation model would reduce overall life-cycle costs by 5 percent (Beckstrand et al., 2017).

Objective of Study

With the goal of managing geotechnical assets along roadways, this research evaluated slope-failure risk along the primary GRSM transportation corridors to determine how to prioritize limited financial resources for risk-reduction maintenance or full-mitigation-level work. As such, the specific research objectives were to (1) create an inventory of unstable slopes and associated transportation-related hazards and risk ratings using USMP organized in a geospatial database, (2) delineate unstable slope hotspot areas that have high likelihood of roadway interruption using geospatial analysis, (3) perform site-specific investigations that predict roadways susceptible to unstable slope impact using probabilistic simulations, and (4) perform site-specific acid-base accounting (ABA) tests to evaluate the acid-producing potential (APP) of waste rock from slope failures.

The inventory of unstable slopes along with the hazards and risk rating digital geodatabase and maps will enable GRSM officials to take steps towards prioritizing maintenance and mitigation efforts using cost-benefit analyses based on short- and long-term budgets. The research provides an example of high-risk unstable slope prioritization using data-driven hotspot analysis, and application of USMP to provide a geologic and environmental framework for site-specific slope remediation to maintain the integrity of roadways in GRSM.

Study Area

Most of GRSM is in the Western Blue Ridge Physiographic Province, with a limited area in the Tennessee Valley and Ridge Physiographic Province to the northwest (Southworth et al., 2012). Bounded to the south by series of en echelon zones collectively called the Swannanoa Lineament, the park is home to some of the highest peaks in the eastern United States, some of which reach more than 2,025 m (6,644 ft) above adjacent valley floors. In some areas of the park, mountain slopes may be as great as 44° (Southworth et al., 2012; Hill, 2018). Much of GRSM is within the highlands of the Western Blue Ridge Physiographic Province, which is composed primarily of Neoproterozoic metasedimentary rocks of the Snowbird Group and Great Smoky Group (Southworth et al., 2012) (Figure 3). The northwestern portion of the park is within the foothills of the Western Blue Ridge Physiographic Province, which is characterized by rolling hills. The foothills are primarily low-grade greenschist facies or have not been metamorphosed and range from Neoproterozoic to Early Ordovician in age (Southworth et al., 2012). Quaternary deposits of alluvium and colluvium occur in low-lying areas of the park, along drainage features, or along the base of cliffs and slopes.

Along Route 0010, the primary rock formations encountered included metasandstone of the Thunderhead Formation and slate and metasiltstone of the Anakeesta Formation. Metasandstone of the Thunderhead Formation, Metcalf Phyllite, and Pigeon Siltstone and metasandstone of the Elkmont Formation were encountered along Routes 0013, 0014, and 0015. Route 0011 is mainly composed of Roaring Fork Formation metasandstone and the Pigeon Siltstone.
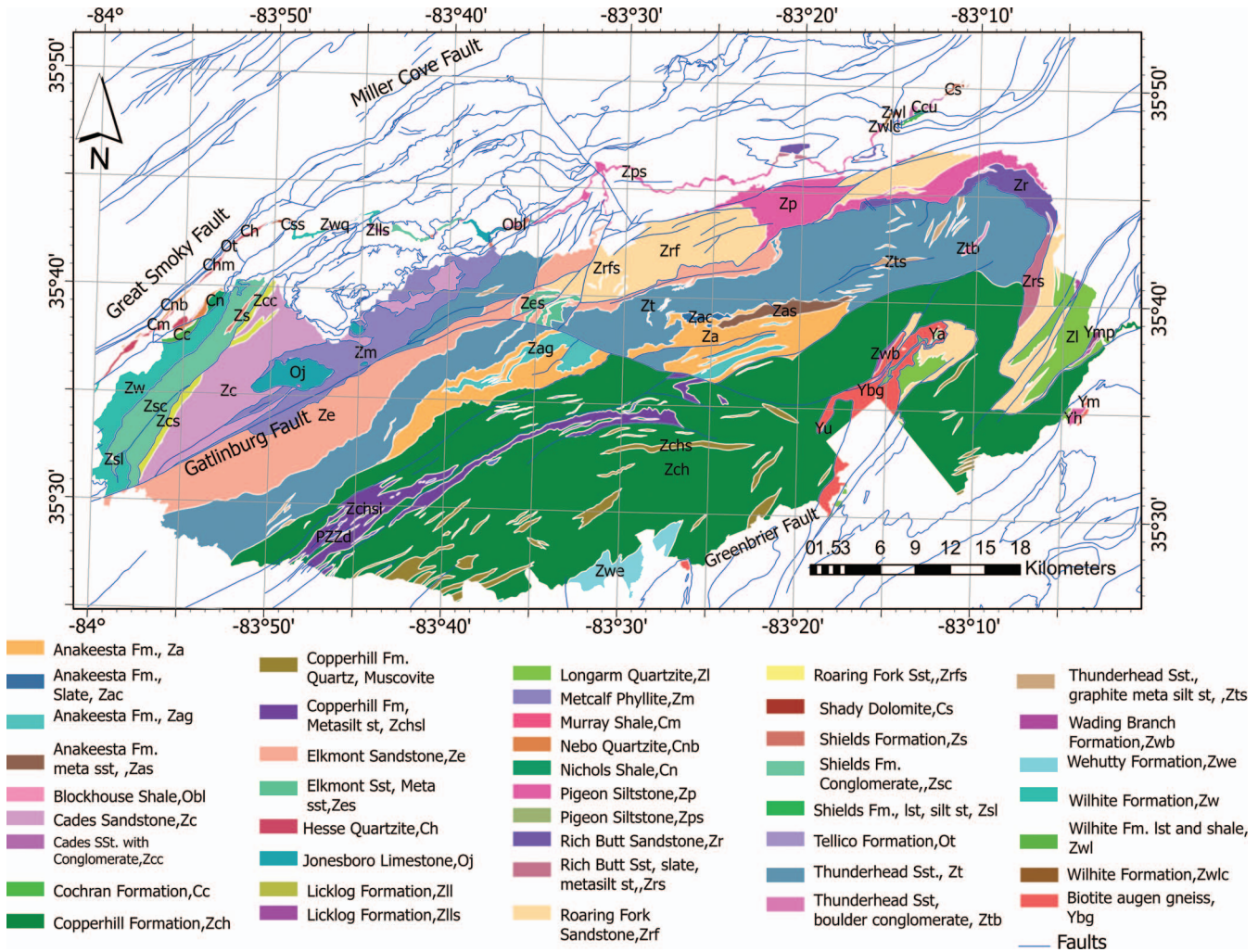
Figure 3. Geology and major faults in Great Smoky Mountains National Park.

Route 0008 (H, G, F, and E) crosses Hesse Quartzite, Wilhite Formation phyllite, and conglomerate, sandstone, and slate of the Shields Formation. Route 0019 traverses mostly through Wehutty Formation, consisting of slate graphitic and sulfidic schist. The Anakeesta, Wehutty, and part of the Copperhill formations are prime examples of acid-producing rock because they contain sulfide minerals such as pyrite and little or no carbonate minerals. GRSM is dominated by four major structural systems: (1) The Greenbrier and Dunn Creek faults in the highlands and foothills, (2) the Miller Cove and Great Smoky thrust faults in the foothills, (3) the Gatlinburg and Pigeon Forge faults in the foothills, and (4) the thrust sheets of the Tennessee Valley, which are bounded by the Pine Mountain Thrust Fault and the Great Smoky Fault (Thornberry-Ehrlich, 2008; Southworth et al., 2012). Most of the major faults are part of a connected fault system and

can be a source of rockslides (Southworth et al., 2012) (Figure 3).

Annual rainfall throughout the park ranges from 1.14 m (45 in.) to 2.41 m (95 in.). Most of the primary roads are in the 1.50 m (59 in.) to 2.06 m (81 in.) range, and in higher sections of the park, over 2.16 m (85 in.) of precipitation falls annually (NPS-GRSM, 2017). More slope movements are expected to occur during early spring and late fall, when frost wedging conditions and large storm events create ideal slide conditions (Matsuoka, 2001; Sass, 2005; and Nandi and Shakoor, 2017). Over 3,379 km (2,100 mi) of streams and rivers are contained within GRSM, of which 1,175 km (730 mi) are fish-bearing and 2,092 km (1,300 mi) are tributaries (NPS-GRSM, 2017). Tributaries, springs, and precipitation replenish waterfalls and surface streams (McKenna, 2007). GRSM streams are vulnerable to acid rain because of

nearby power plants, factories, and volume of traffic (McKenna, 2007). Water in GRSM can be acidic from pollutants in rain, and from rock formations that have acid-producing potential (e.g., Anakeesta Formation, Copperhill Formation, Wehutty Formation). Schaeffer and Clawson (1996) conducted geologic mapping, petrographic analysis, and ABA tests as part of a road and transmission line construction project in southwestern NC, where the acid-producing rocks of interest included Anakeesta Formation graphitic schist and thin layers of sulfidic rock within the Ammons Formation, both of which are present in GRSM. The construction project required the use of an encapsulating embankment design similar to several large highway projects in the Blue Ridge Physiographic Province in TN and NC to prevent acid drainage (Byerly, 1996; Schaeffer and Clawson, 1996). Their study exemplifies the special handling required for acid-producing material to minimize acid rock drainage (ARD) and avoid costly mitigation of adverse environmental impacts (Byerly, 1996). The potential negative impacts on physical infrastructure and surface waters illustrate how evaluation of the acid-producing potential at rockfall prone cut slopes can help to inform waste rock management strategies and why ARD represents an important consideration for the GAM strategy in GRSM. A study by Mathews and Morgan (1982) showed the adverse effect of ARD on aquatic life: The salamander (*Leurognathus marmoratus*) population was almost destroyed downstream from the highway cut-and-fill areas due to the presence of sulfide minerals in the Anakeesta Formation. These rock types are more prone to rockfalls and landslides, and they also have the potential to negatively impact flora and fauna via acidification of waters (Schaeffer and Clawson, 1996; Latham et al., 2009).

METHODS

This study utilized the USMP for FLMA protocols to develop a digital database of unstable slopes and their current conditions along 243.67 km (151.41 mi) of road in GRSM. Site investigation field data were added to a geodatabase in ArcGIS Pro 2.7 and analyzed to better understand the spatial distribution of unstable slopes. Kernel density estimation (KDE) was used to identify clusters of unstable slopes with high likelihood of roadway disruption and establish study areas for site selection. Two-dimensional probabilistic slope stability simulations and ABA tests were used to predict unstable slope pathways and evaluate the acid-producing potential of rock fragments. The study methods are displayed in a flowchart (Figure 4) and described in the following sections.

Data Collection and Preparation of the Geodatabase

Primary data were collected using the USMP for FLMA standardized field form that organizes hazard and risk data into discrete attributes and quantifies the observations (Capps et al., 2017; Beckstrand et al., 2019). The protocols can be used to assess several types of unstable slopes, such as soil and rock landslides, rockfalls, debris flows, and thaw-unstable slopes (Capps et al., 2017). Site assessments ranged from July 2019 to July 2020. A field rating was conducted for each unstable slope using the USMP for FLMA rating form, which included parameters listed in Table 2. Photographs of each slope and global positioning system (GPS) coordinates were also collected, and site data were uploaded to the USMP.info web portal. Preliminary and total USMP ratings were calculated based on the hazard and risk parameters as indicated by FHWA (2020) observed in the field or reported by park officials.

Secondary data were acquired as spatial data layers from state and federal data download websites. The NPS Integrated Resource Management Applications (IRMA) web portal (IRMA.NPS.gov) was used for road centerlines, the park boundary shapefile, and the 2016 geologic map of GRSM. Sub-meter-resolution light detection and ranging (LiDAR) digital elevation models (DEMs) were downloaded from the Tennessee GIS Clearinghouse (TNGIS.org/LiDAR) and North Carolina's Spatial Data Download website (SDD.NC.gov). Primary and secondary data were compiled and organized to create a geodatabase of unstable slopes along primary transportation corridors in GRSM.

Establish Priority Areas: KDE

The KDE method is an interpolation routine used to identify hotspots or high-risk areas based on a set of point or line data. For this study, the Kernel Density tool from ArcGIS Pro 2.7 was used to identify clusters of poorly rated unstable slopes. Line data were used that represent the length of the affected roadway associated with known unstable slopes. Each line was associated with a symmetrical surface centered on the line called a kernel. A quartic kernel with a fixed-interval bandwidth (search area) was used in this study (Silverman, 1986; ESRI, 2021). The following formula was used to calculate the density value at each output raster cell or (x, y) location (ESRI, 2021).

$$Density\,(KDE)$$
$$= \frac{1}{(radius)^2} \sum_{i=1}^{n} \left[\frac{3}{\pi} pop_i \left(1 - \left(\frac{dist_i}{radius} \right)^2 \right)^2 \right] \quad (1)$$
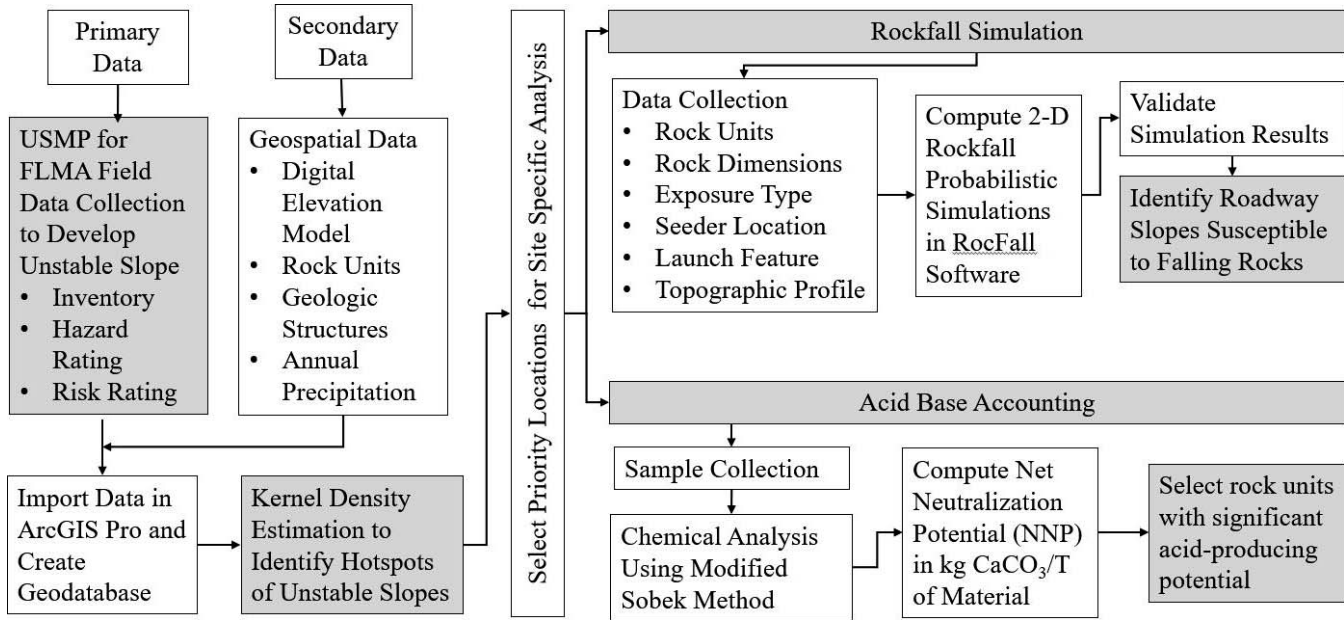
Figure 4. Methodology flowchart, where the gray color code corresponds to the study objectives.

This equation was used for $dist_i < radius$, where $i = 1, \ldots, n$ are the input line segments within the radius distance of a (x, y) location; the population field pop_i is the total USMP score; and $dist_i$ is the distance between line segment i and the (x, y) location. The default search radius was used in the study and was determined using an algorithm that (1) calculated the weighted mean center of input unstable slopes; (2) calculated the distance from the weighted mean center for all sites; (3) determined the weighted median of these distances, D_m; and (4) calculated the weighted standard distance, SD. Once these values were established, they were applied to the following formula:

$$Radius = 0.9 * \min\left(SD, \sqrt{\frac{1}{\ln(2)}} * D_m\right) * n^{-0.2} \quad (2)$$

where n is the sum of the population field values and either SD or $\sqrt{\frac{1}{\ln(2)}} * D_m$, whichever value is smaller.

The output KDE raster was used to establish priority study areas for site-specific analysis.

After selecting priority sites based on the results from the KDE, rockfall simulations and ABA tests were conducted at each slope coinciding with hotspots to develop a geologic and environmental prioritization framework for slope remediation (Figure 4). Rockfall simulation was conducted because field investigation revealed that common unstable slopes along the roadways were mostly categorized as rockfalls. Field assessments were conducted at each rock slope to record bedrock lithology, block dimension, slope material properties, seeder or starting location, and potential rockfall pathway data. The topographic profiles were extracted from the 1 m DEM and revised in the field using a laser range finder. Rockfall simulations were completed using RocFall software utilizing the rigid body analysis method with tangential Colorado Rockfall Simulation Program (CRSP) damping

Table 2. *Parameters used to calculate USMP ratings.*

Preliminary Rating	Hazard Rating	Risk Rating
Ditch effectiveness	Slope drainage	Route width
Rockfall history	Annual rainfall	Human exposure factor
Block size/volume per event	Slope height	% of decision sight distance
Impact on use	Maintenance frequency	Right of way impacts
Annual Average Daily Traffic/usage/economic or recreational importance	Structural condition	Environmental/cultural impacts
	Rock friction	Maintenance complexity
		Event cost

Table 3. *Earth materials parameter properties used for simulated rockfall pathways for the 14 investigated sites.*

Parameter	Barren Bedrock	Vegetated Bedrock	Talus, Loose Rock Debris	Asphalt	Generalized Soil
Coefficient of normal restitution (R_n)	0.4 ± 0.04	0.32 ± 0.04	0.32 ± 0.04	0.4 ± 0.04	0.3
Coefficient of tangential restitution (R_t)	0.8 ± 0.04	0.71 ± 0.04	0.82 ± 0.04	0.9 ± 0.03	0.81
Dynamic friction	0.55 ± 0.04	0.58 ± 0.04	0.56 ± 0.04	0.55 ± 0.04	0.56
Rolling friction	0.15 ± 0.02	0.4 ± 0.02	0.65 ± 0.04	0.1 ± 0.01	0.59

(RocScience, 2002). The slope material properties of the topography are listed in Table 3. One thousand (1,000) rocks, distributed evenly between seeders, i.e., starting locations, were thrown for each simulation, and a recommended default initial horizontal velocity of 1.5 m/s (4.9 ft/s) was used for every seeder, while initial vertical and rotational velocities were set to 0 m/s (0 ft/s), as recommended by the *RocFall User Guide* (RocScience, 2002). Point seeders were added to each slope based on field observations, and line seeders were added along slopes where point sources were not obvious, for example, where rock debris and fragments were observed along the length of a slope and within the ditch. Each seeder required block shape, dimensions (0.3 to 1.2 m [1 to 4 ft] in the elongated direction), and a density value that was specified using the rock type library. An appropriate rock type for the site was selected to determine density, while block shape(s) and dimensions were taken from field notes. The block size ranged from 0.3 to 1.2 m (1 ft to 4 ft) in the long direction, and the block shapes were various shapes of polygons selected from the library, as closely represented in the field. Additional input data such as roadway width, ditch properties, and presence of mitigation measures were collected during the field visits. Validation of model results was performed by comparing the rock pathways and end points to photographs taken during field visits and notes recorded in the field. Photographs and field notes provided an account of rock block locations along the slope, contained within the ditch, and occasionally within the roadway. For several sites, traces of scars associated with impacts of blocks on the roadways were also observed and recorded.

Rock samples were collected during field assessments and were sent to a commercial laboratory for ABA tests. Rock samples were collected as loose material along the toe of slopes, in compliance with the scientific research and collecting permit granted by the NPS to minimize impact to park resources (Figure 5). Three samples were collected at roughly equal distance along the base of each slope and placed in labeled plastic bags for storage. A composite sample was prepared for each site using approximately 333 g of material from each sample point for a total weight of 1 kg. An ABA test using the modified Sobek method described by Sobek et al. (1978) and Lawrence and Marchant

(1991) was used in this study. ABA test results are reported in units of kg $CaCO_3$ per tonne of material. Samples with net neutralization potential (NNP) values < -5 kg $CaCO_3/t$ are considered to have a significant acid-producing potential. In practical terms, an NNP value of -5 means that 5 kg of $CaCO_3$ are required to neutralize 1 t (1 metric ton) of sample material.

RESULTS

USMP Inventory

In total, 285 discrete unstable slopes assessed along 243.67 km (151.41 mi) of roadway in GRSM were added to the USMP database. Of these, 280 slopes were designated as localized rockfall, dominated by wedge and planar failure mechanisms. The five (5) remaining sites were designated as small-scale landslides in soil-fill embankments along stream banks. The USMP for FLMA classification system defines slope conditions as "good" when the total USMP score is <200, "fair" when it is ≥ 200 and ≤ 399, and "poor" when it is ≥ 400. This classification system is based on experience and was designed for federal land management agencies with low to very low traffic volumes (Beckstrand et al., 2019). In the assessment, 133 slopes ranked as "poor" (45 percent), 147 ranked as "fair" (53 percent), and five ranked as "good" (<2 percent) based on the USMP for FLMA classification system. Figure 6 shows the distribution of 285 slopes classified by quartile range to better compare local sites. Because 280 out of 285 slopes were rockfalls, the five landslide sites on soil slopes were discarded from further site-specific analysis.

The majority (72 percent) of unstable slopes were identified along three main roads in the park: Routes 0014 (Little River Gorge Road), 0010 N (Newfound Gap Road), and 0011 N, S (Gatlinburg Spur Road). Of these, 32 percent were located along Route 0014 in the Metcalf Phyllite, Cades Sandstone, and Thunderhead Sandstone geologic units, including four of the 10 highest-rated slopes; 18 percent were located along Route 0010 N, which crosses the NC-TN state border in the Anakeesta Formation, Copperhill Formation, and Thunderhead Formation; and 22 percent
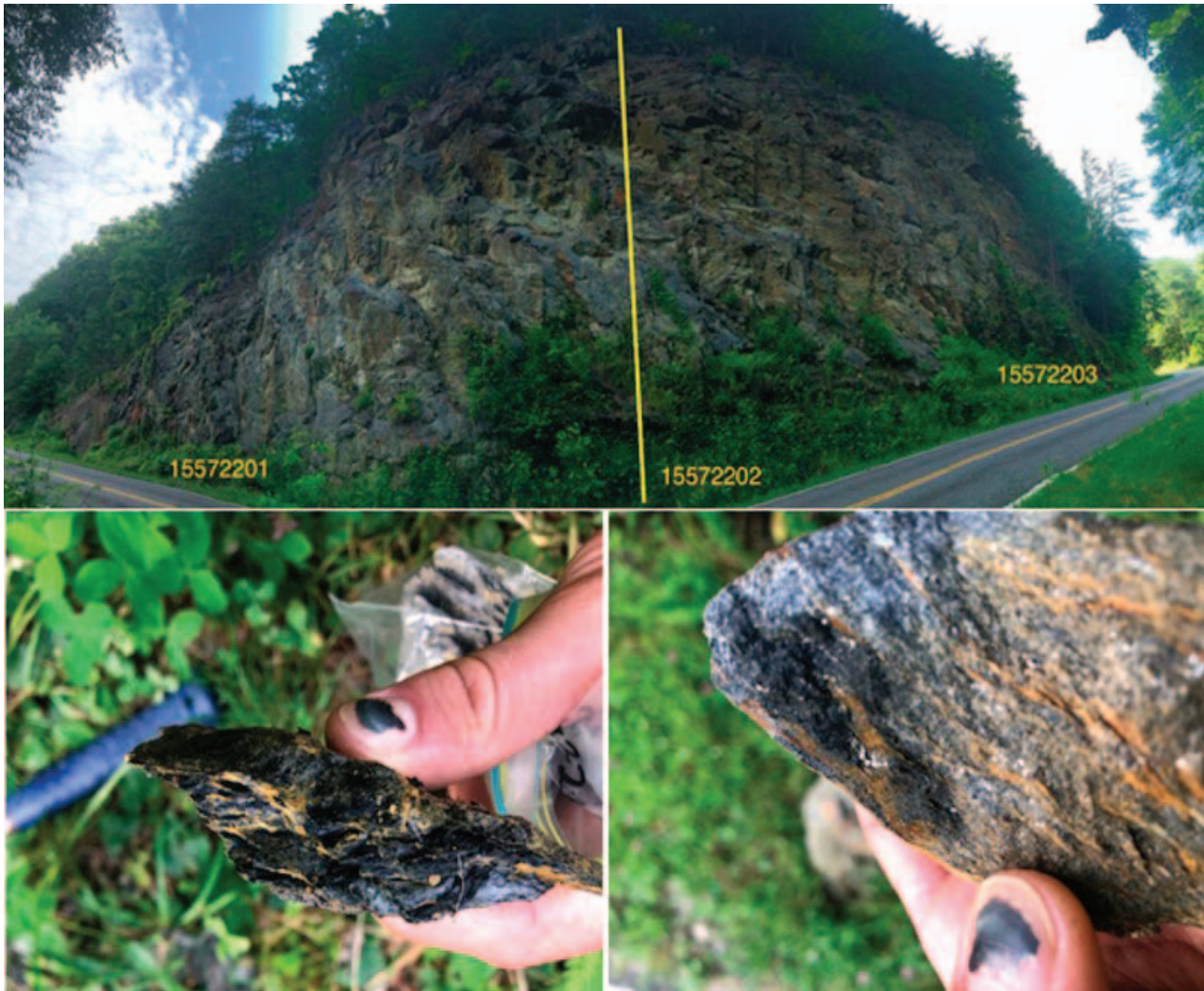
Figure 5. Composite samples were prepared for each unstable slope. This representative outcrop (GRSM-155) (35.4574186°N, 83.4956021°W) was in Wehutty Formation composed of dark metagraywacke and metasiltstone, with black graphite schist; outcrop is covered with Fe oxides, secondary sulfur minerals, and gypsum. The hand sample shown in the figure is a graphite schist. Net neutralization potential (NNP) for the composite sample was −26.4 (kg $CaCO_3$/t).

were identified along Route 0011 N and S, primarily in the Pigeon Siltstone and to a lesser extent in the Rich Butt Sandstone.

The remaining 28 percent of unstable slopes were distributed along the other primary transportation corridors. Notably, 12 percent of slopes were identified along Route 0008 E, F, G, and H from Chilhowee at the southwest to Wears Valley at the north near Sevierville, TN. Additionally, 5 percent of unstable slopes were assessed along Route 0019 near Bryson City, NC, within the Wehutty and Copperhill formations. Most of the primary roads and unstable slopes in GRSM were located on the TN side of the park in the foothills of the Western Blue Ridge Physiographic Province.

Kernel Density Estimation

The output density surface created using KDE had a spatial resolution of 10 m and was presented using equal interval classification. Dark purple patched areas in Figure 7 have the greatest density of poorly rated unstable slopes, as labeled in Figure 6 and subset in Figure 7. The geologic formations at the greatest density of poorly rated areas included the Anakeesta Formation, Thunderhead Sandstone, Cades Sandstone, Metcalf Phyllite, Wehutty Formation, Shields Formation, and Pigeon Siltstone. Six noticeable clusters of unstable slopes with a high likelihood of roadway disruption were identified along the Gatlinburg Spur (0011), Newfound
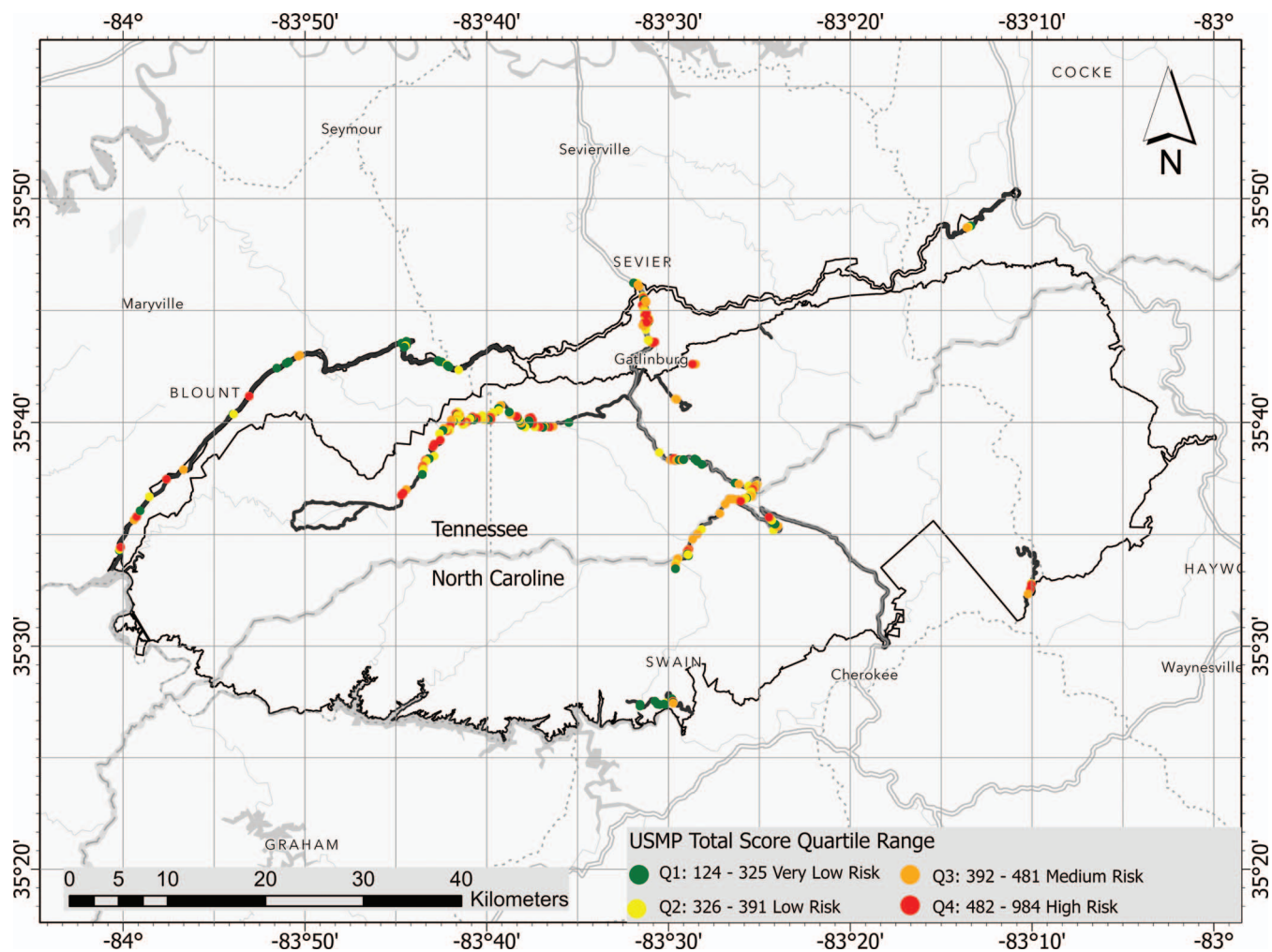
Figure 6. Inventory map of unstable slopes classified by USMP total score quartile range.

Gap Road (0010) near the TN-NC border, Little River Gorge Road (0014), and Laurel Creek Road (0015) (Figure 7). Lakeview Drive East Road (0019) showed a medium- to low-density cluster. Foothills Parkway West (0008) did not show any leading clusters; however, the route was included as an additional area of interest for further site-specific studies based on its documented history of sporadic rockfall and environmental hazards, such as acid rock drainage. Using the KDE output, 14 sites were selected within the clusters and along Route 0008 for site-specific analysis, including probabilistic rockfall simulation and ABA (Figure 7).

Probabilistic Rockfall Simulations

The RocFall output includes end-point analysis, kinetic energy (total, translational, and rotational), velocity (translational and rotational), and bounce height. End-point analysis is a significant factor con-

cerning safety on the roadway. Therefore, this study primarily focused on the distribution of rockfall end points as the percentage of rocks running out of the ditch and passing the edge of the roadway closest to the slope, passing the centerline, and exiting the roadway away from the slope. Validation of rockfall simulations was performed by comparing model results to Google Maps street view, site photographs, and field notes.

Results from the simulations showed rock material entering the roadway at all 14 sites (Figure 8). The distributions of end-point locations for each unstable slope are presented in Table 4. Across all sites, most rocks (63.4 percent) were contained by ditches and did not enter the roadway. End points for rocks that did enter the roadway were generally confined to one lane of traffic closest to the slope. Only 3.4 percent of rocks reached the centerline, and only 0.2 percent of rocks crossed both lanes of traffic. The predicted percentage of rocks contained within ditches varied widely among
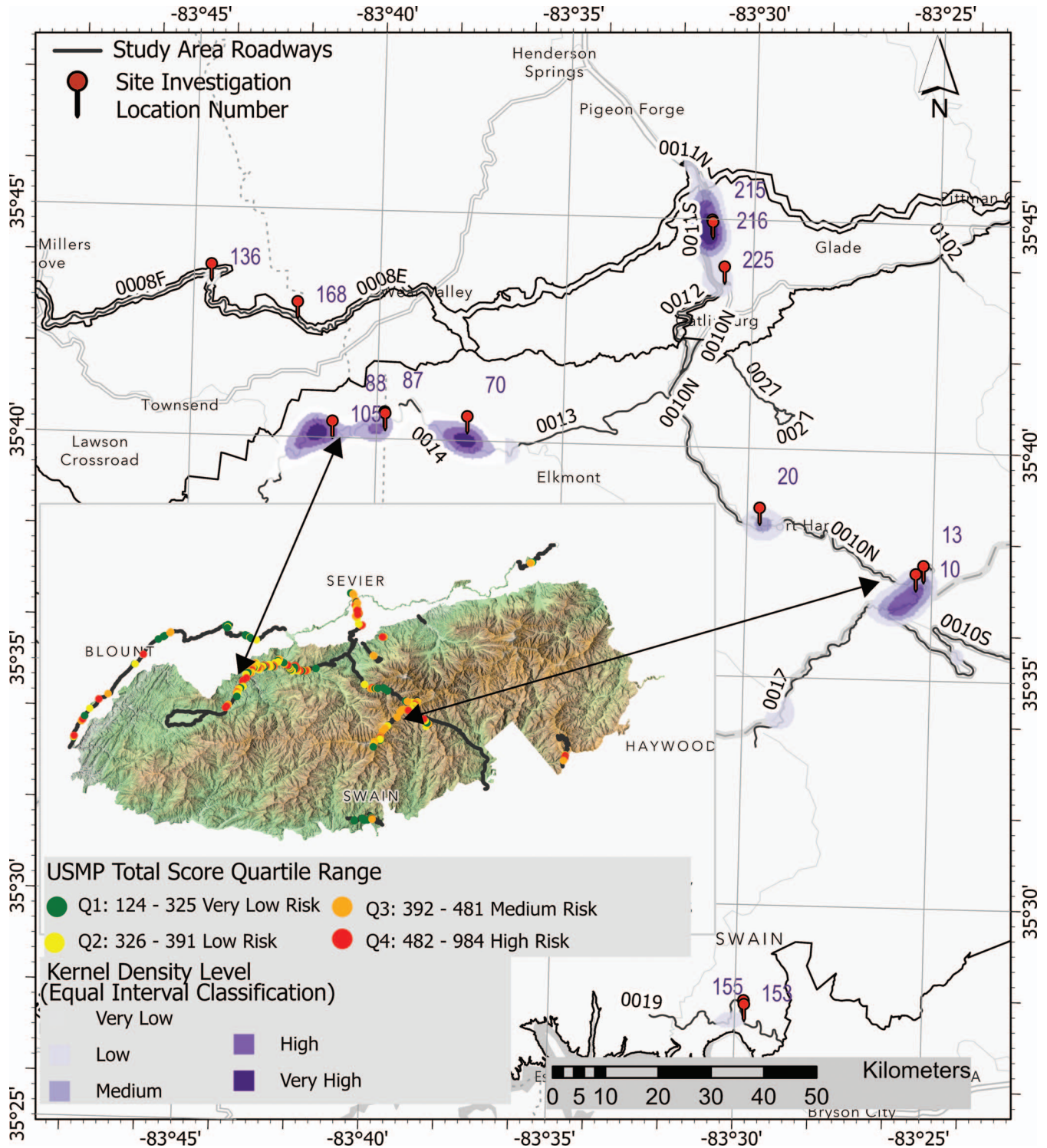
Figure 7. High-density clusters of poorly rated slopes were identified using KDE. Fourteen sites were selected within the clusters for site investigation. The subset map includes the locations of unstable slopes color-coded by risk rating.

slope models. For example, GRSM-168 on Foothills Parkway Section 8E had the most effective containment of material, with only one rock out of 1,000 (0.1 percent) entering the roadway. In contrast, GRSM-088 on Little River Gorge Road had the least effective containment, with 99.5 percent of rock-path end points within roadway, 3.3 percent of which reached the centerline. An inverse relationship between ditch width
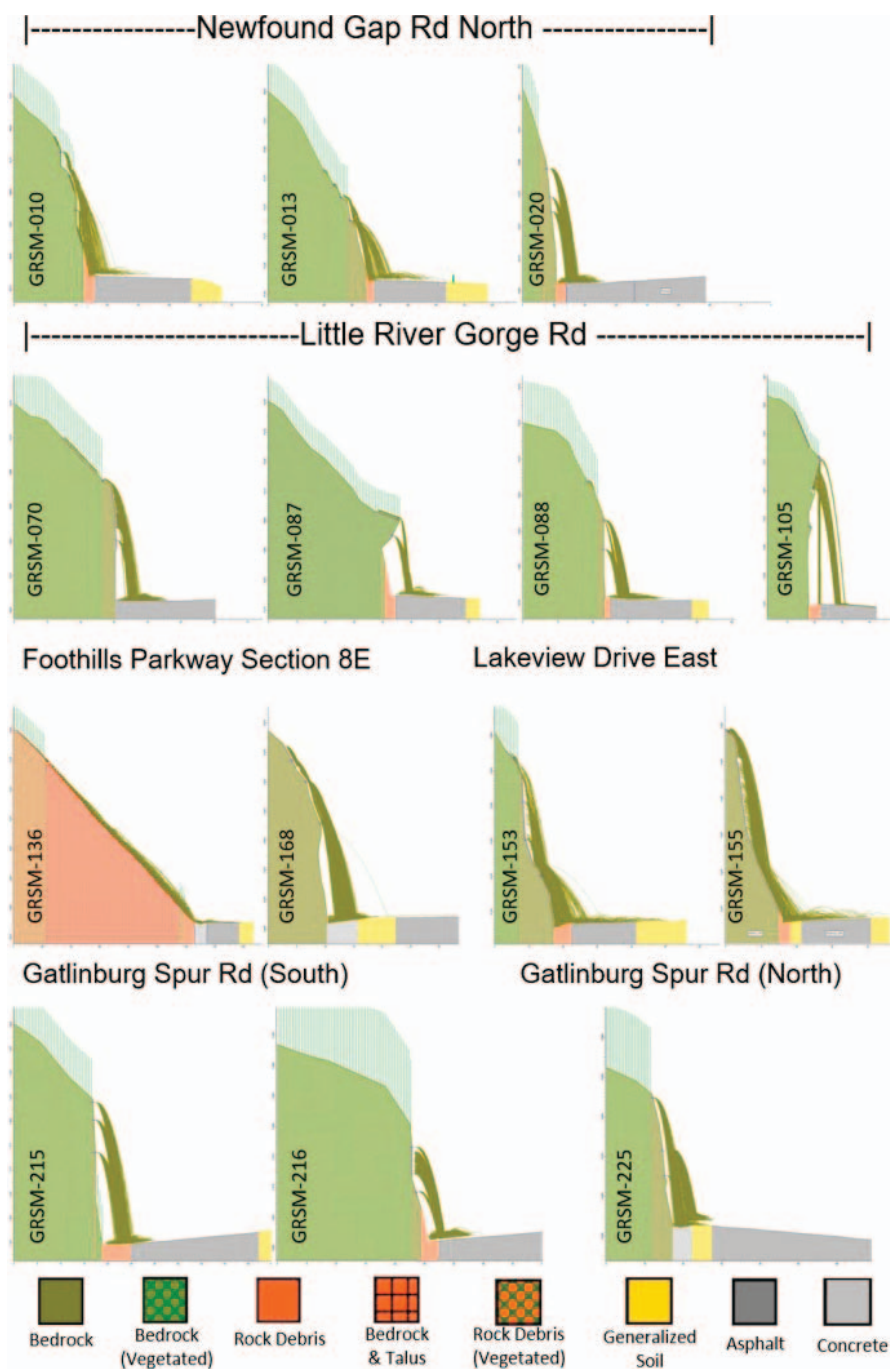
Figure 8. Simulated rockfall pathways for the 14 investigated sites.

and the percentage of rocks entering the roadway (Table 4) was noted; however, the statistical relationship was not analyzed due to the small sample size.

Environmental Impact (ABA)

Total sulfur concentration was reported as weight percent and ranged from below the detection limit (0.02 weight percent) to 1.5 weight percent. A full ac-count of ABA test results is included in Table 5. Samples from five sites contained significant concentrations of total sulfur (>0.5 weight percent). These values directly correlated with the sulfide concentration and therefore the acid-generation potential of the samples. Test results indicated a wide range of NNP values, from −31.1 to +69.2 kg $CaCO_3$/t (Figure 9). Notably, samples from GRSM-013 and GRSM-168 had significant sulfide concentrations and acid-generation

Table 4. *Distribution of end-point locations for each unstable slope.*

GRSM Route/ Road Name	GRSM ID	Ditch Width in m (ft) (Field Measured)	% Contained in Ditch	% End Points within Roadway	% Reached Centerline	% Exited Roadway	Validation Method
0010N Newfound Gap Road North	10	2.1 (7)	93.9	6.1	0	0	GSV, PH
0010N Newfound Gap Road North	13	1.4 (4.5)	85.5	14.5	2.1	0	GSV, PH, USMP
0010N Newfound Gap Road North	20	1.4 (4.5)	10.8	89.2	1.2	0	GSV, PH
0014 Little River Gorge Road	70	0	20.1	79.9	21	0	GSV, PH, USMP
0014 Little River Gorge Road	87	0.6 (2)	77.7	22.3	1.7	0	GSV, PH, USMP
0014 Little River Gorge Road	88	0.4 (1.25)	0.5	99.5	3.3	0	GSV, PH
0014 Little River Gorge Road	105	1.1 (3.5)	98.0	2	1.2	0	GSV, PH, USMP
0008E Foothills Parkway Section 8E	136	1.8 (6)	87.4	12.4	4	0.2	GSV, PH, USMP
0008E Foothills Parkway Section 8E	168	3.7 (12)	99.9	0.1	0	0	GSV, PH, USMP
0019 Lakeview Drive East	153	2.3 (7.5)	70.9	27.4	5.5	1.7	GSV, PH, USMP
0019 Lakeview Drive East	155	1.5 (5)	46.2	53.5	7.7	0.3	GSV, PH, USMP
0011S Gatlinburg Spur Road (South)	215	1.8 (6)	67.8	32.2	0	0	GSV, PH, USMP
0011S Gatlinburg Spur Road (South)	216	1.2 (4)	41.5	58.5	0	0	GSV, PH, USMP
0011N Gatlinburg Spur Road (North)	225	3.0 (10)	88.4	11.6	0	0	GSV, PH, USMP
	AVG:		63.5	36.4	3.4	0.2	

Validation methods: GSV = Google Maps Street View, PH = photographs and notes from field visits, USMP = comments from USMP geodatabase.

potentials that did not result in NNP values <-5 kg $CaCO_3$/t due to relatively high neutralization potentials. Four rock samples collected from three discrete slopes had NNP values <-5 kg $CaCO_3$/t. The most negative values, -31.1 and -27.6 kg $CaCO_3$/t, were from the Anakeesta Formation and were duplicate samples collected at GRSM-010 along Newfound Gap Road North. Two samples collected from two discrete slopes in the Wehutty Formation along Lakeview

Drive East also indicated significant acid-producing potential with NNP values of -26.4 and -20.7 kg $CaCO_3$/t.

DISCUSSION

The geodatabase and inventory maps created in this study represent an important step towards implementing long-term GAM protocols in GRSM. The

Table 5. *Complete ABA test results for the 14 investigated discrete slopes.*

GRSM ID/ Geologic Unit	Paste pH (pH units)	Total S (wt%)	HCl Extractable Sulfur (wt%)	Sulfide Sulfur (by diff.) (wt%)	Acid Generation Potential (kg CaCO₃/t)	Mod. ABA Neutralization Potential (kg CaCO₃/t)	Fizz Rating (N/A)	Net Neutralization Potential (kg CaCO₃/t)
010 (Dup.)/Zag	6.81	1.50	0.05	1.45	45.3	14.2	None	−31.1
010/Zag	6.55	1.42	0.05	1.37	42.8	15.2	None	−27.6
013/Za	6.64	1.08	0.04	1.04	32.5	62.5	Slight	30.0
020/Zt	6.75	<0.02	<0.02	<0.02	<0.6	1.20	None	1.20
070/Zts	7.84	0.09	0.01	0.08	2.5	7.00	None	4.50
087/Zc	6.87	0.26	0.16	0.10	3.1	4.20	None	1.10
088/Zc	8.49	0.20	0.01	0.19	5.9	8.00	Slight	2.10
105/Zm	8.14	0.43	0.09	0.34	10.6	11.9	Slight	1.30
136/Zw	8.45	0.04	<0.02	0.04	1.3	50.7	Slight	49.4
153/Zwe	4.07	0.82	0.19	0.63	19.7	−1.00	None	−20.7
155/Zwe	3.96	0.98	0.15	0.83	25.9	−0.500	None	−26.4
168/Zsc	8.51	0.97	0.04	0.93	29.1	98.3	Slight	69.2
215/Zp	9.06	<0.02	0.04	<0.02	<0.6	5.60	None	5.60
216/Zp	8.17	<0.02	0.02	<0.02	<0.6	6.50	None	6.50
225/Zr	7.96	0.11	0.01	0.10	3.1	10.9	Slight	7.80
Blank	8.49	<0.02	<0.02	<0.02	<0.6	0.0	None	0.0
Detection Limits	N/A	0.02	0.01	0.02	0.6	N/A	N/A	N/A

Zag = Anakeesta Formation, metagraywacke and metasiltstone; Za = Anakeesta Formation; Zt = Thunderhead sandstone; Zts = Thunderhead sandstone, dark metasiltstone, and slate; Zc = Cades sandstone; Zm = Metcalf Phyllite; Zw = Wilhite Formation; Zwe = Wehutty Formation; Zsc = Shields Formation, conglomerate; Zp = Pigeon Siltstone; Zr = Rich Butt sandstone.
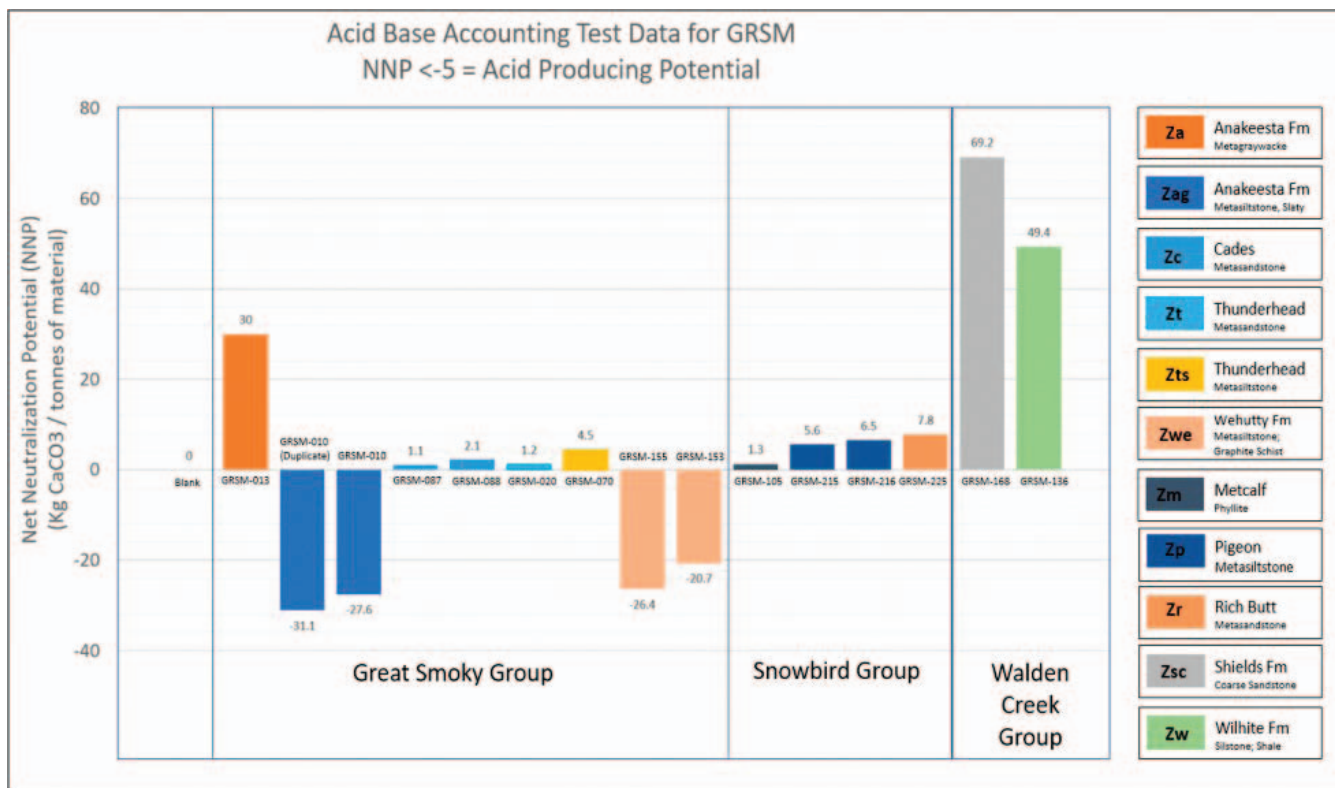
Figure 9. Acid-base accounting test data for GRSM.

cluster map created using KDE highlights sections of road where slopes with a high likelihood of road-way disruption are most concentrated and can be used to communicate risk to park visitors and commuters. Further site-specific kinematic investigation of the structural analysis of bedrock discontinuities along with the rock friction and cohesion within these clusters will provide insights into whether some geologic or geometric condition influences slope stability. Once study areas were established based on results from KDE and input from park officials, site-specific rockfall simulations and ABA tests were conducted at 14 selected as high-risk sites. These investigations provided a better understanding of the potential impacts of rockfalls on roadway infrastructure and the environment.

USMP Inventory and KDEs

Most unstable slopes identified in this study are located on the north side of the park in TN (88 percent) with only one KDE cluster identified in NC. Many of these slopes are within the foothills of the Western Blue Ridge Physiographic Province. This province is bounded to the north by the Great Smoky Fault and to the south by the Gatlinburg Fault and is character-ized by rolling hills with predominately sedimentary bedrock (Neoproterozoic, Cambrian, Lower Ordovician), which is either low-grade greenschist facies or has not been metamorphosed. About a quarter of all slopes were in the higher-grade metamorphic rocks of the highlands of the Blue Ridge, and less than 7 percent of sites were in the Tennessee Valley and Ridge Physiographic Province. Geologic units with the greatest number of unstable slopes along major transportation corridors are Neoproterozoic in age and include the Pigeon Siltstone (n = 45) and Metcalf Phyllite (n = 45) of the Snowbird Group and the Thunderhead Sandstone (n = 30), Cades Sandstone (n = 27), Anakeesta Formation (n = 28), and the Copperhill Formation (n = 25) of the Great Smoky Group. The remaining 85 slopes were distributed among 11 other rock formations. The *Great Smoky Mountains National Park Geologic Resource Evaluation Report* by Thornberry-Ehrlich (2008) and previous slopes stability studies at GRSM hinted upon the same susceptible rock units (Moore, 2004; Wieczorek et al., 2000; and Nandi and Shakoor, 2017).

The cluster analysis created using the USMP total score helped to highlight areas where unstable slopes pose significant risk to park visitors and commuters along GRSM primary routes. The cluster map

was also helpful in establishing priority areas within the park where site-specific studies were concentrated. More clusters and more unstable slopes in general occur on the north side of the park because this is where the majority of roadways within the study area exist. This represents a limitation of the study because the presence of clusters is controlled by the roadways and data collection sites. However, it may also be true that rock units within the foothills of the Western Blue Ridge Physiographic Province are more susceptible to rockfalls and rockslides where road cuts exist than rock units within the highlands. Future studies could evaluate whether a relationship exists between the metamorphic grade of geologic units and instability.

Ultimately, the aim of this study was to assess unstable slopes along major transportation corridors in GRSM, so data collection was constrained to accomplish that goal. The research provided examples of site-specific investigations like probabilistic rockfall simulation and ABA for selected sites that could be prioritized from cluster analysis using the USMP inventory database. This type of application could be adapted by a state department of transportation, FLMA, or future researcher to suit their specific needs. In addition to ongoing condition assessments and performance monitoring, future effort should be directed to develop forecasting models, such as topographical change detection using GPS combined with real-time kinematic (RTK) capabilities, unmanned aircraft system (UAS) structure from motion (SfM) analysis to generate three-dimensional slope models that can detect the temporal change of a surface, and terrestrial laser scanner (TLS) and aerial laser scanner (ALS) data from UAS to detect slope change and displacement. These forecasting models can provide estimates of future changes in the performance of discrete slopes, which can help GRSM park officials to anticipate changes to management costs and evaluate program alternatives.

Probabilistic Rockfall Simulations

Accurately predicting rockfalls is difficult due to variability in slope geometry, uncertain material properties, and the sensitivity of analysis methods (Stevens, 1998). However, results from probabilistic simulations provide an effective and acceptable method for evaluating the potential impact of rockfall on transportation corridors. Results from this study showed rock material entering the roadway at all 14 sites, which confirms the premise that GRSM's major transportation corridors are vulnerable to localized slope failures. Model results also indicated that some sections of roadway are more vulnerable than others, mainly

where ditch effectiveness is limited. These predictions were validated using a combination of Google Street View, field notes and photographs, and comments in the USMP for FLMA geodatabase. GRSM-136 on Foothills Parkway Section 8E stands out as somewhat unique from the other sites due to its long and consistent slope, wide ditch, and vegetation near the slope's toe. Also, a feature of interest is that vegetation has a significant damping effect on simulated rockfalls; however, this relationship is complicated by the fact that vegetation can contribute to biological weathering, especially in fractured rocks. Sites like GRSM-087 and GRSM-105 along Little River Gorge Road stand out because they feature blocks that slightly overhang the roadway.

Environmental Impact (ABA)

Insights from ABA tests can be used by GRSM park officials to help develop solid waste management protocols at cut slopes. Additional costs associated with encapsulating or transporting acid-producing rock debris are important to consider for budget allocation, which is an essential part of the GAM process. As part of ongoing condition assessment and performance monitoring, park officials should take note of the acid-producing potential of rock units. Weathering of Precambrian metasedimentary rocks in the Southern Appalachian Mountains is well recognized, and the Federal Highway Administration developed guidelines on evaluation and handling of acid-producing materials (Byerly, 1996). ABA test results indicated significant acid-producing potential at three discrete rock slopes of the 14 sites sampled. The study confirmed that the sulfide minerals contribute to the acid-generating potential, and the Anakeesta Formation and the Wehutty Formation present the greatest hazard regarding ARD. At these sites, it is reasonable to take special precautions when handling rockfall materials. Field investigation revealed that slaty metasiltstone members of the Copperhill Formation may also require special handling due to ARD; however, no samples were analyzed in this study. Significant ARD seems to be limited to a short length of roadway, about 21.2 km (13.2 mi) out of 243.7 km (151.41 mi), almost exclusively between mile markers 10 and 20 of Newfound Gap Road (GRSM-0010N, S), the first 1.6 km (1 mi) of Clingman's Dome Access Road (GRSM-0017), and the first 8 km (5 mi) of Lakeview Drive East (GRSM-0019), where units of the Anakeesta Formation, slaty metasiltstone member of the Copperhill Formation, or Wehutty Formation are exposed.

Schaeffer and Clawson (1996) concluded that the Anakeesta Formation is a potential acid-producing graphite schist unit, with NNP for the graphite schist

units ranging from -19.27 to 1.81 $CaCO_3/t$. Hammarstrom et al. (2003) conducted a thorough investigation of metal cycling in GRSM and identified soils at the Hazel Creek Mine with an NNP value of -61 kg $CaCO_3/t$. That study presented important considerations for sulfide minerals at historic mine sites within the park; however, the study did not discuss how sulfide minerals and ARD could impact transportation infrastructure or how solid waste management practices should be incorporated into GAM protocols. Latham et al. (2009) found an association of sulfide minerals with unstable slopes in metagraywackes and graphitic muscovite schists along the Blue Ridge Parkway. Further, sulfide-induced heave was not observed during field observations; however, Bryant (2003) documented the same in the Sevier Shale near the study area and presented chemical tests procedures and various ARD mitigation options.

CONCLUSION

Implementing long-term, risk-based strategic GAM is imperative for public lands, like GRSM, where maintenance officials are responsible for achieving performance objectives with a fluctuating annual budget. The goal of the work described here was to provide data to guide GAM efforts by prioritizing sites and informing the selection of site-specific interventions. The study succeeded in creating the first exhaustive inventory of unstable slopes along major transportation corridors in GRSM and provides an example of high-risk rock slope prioritization using cluster analysis. Additionally, 14 site-specific investigations were completed that predicted rockfall pathways using probabilistic simulations, and acid-base accounting tests were performed to evaluate the acid-producing potential of unstable rocks. The study provides a geologic and environmental framework for slope remediation to maintain the integrity of roadways in GRSM. The study will assist park officials in their efforts and foster a better understanding of life cycles of discrete unstable slopes.

This study utilized the USMP for FLMA protocol to (1) create a detailed inventory of 285 unstable slopes, of which five slopes were ranked as being in good condition, 147 slopes were ranked as fair, and 133 slopes were ranked as poor according to the USMP for FLMA classification system. (2) Five noticeable clusters of unstable slopes with high likelihood of roadway disruption were identified along three major transportation corridors using KDE. As state departments of transportation and FLMAs across the country adopt and implement GAM programs, cluster analysis can be used to target remediation and mitigation efforts. This is significant because, once an inventory has been created, the decision of where to target proactive management or mitigation can be daunting.

The site-specific analysis of the 14 high-risk slopes indicated that (3) rock fragments entered the roadway at all 14 sites, (4) sections of roadway where ditch effectiveness is limited are more vulnerable to rockfall, such as along Little River Gorge Road (0014), and (5) significant APP is limited to a short length of roadway overall, because only about 21.2 km (13 mi) of roadway exist where Anakeesta Formation, the slaty metasiltstone member of the Copperhill Formation, or Wehutty Formation are exposed. Probabilistic rockfall simulations can provide valuable information for park officials who are responsible for GAM protocols. Because rockfall events interfere with transportation corridors during most years, which can have a negative impact on the local economy, rockfall modeling has a role in future management and mitigation efforts. To a lesser extent, the same is true for analysis of acid-producing waste rocks at GRSM. Future studies can evaluate the correlation between acid-producing rocks and slope instability in the park.

Finally, results from this study affirm that GRSM's major transportation corridors are vulnerable to localized slope failures. Insights from the study can be used by GRSM park officials to help develop short- and long-range management and mitigation plans, such as widening ditches, installing barriers, and encapsulating acidic rockfall material. These strategies can inform park officials' efforts to monitor the performance of geotechnical assets and make periodic updates to the GAM in GRSM. In addition to ongoing condition assessments and performance monitoring, future effort should be directed to develop forecasting models that estimate future changes in performance of discrete slopes. These forecasting models can facilitate efforts by GRSM park officials to anticipate changes to management costs and evaluate program alternatives.

ACKNOWLEDGMENT

REFERENCES

ANDERSON, D. A. AND CUELHO, E., 2017, *Executive Summary for the Unstable Slope Management Program for Federal Land Man-*

agement Agencies (USMP for FLMA): Unstable Slope Management Program.

ANDERSON, S. A., 2016, Communicating multiobjective risk: A new geotechnical need for transportation: *Transportation Research Record*, Vol. 2580, No. 1, pp. 2C-8.

BANKS, B.; HOLLAND, J.; ABDELHADI, M.; BAUER, J. B.; AND BAIN, A., 2021, Unstable Slope Management Program—Implementation along the Blue Ridge Parkway, North Carolina, Part 2. *Banks: Association of Environmental and Engineering Geologists Programs with Abstracts*, Vol. 64, No. 4, pp. 52–53.

BAUER, J. B.; FUEMMELER, S. F.; AND BANKS, B., 2021, Unstable Slope Management Program—Implementation along the Blue Ridge Parkway, North Carolina, Part 1: *Association of Environmental and Engineering Geologists Programs with Abstracts*, Vol. 64, No. 4, pp. 52–53.

BECKSTRAND, D.; BENKO, B. A.; MINES, A.; PIERSON, L. A.; THOMPSON, P. D.; AND KIMMERLING, R., 2017, *Statewide Geotechnical Asset Management Program Development: Final Report for Rock Slopes, Unstable Soil Slopes and Embankments, Retaining Walls, and Material Sites:* Alaska Department of Transportation and Public Facilities, Research and Technology Transfer, Publication No. STP4000(126)(A).

BECKSTRAND, D.; STANLEY, D.; THOMPSON, P.; BILDERBACK, E.; WITTIE, M.; UPULEE, K.; CUELHO, E.; AND ANDERSON, D. A., 2019, *Unstable Slope Management Program for Federal Land Management Agencies:* Federal Highway Administration Report No. FHWA-FLH-19-002.

BOGUCKI, D. J., 1976, Debris slides in the Mt. Le Conte area, Great Smoky Mountains National Park, U.S.A.: *Geografiska Annaler*, Vol. 58, No. 3, pp. 179–191.

BRYANT, L. D., 2003, *Geotechnical Problems with Pyritic Rock and Soil:* Unpublished Ph.D. Dissertation, Virginia Tech, Blacksburg, VA.

BYERLY, D. W., 1996, Handling acid-producing material during construction: *Environmental & Engineering Geoscience*, Vol. II, No. 1, pp. 49–57. https://doi.org/10.2113/gseegeosci.II.1.49

CAPPS, D. M.; ROSENBERG, R.; COLLINS, A.; ANDERSON, D. A.; HOOPER, S.; ROGERS, H.; COLLINS, B.; AND BILDERBACK, E., 2017, Geohazards risk assessment of the Denali National Park Road. In De Graff, J. V. AND Shakoor, A. (Editors), *Landslides: Putting Experience, Knowledge and Emerging Technologies into Practice:* Special Publication 27, Association of Environmental and Engineering Geologists (AEG), Brunswick, OH, pp. 840–850.

CHEROKEE ONE FEATHER, 2019, Heavy rainstorm results in rockslides, downed trees, and motorist fatality on Spur: Cherokee One Feather, Electronic document, available at https://www. theonefeather.com/2019/08/heavy-rainstorm-results-in-rockslides-downed-trees-and-motorist-fatality-on-spur/

CULLINANE, T. AND KOONTZ, L., 2020, *National Park Visitor Spending Effects: Economic Contributions to Local Communities, States, and the Nation:* National Park Service Natural Resource Report NPS/NRSS/EQD/NRR—2020/2110.

ESRI (ENVIRONMENTAL SYSTEMS RESEARCH INSTITUTE), 2021, ArcGIS Pro, Release 2.8.3: ESRI, Redlands, CA.

FEDERAL HIGHWAY ADMINISTRATION, 2020, *Zion National Park Unstable Slope Assessment Report:* U.S. Department of Transportation Geotechnical Report No. UT-NX-USMP-20-01 (also Federal Highway Administration Report No. FHWA-OR-RD-02-04).

HAMMARSTROM, J. M.; SEAL, R. R.; MEIER, A. L.; AND JACKSON, J. C., 2003, Weathering of sulfidic shale and copper mine waste: Secondary minerals and metal cycling in Great Smoky Mountains National Park, Tennessee, and North Carolina, USA: *Environmental Geology*, Vol. 45, No. 1, pp. 35–57.

HILL, J. S., 2018, *Post-Orogenic Uplift, Young Faults, and Mantle Reorganization in the Appalachians:* Unpublished Doctoral Dissertation, The University of North Carolina at Chapel Hill, NC.

LATHAM, R. S.; WOOTEN, R. M.; CATTANACH, B. L.; MERSCHAT, C. E.; AND BOZDOG, G. N., 2009, Rock slope stability analysis along the North Carolina section of the Blue Ridge Parkway: Using a geographic information system (GIS) to integrate site data and digital geologic map. In *43rd US Rock Mechanics Symposium & 4th US-Canada Rock Mechanics Symposium:* American Rock Mechanics Association, Alexandria, VA.

LAWRENCE, R. W. AND MARCHANT, P. M., 1991, *Acid Rock Drainage Prediction Manual:* Mine Environment Neutral Drainage MEND/NEDEM Report, March 1, 1991.

MATHEWS, R. C., JR. AND MORGAN, E. L., 1982, Toxicity of Anakeesta formation leachates to shovel-nosed salamander, Great Smoky Mountains National Park: *Journal of Environmental Quality*, Vol. 11, pp. 102–106. https://www. osti.gov/biblio/5546278

MATSUOKA, N., 2001, Direct observation of frost wedging in alpine bedrock: *Earth Surface Processes Landforms*, Vol. 26, pp. 601–614. https://doi.org/10.1002/esp.208

MCKENNA, A. M., 2007, Characterizing Groundwater-Surface Water Interactions in Great Smoky Mountains National Park Using Hydrologic, Geochemical and Isotopic Data: Unpublished M.S. Thesis, University of Tennessee, Knoxville, TN.

MOORE, H. L., 2004, *A Roadside Guide to the Geology of the Great Smoky Mountains National Park*: University of Tennessee Press, Knoxville, TN, 192 p.

NANDI, A. AND SHAKOOR, A., 2017, Predicting debris flow initiation zone using statistical and rock kinematic analyses: A case study from West Prong Little Pigeon River, TN. In De Graff J.V. and Shakoor, A., eds., Proceedings, 3rd North American Symposium on Landslides, June 4-8, Roanoke, VA, pp. 912–920.

NPS (NATIONAL PARK SERVICE), 2019, *National Park Service Land Resources Division Listing of Acreage 2019 (Summary): National Park Service*, Washington, DC, pp. 1–11.

NPS (NATIONAL PARK SERVICE), 2021, Annual Park Recreation Visitation (1904–2021): Electronic document, available at https://irma.nps.gov/Stats/SSRSReports

NPS-GRSM (NATIONAL PARK SERVICE–GREAT SMOKY MOUNTAINS NATIONAL PARK), 2014, *Cycle 5 NPS/RIP Route ID Report:* Great Smoky Mountains National Park, Gatlinburg, TN, pp. 1–43.

NPS-GRSM (NATIONAL PARK SERVICE–GREAT SMOKY MOUNTAINS NATIONAL PARK), 2017, *GRSM Park Statistics:* Electronic document, available at https://www.nps.gov/ grsm/learn/management/statistics.htm

ROCSCIENCE, INC., 2002, *RocFall: Risk Analysis of Falling Rocks on Steep Slopes [User's Guide]:* Electronic document, available at https://www.rocscience.com/downloads/ rocfall/RocFall%20Tutorial.pdf

SASS, O., 2005. Spatial patterns of rockfall intensity in the northern Alps: *Zeitschrift für Geomorphologie N. F. Supplementband*, Vol. 138, pp. 51–65.

SCHAEFFER, M. F. AND CLAWSON, P. A., 1996, Identification and treatment of potential acid-producing rocks and water quality monitoring along a transmission line in the Blue Ridge Province, southwestern North Carolina: *Environmental & Engineering Geoscience*, Vol. II, pp. 35–48.

SILVERMAN, B. W., 1986, *Density Estimation for Statistics and Data Analysis*: Chapman & Hall, London. http://dx.doi.org/10.1007/978-1-4899-3324-9

SOBEK, A. A.; SCHULLER, W. A.; FREEMAN, J. R.; AND SMITH, R. M., 1978, *Field and Laboratory Methods Applicable to Overburden and Mine Soils:* Industrial Environmental Research Laboratory, Office of Research and Development, U.S. Environmental Protection Agency EPA Report 600/2-78-054, 204 p.

SOUTHWORTH, S.; SCHULTZ, A.; ALEINIKOFF, J. N.; AND MERSCHAT, A. J., 2012, *Geologic Map of the Great Smoky Mountains National Park Region, Tennessee and North Carolina:* U.S. Geological Survey Scientific Investigations Map 2997, one sheet, scale 1:100,000, and 54 p. pamphlet. (Supersedes U.S. Geological Survey Open-File Reports 03–381, 2004–1410, and 2005–1225.)

STANLEY, D. A., 2011, Asset management in a world of dirt: Emergence of an underdeveloped sector of transportation asset management: *TR News*, Vol. 277, pp. 18–22.

STANLEY, D. A., AND ANDERSON, S. A., 2017, Managing landslides and slopes as transportation infrastructure assets. In *Proceedings of the 3rd North American Symposium on Landslides and Engineered Slopes:* Association of Environmental and Engineering Geologists, Brunswick, OH, pp. 71–82.

STEVENS, W. D., 1998, *RocFall, a Tool for Probabilistic Analysis, Design of Remedial Measures and Prediction of Rockfalls:* Unpublished Ph.D. Dissertation, University of Toronto, Canada.

TENNESSEE DEPARTMENT OF TRANSPORTATION (TDOT), 2010a, All lanes temporarily opened on The Spur, 9 March 2010: Electronic document, available at https://www.tn.gov/news/2010/3/9/all-lanes-temporarily-opened-on-the-spur.html

TENNESSEE DEPARTMENT OF TRANSPORTATION (TDOT), 2010b, TDOT completes rockslide repairs on U.S. 441 in Sevier County, 30 April 2010: Electronic document, available at www.tn.gov/news/2010/4/30/tdot-completes-rockslide-repairs-on-u.s.-441-in-sevier-county.html

THOMPSON, P. D., 2017, *Geotechnical Asset Management Plan: Technical Report:* Alaska Department of Transportation and Public Facilities Research and Technology Transfer Report No. STP000S(802)(B).

THORNBERRY-EHRLICH, T., 2008, *Great Smoky Mountains National Park Geologic Resource Evaluation Report:* National Park Service Natural Resource Report NPS/NRPC/GRD/NRR—2008/048.

TURNER, K. A. AND SCHUSTER, R. L., 1996, *Landslides—Investigation and Mitigation:* Transportation Research Board, National Research Council, National Academy Press, Washington, DC.

USGS (U.S. GEOLOGICAL SURVEY), 2013, *Great Smoky Mountains Landslide, North Carolina, 2013: Electronic document, available at* https://www.sciencebase.gov/catalog/item/589e0885e4b099f50d3a0675

VARNES, D. J., 1978, *Slope Movement Types and Processes:* Transportation Research Board Special Report 176, pp. 11–33.

WEGWERTH, I., 2019, Landscape Architect, Great Smoky Mountains National Park. Personal Communication.

WIECZOREK, G. F. AND LEAHY, P. P., 2008, Landslide hazard mitigation in North America: *Environmental & Engineering Geoscience*, Vol. 14, No. 2, pp. 133–144.

WIECZOREK, G. F.; MORGAN, B. A.; AND CAMPBELL, R. H., 2000, Debris-flow hazards in the Blue Ridge of central Virginia:" *Environmental & Engineering Geoscience*, Vol. 6, No. 1, pp. 3–23.

New Insights from Legacy Seismic Data regarding Basalt Elevations and Variability on the Hanford Site

JAMES T. ST. CLAIR*
ADAM R. MANGEL
TIM C. JOHNSON

Pacific Northwest National Laboratory, 902 Battelle Boulevard, Richland, WA 99354

Key Terms: *Columbia River Basalt, Landstreamer, Hydrostratigraphy, MASW, Tomography*

ABSTRACT

Migration of groundwater contaminants in the Gable Gap area of the Hanford Site in southeastern Washington State is strongly influenced by the distribution and permeability of basalts that lie beneath an unconfined aquifer. Locally, folding and faulting of the Columbia River Basalt associated with the Yakima fold and thrust belt followed by erosion due to the Lake Missoula floods resulted in a complex basalt surface that represents either an impermeable lower boundary to the unconfined aquifer system or localized regions of increased permeability that potentially promote communication between the unconfined aquifer system and deeper, confined aquifer systems. Paleo-channels carved into the basalt by floodwaters are thought to provide preferential flow paths for groundwater contaminants. In 2011, a seismic landstreamer campaign was carried out to image the basalt surface and produced pre-stack depth migrated p-wave reflection images. The reflection images identified two large troughs that may represent paleo-channels and several areas of possible faulting. Here, the streamer data are re-analyzed using refraction travel-time and Rayleigh wave dispersion analyses to obtain images of compressional and shear wave velocities within the suprabasalt sediment sections and the upper basalt surface. The combined interpretation of reflection and seismic velocity images shows complexity in the basalt velocity and elevation, which varies by 50 m or more within the study area. These results, along with other ongoing geophysical investigations, will be used to inform the site geologic model and potentially guide placement of future boreholes needed to quantify vertical flow between the confined and unconfined aquifers.

*Corresponding author email: james.stclair@pnnl.gov

INTRODUCTION

The Hanford Superfund site in southeastern Washington State is where plutonium was produced for use in U.S. nuclear weapons during World War II and throughout the Cold War. Liquid waste disposal associated with these activities has resulted in groundwater contaminant plumes within the unconfined aquifer emanating from the 200 East Area (Figure 1) (Hartman et al., 2009). The relatively impermeable nature of the underlying basalt compared to the overlying sediments supports the conceptual model of the basalt acting as a lower boundary of the local aquifer system (DOE/RL, 2012, Appendix E). In some regions, basalt elevations are higher than the water table, and flow is confined largely to the regions where Pleistocene flooding associated with Lake Missoula scoured channels through the basalt (Bjornstad et al., 2010). These channels and other local geologic structures are thought to provide preferential flow paths for contaminant plumes to travel north toward the Columbia River (Bjornstad et al., 2010). In addition, regional erosion of underlying basalt layers during Pleistocene flooding events exposed several of the deeper basalt units and interbeds to the unconfined aquifer above, which may allow vertical communication between the unconfined aquifer and deeper, confined aquifers within the Columbia River Basalt (CRB) group (Graham et al., 1984). Given these heterogeneities and potential impacts of contaminant migration to the Columbia River, a detailed examination of paleo-channel geometry is warranted as well as identification of regions that potentially support communication between deep, confined aquifer systems and the overlying unconfined system.

Surface-based seismic methods can provide useful information about subsurface structure as it relates to key hydrologic parameters (e.g., Hubbard and Linde, 2010). Seismic reflection methods utilize waves that reflect off subsurface boundaries to produce images of subsurface stratigraphy and structure. Seismic refraction methods utilize waves that are transmitted through the subsurface, turning back toward
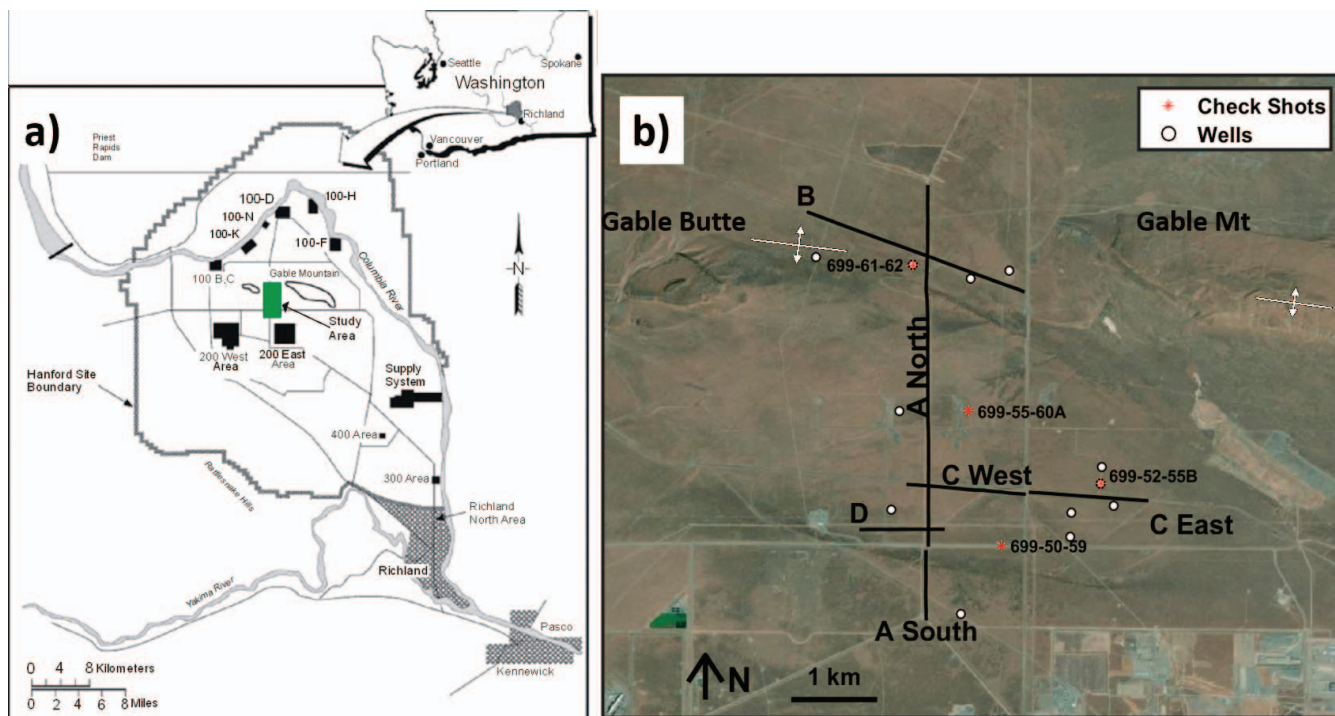
Figure 1. (a) Location of the Hanford Site in southeastern Washington (after Sunwall et al., 2011). The Gable Gap area is shown in green. (b) Satellite view of the Gable Gap area showing the seismic profile locations (black lines) and the locations of check shots (red stars) and wells (white circles with black outlines) used to validate seismic models. Gable Mountain Anticline is indicated by symbols.

the surface as they encounter faster-velocity materials at depth (Steeples, 2005). Travel times of refracted waves can be used to image the seismic velocity structure within the subsurface. It is most common to measure compressional wave velocity (Vp) with refraction methods. Shear wave velocity (Vs) can be measured with dispersive Rayleigh waves (Park et al., 1999). Seismic velocities vary systematically with lithology, porosity, saturation, and pressure (e.g., Mavko et al., 2009); thus, they are useful for identifying bedrock depths, the water table, and zones that are potentially more permeable.

Several seismic reflection surveys have been conducted in the Gable Gap area of the Hanford site. During 1979 and 1980, approximately 80 km of seismic reflection data were acquired as part of the Basalt Waste Isolation Project to identify deep storage targets for spent fuel (SSC, 1979,1980). More recently, several shallow seismic investigations have been carried out to identify basalt elevations and structure for hydrologic investigations (Cummins, 2009; Hyde et al., 2011) Hyde et al. (2011) showed the utility of the seismic landstreamer for the rapid collection of seismic data on the Hanford site. Their results showed a rugged and faulted basalt surface along 12 km of seismic profiles. A subsequent landstreamer study (Sunwall et al., 2011) added 12 km of seismic profiles within the Gable Gap area and further supported a rugged and faulted

basalt surface. A 2012 study that integrated all of the existing seismic reflection data in the area and compared known basalt depths to the seismic interpretations concluded that the reflection data often overestimated basalt depths, possibly due to an inaccurate seismic velocity model used to convert travel times to depth (Williams et al., 2012).

In this study, 12 km of legacy landstreamer data (Sunwall et al., 2011) are analyzed to measure Vp and Vs from the refracted p-waves and the dispersive Rayleigh wave signals. The resulting velocity models provide an estimate of basalt depth that is independent from the pre-stack depth migrated (PSDM)–derived estimates. Comparing these new results to borehole observations and integrating them with the reflection images provides an updated interpretation of depth to basalt within the Gable Gap and 200 E areas that will be used to refine the site geologic model. Zones of interest are also identified where additional characterization is needed to evaluate the possibility of vertical communication between the unconfined aquifer and deeper aquifer systems.

Hydrogeologic and Geophysical Setting

The hydrostratigraphy in the Gable Gap area consists primarily of the sand- and gravel-dominated Hanford units overlying the faulted and folded CRB group
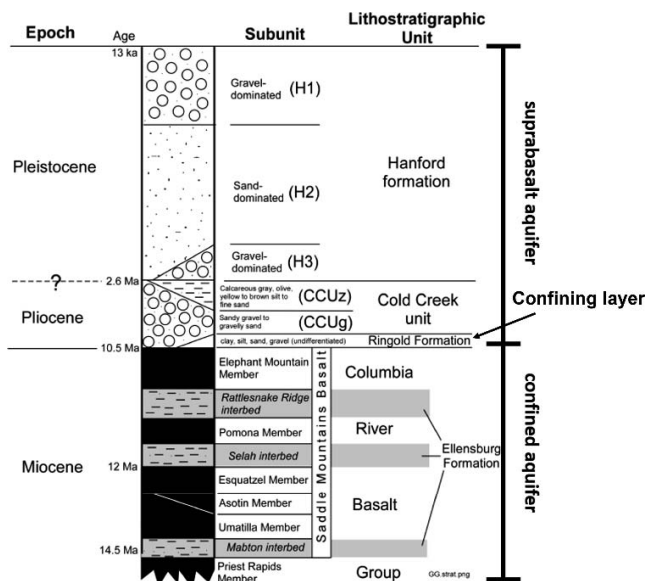
Figure 2. Generalized hydrostratigraphy in the Gable Gap area (after Bjornstad et al., 2010).

Figure 3. Summary of downhole seismic velocity measurements made in boreholes near the Gable Gap area (Rohay and Brouns, 2007). Unsaturated Vp for the Hanford (H-2 and H-3) and Cold Creek sediments are shown in black, and saturated Vp in the Cold Creek, Ringold (Rg), and basalt units are shown in blue. Vs for all units is shown in red.

with sediment interbeds (Figure 2). Older suprabasalt sedimentary units in the area are the Cold Creek unit and the Ringold formation, which are sparsely distributed, having been eroded during Pleistocene flooding associated with Lake Missoula. The top of the basalt is considered to mark the bottom of an unconfined, suprabasalt aquifer. A confined aquifer also exists within the basalts and interbedded sediments.

The Gable Gap (Figure 1) lies within the Yakima fold and thrust belt. To the north of the study area, the asymmetric east-to-west Gable Mountain anticline (GMA) folds the CRBs and the interbedded Ellensburg formation. The northern dipping limb of this anticline is steep, whereas the southern limb has a relatively gentle dip. Second-order syncline and anticline pairs have been inferred to exist along the southern limb and throughout the study area (e.g., Ault, 1981). Previous studies have hypothesized that secondary normal and thrust faults may also exist along the southern limb of the GMA (e.g., Hyde et al., 2011).

The principal CRB unit of hydrologic interest in the Gable Gap area is the Elephant Mountain member, which is considered the base of the unconfined, suprabasalt aquifer (Bjornstad et al., 2010). However, erosion related to Pleistocene flooding of Lake Missoula has locally eroded the Elephant Mountain member, exposing older basalt units and sediment interbeds to the unconfined aquifer, and may allow vertical communication between the unconfined and confined aquifers in these areas (Graham et al., 1984).

Above the CRB, the unconfined suprabasalt aquifer is hosted in the flood-deposited Hanford formation. The Hanford formation contains both gravel- (H1 and

H3) and sand- (H2) dominated units, and their distribution reflects flood dynamics. The older Ringold and Cold Creek units are river deposits containing gravels, sands, and silts. However, within the Gable Gap area, they were largely eroded during the Lake Missoula floods and are unlikely targets for refraction imaging.

Rohay and Brouns (2007) used check shots to measure Vp and Vs in three boreholes in the 200 East Area south of the landstreamer profiles (Figure 1a). Vp data were collected using a sledgehammer source, and Vs data were collected using a horizontal accelerated weight drop. The boreholes penetrated the Hanford units, the Cold Creek unit, the Ringold formation, and the CRB. Their measurements reflect unsaturated conditions for the Hanford units and the Cold Creek unit and saturated (below the water table) conditions for the Cold Creek unit, Ringold formation, and CRB (Figure 3). The influence of the water table can be seen for the Cold Creek formation; Vp in unsaturated Cold Creek is 1,200–2,000 ms^{-1}, while saturated Cold Creek ranges between 3,400 and 3,900 ms^{-1}. Since fluids do not support shear stresses, Vs is largely unaffected by fluid saturation.

The Rohay and Brouns measurements indicate that Vp should be a reliable means of distinguishing basalt from the Hanford formation. Unsaturated Cold Creek is also easily distinguished from basalt. Vp in saturated Cold Creek and the Ringold formation overlap with the basalt measurements, indicating that it will not be possible to differentiate them using Vp measurements. Additionally, Ringold Vs overlaps with basalt Vs, suggesting that even unsaturated Ringold cannot be

confidently distinguished from basalt on the basis of seismic velocity alone.

Legacy Seismic Data

The landstreamer is a rapid seismic acquisition system that consists of a string of geophones and an accelerated weight drop (AWD) towed behind a vehicle. The geophone spacing is fixed so that after each shot, the entire system is moved forward, and the source-receiver offsets remain constant. The streamer survey geometry is suitable for reflection imaging, compressional wave refraction imaging, and Rayleigh wave dispersion analysis.

Approximately 12 km of landstreamer data were collected in April and May 2011 by the Confederated Tribes of the Umatilla Indian Reservation and Montana Technological University. The streamer comprised 96 gimballed 30-Hz geophones spaced 2 m apart. The streamer was towed by a pickup truck, which also towed an AWD 6 m in front of the streamer. The AWD was a 227-kg steel ram lifted by a hydraulic pump and accelerated by an elastic band. The AWD was used to vertically strike a 60×60-cm steel plate at 2-m intervals along each profile. This source produces high-amplitude seismic energy in the 5- to 150-Hz band and facilitates rapid data acquisition. The data set includes 5,564 shot gathers, and each shot record contains 2 seconds of data sampled every 0.5 ms. The minimum offset was 6 m, and the maximum offset was 196 m.

Sunwall et al. (2011) processed the reflection data and produced PSDM images. However, the raw data (Figure 3) show clear direct and refracted arrivals with apparent Vp that is consistent with suprabasalt sediments ($\sim$1,200 ms^{-1}) and the underlying basalt ($\sim$4,500 ms^{-1}). Dispersive surface waves are also evident and suggest suprabasalt Vs between 200 and 600 ms^{-1}. In this article, the first-arrival travel times and Rayleigh wave dispersion curves are used to image Vp down to basalt and Vs in the upper 15–30 m, respectively.

METHODS

Seismic Tomography

Seismic refraction methods utilize the travel time of the first arriving body wave for each source–receiver pair. Seismic velocities generally increase with depth, causing seismic rays to turn, or refract, back toward the surface as they propagate. At short source–receiver distances, the first arrival often represents the wave traveling directly from the source to the receiver, and the slope of the distance–time curve is the inverse of

seismic velocity. At longer distances, it is often observed that the travel-time curve becomes flatter, indicating that the waves have traveled through a higher-velocity medium. Seismic velocities can be measured directly from the slopes of the travel-time curves. However, when there is lateral variability in the subsurface, a more robust approach is required. Tomography is an iterative method where the subsurface is represented by many small elements of constant velocity. An initial velocity structure is chosen (usually an increase in velocity with depth), and travel times for the initial model are predicted. The difference between the predicted and the observed arrival times is used to find a model update that reduces the misfit. The process of predicting travel times and updating the model is iterated until the data misfit becomes acceptable.

Finding an appropriate update to the model requires solving an inverse problem that is generally poorly constrained. The data contain errors, some regions of the model may not contribute to the travel-time prediction, and solutions are non-unique (e.g., de Wit et al., 2012). The problem can be made stable by including smoothness constraints on the model, known as regularization. Regularization constraints place a penalty on model parameters that are very different from their neighbors. There is a trade-off between data misfit and model smoothness, and it is possible to find many velocity models that explain the data.

The conventional approach to regularizing the seismic tomography problem is to minimize the L2 norm (square root of the summed values) of the velocity gradient. This approach will not allow sharp boundaries, and because the L2 norm seeks to normally distribute velocity gradients throughout the model, it tends to produce smooth gradients in areas where the data do not constrain the model. An alternative approach is to minimize the L1 norm of the velocity gradient (sum of the absolute values), which allows sharp boundaries to develop and suppresses gradients in areas where the data do not constrain the model. In the Gable Gap area, the transition from suprabasalt sediments to basalt is likely a sharp velocity contrast for several reasons. First, borehole geophysical measurements indicate that the transition from suprabasalt sediments to basalt is sharp (Rohay and Brouns, 2007; Hyde et al., 2011; Figure 2). The raw seismic shots also contain several indicators of a sharp seismic boundary; the apparent basalt Vp measured on the raw data is $\sim$4,500 m s^{-1}, and the apparent sediment velocity is $\sim$1,200 m s^{-1} (Figure 3). Much of the data also contain a converted shear wave phase with an apparent velocity of $\sim$2,200 m s^{-1} (Figure 3). The presence of this phase indicates that Vs in the basalt is greater than the Vp of the material immediately above it (St. Clair and Liberty, 2019).

A two-dimensional tomography code (St. Clair, 2015) written in MATLAB was used to invert manually interpreted first-arrival observations. The code predicts travel times using the shortest path raytracing method (Moser, 1991), and the inverse problem is regularized with first-order derivative operators in the vertical and horizontal directions. The L1 constraint on model gradient is implemented with an iterative least squares algorithm (Ajo-Franklin et al., 2007). The high spatial density of the data results in many redundant raypaths; thus, travel times were interpreted on every second to third shot gather.

Travel-time tomography, like many geophysical methods, suffers from uncertainty and non-uniqueness. Uncertainty is due to noise in the data, the possible correlation of different model parameters, and non-uniform sensitivity of model parameters to the data. The same factors contribute to non-uniqueness of the solution. Because these issues are inherent in the method, the approach used to model the data needs to be consistent with the geologic setting, using information not contained in the travel times (e.g., the presence of converted phases) as a constraint for model selection and validation.

Non-uniqueness in the tomography solution occurs both because of errors and uncertainty in the input data and because many different velocity structures can have identical travel-time curves (e.g., Shearer, 1999). The choice of an L1 constraint on model smoothness favors models with a sharp boundary. The range of acceptable models is further limited by preferring solutions with the minimum amount of structure required to fit the data within estimated uncertainty. The picking error is estimated to be on the order of 1–3 ms; thus, the root mean square errors for the models should be ~3 ms. Finally, regions of the models are masked if they do not contribute to the data misfit (i.e., where no rays are present) using the derivative weight sum. The derivative weight sum represents the total length of raypaths that pass through a given model cell.

The data set contains several points where profiles intersect (Figure 1b). Comparing the velocity estimates and interpreted depths to basalt at these points can give some insight into the precision of the approach. Since each profile was inverted independently, the coincident measurements can be considered as independent observations. Finally, models are validated by comparing the predicted depth to basalt to nearby well observations and, where available, to velocity profiles derived from check shot data in nearby wells.

Rayleigh Wave Dispersion Analysis

Rayleigh waves are surface waves that have both vertical and horizontal components of motion. They travel at phase velocities, which are slightly slower than shear waves, and the lower-frequency (longer-wavelength) components are sensitive to greater depths. A typical Rayleigh wave dispersion curve will have higher phase velocities at low frequencies and lower phase velocities at high frequencies.

The multichannel analysis of surface waves (MASW) approach (Park et al., 1999) was used in this analysis. A linear radon transform approach (Mikesell et al., 2017) was used to map the raw shot gathers into the frequency-phase velocity domain (Figure 4b–d), and the dispersion curves were manually interpreted. The dispersion curves were then inverted for one-dimensional Vs profiles that represent the average Vs structure across the width of the streamer aperture (196 m). The results are displayed as pseudo–two-dimensional Vs images with each one-dimensional model mapped to the midpoint of the streamer for the corresponding shot gather. Due to the high spatial density of the data set, the dispersion curves were interpreted for every second or third shot gather where noise level allowed a confident interpretation to be made. Some portions of the data were too noisy to interpret, and final images are masked to reflect the absence of data.

Like travel-time tomography, MASW requires an inverse solution to find the optimal Vs-depth profile that agrees with the measured data. The inversion is iterative and requires a method for predicting the dispersion curve for any given model. The propagator matrix approach described in Aki and Richards (2002) was used to predict dispersion curves, and first-order difference operators were used to constrain the inversions to be smooth. The Rayleigh wave phase velocity is sensitive to Vs, Vp, and density. Since the influence of Vp and density is small compared to Vs (Xia et al., 1999), the Vp/Vs ratio was fixed at 2, with density increasing linearly from 1,900 to 2,100 m kg^{-3} from the surface to a depth of 35 m. Models are parameterized as layers that increase in thickness from 1 to 3 m with increasing depth.

While the 30-Hz geophones used in this survey limit the amount of low-frequency content required for deeper MASW sensitivity, Ivanov (2008) demonstrated that dispersion curves can be interpreted down to about an octave lower than the natural frequency of the geophones. Frequency-phase velocity images for the data presented here show interpretable dispersion down to ~15–20 Hz (Figure 3). To indicate where the models are sensitive to the data, the partial derivatives of data misfit with respect to model parameters are summed for each model layer, and layers that have little influence on data fit are masked. This procedure suggests that the dispersion data are most sensitive to the upper 10–20 m. Basalt depths are 50–100 m, so
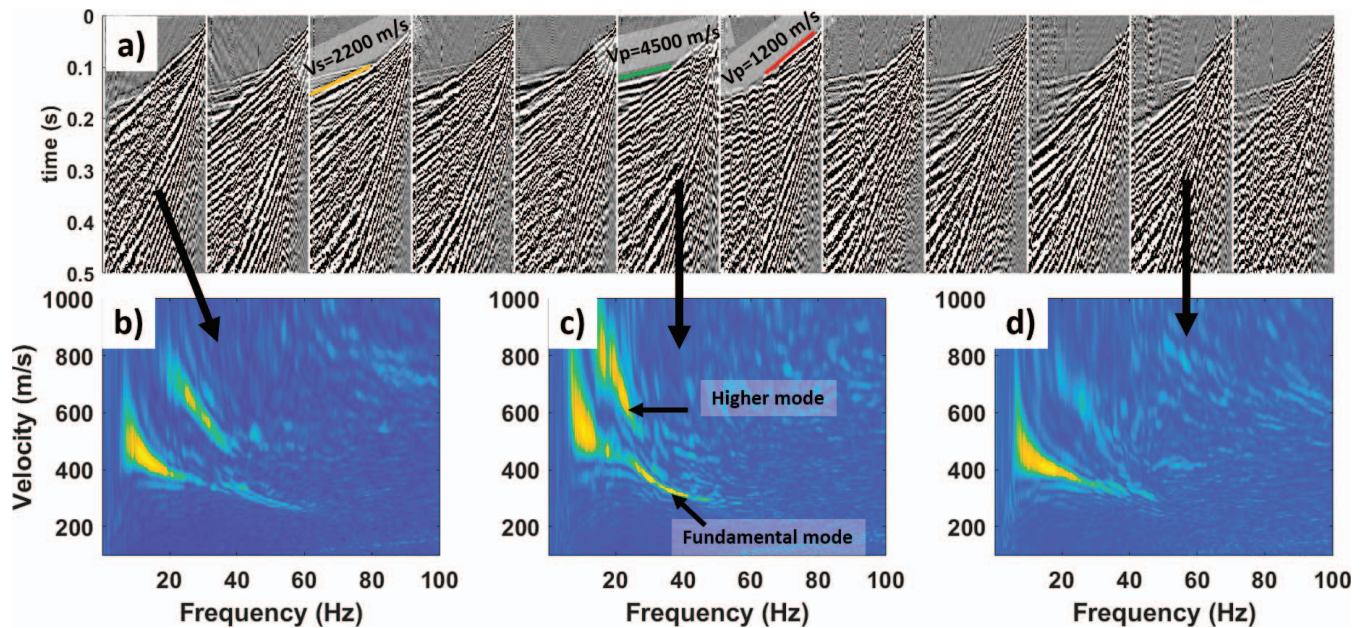
Figure 4. (a) Every 100th shot gathers along prolife B, showing clear first arrivals with apparent Vp consistent with suprabasalt sediments (1,200 ms^{-1}) and basalt (4,500 ms^{-1}). Only 0.5 seconds of the 2-second record is shown. Many of the shot gathers in this data set also contain a converted phase with an apparent velocity around half that of the first arrival. This P-SV-P phase suggests a sharp transition from sediment to basalt. The data also contain dispersive Rayleigh waves suitable for imaging shallow Vs structure (b–d).

the data do not constrain basalt properties; however, they do provide information about shallow sediment properties.

The MASW approach produces one-dimensional models that smear geologic structure over the width of the geophone aperture of 196 m. Thus, the resulting images are unlikely to capture strong lateral changes in Vs but will highlight long-wavelength structure.

RESULTS

The refraction-generated Vp and MASW-generated Vs models for Line A North and Line B are presented (Figures 5 and 6) and compared to the PSDM images of Sunwall et al. (2011) as well as nearby borehole observations of basalt elevation and velocity profiles obtained from downhole check shots. Figure 1 displays the locations of all wells and check shots that are compared to the seismic results. Results for the other profiles indicated in Figure 1 are displayed in the supplementary information. https://www.aegweb.org/e-eg-supplements

Line A North

Line A North (Figure 5) is an approximately 4.1-km, north-to-south profile (see Figure 1). It is the longest profile in the data set and crosses two troughs interpreted as paleo-channels (distances of 400–800 m and 2,000–3,000 m in Figure 5a). Vp in the suprabasalt

sediment section ranges from 400 and 1,500 m s^{-1}, and basalt Vp ranges between 3,000 and 4,500 m s^{-1}. The 3,000-m s^{-1} Vp contour is intermediate between sediment and basalt velocities and typically lies at the center of the steepest vertical velocity gradient; thus, this velocity contour was selected to interpret the transition from sediment to basalt.

Lower basalt Vp is apparent along the edges of regions where the depth to basalt is not well constrained (distances of 400–800 m and 2,000–3,000 m in Figure 5a). Here, the data lack the coverage necessary to adequately constrain basalt properties. In contrast, the lower basalt velocity near 3,400–3,500 m is well constrained and nicely correlates with a discontinuity in the PSDM reflection image (yellow colors representing Vp ~2,500 m/s; Figure 5a). This area may represent a locally permeable basalt feature. There are two regions along A North where the refraction data do not constrain depth to basalt between profile distances of 300 and 1,000 m and 2,000 and 3,000 m. Here, either the basalt may be too deep to image with the streamer offset or the basalt velocity may be lower compared to other regions. It is also noteworthy that in these areas, the PSDM image shows a less continuous reflector, suggesting that the basalt may be fractured or otherwise damaged through erosion or faulting, supporting the interpretation that basalt Vp is lower.

There are three locations along this profile that are intersected by other lines, and the depth to the
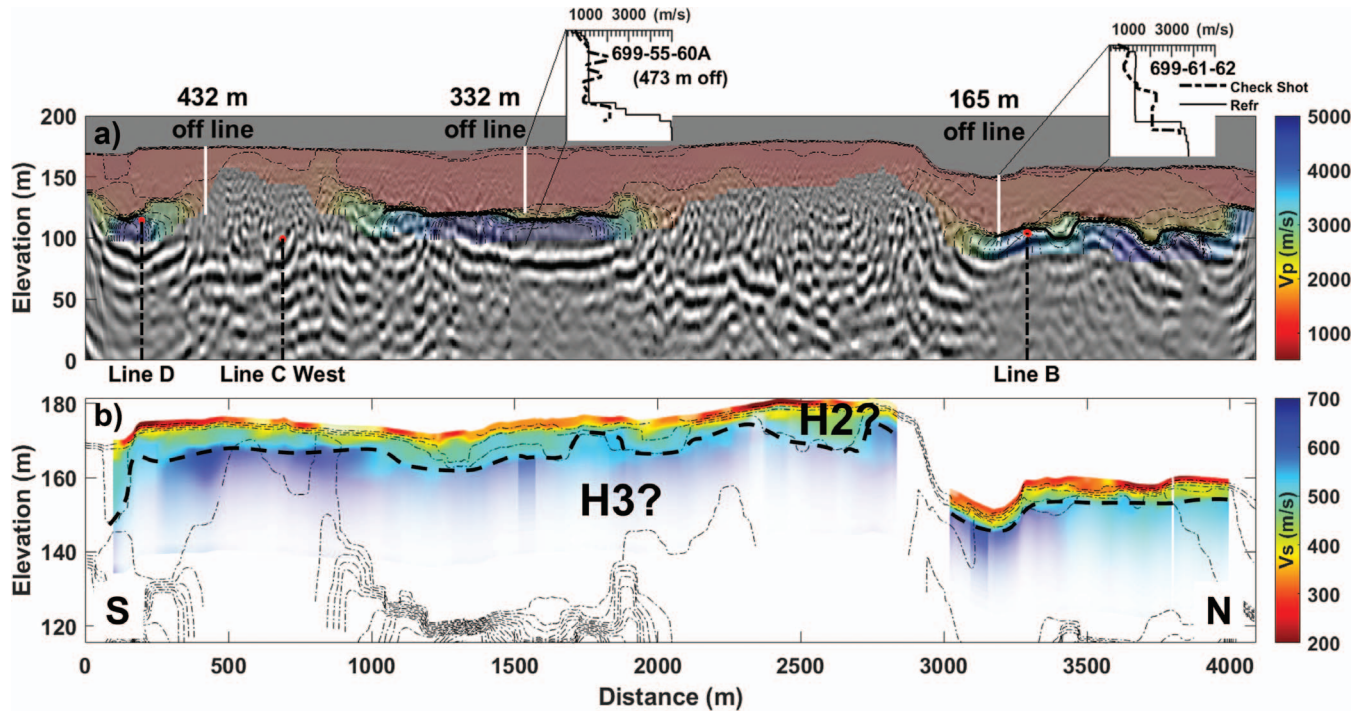
Figure 5. (a) Line A North Vp result overlaid on PSDM image. White lines indicate basalt elevations observed in nearby wells. Thick black line highlights the 3,000 m s⁻¹ Vp contour used to interpret basalt elevation. Red dots indicate interpreted depths to basalt on crossing profiles. Check shot Vp results compared to refraction-derived Vp are shown in insets. (b) The Vs image with Vp contours overlaid (thin dashed lines). Dashed black line is interpreted transition between the sandy H2 and the gravel-dominated H3.
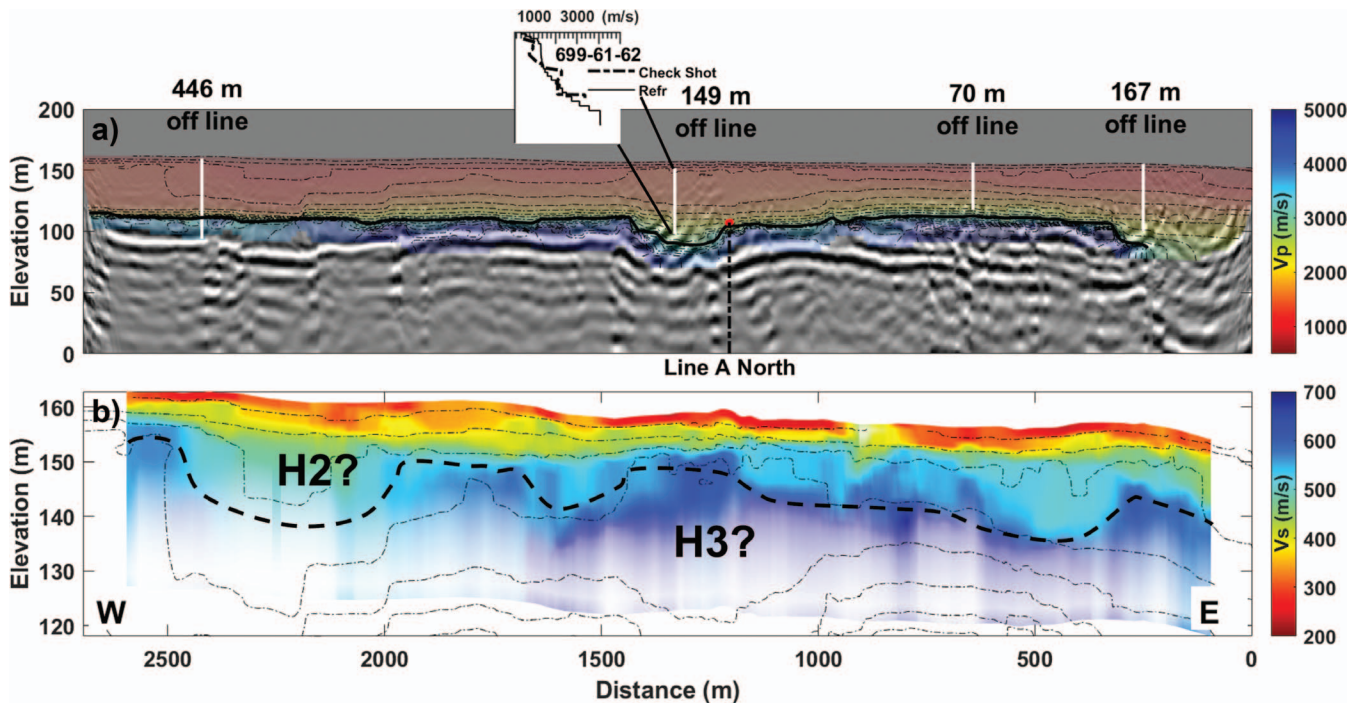
Figure 6. (a) Line B Vp result overlaid on PSDM image. White lines indicate basalt elevations observed in nearby wells. Thick black line highlights the 3,000 m s⁻¹ Vp contour used to interpret basalt elevation. Red dots indicate interpreted depths to basalt on crossing profiles. Check shot Vp results compared to refraction derived Vp are shown in insets. (b) The Vs image with Vp contours (thin dashed lines) overlaid. Dashed black line is interpreted transition between the sandy H2 and the gravel-dominated H3.

3,000-m s^{-1} contour along those profiles is shown by red dots. Where lines B and D cross, interpreted depth to basalt on all three profiles is very close. The 3,000-m s^{-1} contours are within 2 m at the Line D crossing and 4 m at the Line B crossing. Line C West has the depth to 3,000-m s^{-1} at approximately the same depth as the reflections in the PSDM image.

Three well observations of basalt elevation are within 500 m of Line A North to compare to the refraction result in Figure 5a. In two cases, the well observations correspond to locations where depth to basalt is well constrained by the refractions. Well 699-55-60A did not reach basalt; thus, this well represents a minimum basalt depth. The depth to basalt in well 699-61-62 and the 3,000 m s^{-1} are within 5 m, or ~10 percent, of the total observed depth. The difference may be attributed to uncertainty in the seismic result or to real variation in basalt elevation between the seismic profile and the well. A third nearby well cannot be compared to the Vp result, as the refraction data do not image basalt at that location.

Two check shot velocity profiles are also available along Line A North (Figure 5a). Well 699-55-60A is ~475 m to the east of the profile and did not reach basalt. It shows two thin, high-velocity (Vp = 2,000 m s^{-1}) layers that are not evident in the refraction result. Well 699-61-62, which did reach basalt at a depth of 54 m (Figure 5a, inset), indicates two Vp layers within the sediment section (Vp < 1,200 and Vp = 2,000 m s^{-1}). The refraction result is intermediate between these two velocities. The basalt depths and velocity estimates in well 699-61-62 closely match the refraction result.

Vs along this profile ranges between 150 and 650 m s^{-1} (Figure 5b). The 1,000-m s^{-1} Vp contour closely resembles the transition between Vs less than 500 m s^{-1} and Vs greater than 550 m s^{-1}, suggesting that this transition differentiates the H2 from the H3 formation.

Line B

Line B is an approximately 2.7-km-long northwest-to-southeast trending profile in the northern part of the study area (Figure 1). Here, a similar distribution of velocities is observed in the suprabasalt sediment section as Line A North. The top of the basalt shows a prominent dip at profile distance ~1,350 m, mirroring the structure depicted in the PSDM image (Figure 6a). Recovered velocities in that area are lower compared to adjacent sections. Combined with the discontinuous structure indicated by the PSDM image, it suggests that this is an area where the basalt surface is irregular and possibly fractured and permeable. On the eastern edge of the profile, either the basalt

is too deep for imaging or the velocity of the upper basalt is lower compared to elsewhere along the line.

Four well observations of basalt elevation are within 500 m of Line B (Figure 6a). The well projected onto profile distance 2,400 m is 446 m away and suggests that the refraction result underpredicts the basalt depth and agrees more closely with the PSDM image. The well is far away and may not represent the basalt depth at the seismic profile. Elsewhere along the line, the nearby wells are in better agreement with the refraction result.

Well 699-61-62 is 149 m to the south of Line B. It is evident that the refraction result represents a smoothed version of the velocity profile obtained from the check shot. The refraction result here shows a smooth transition into basalt velocities, which may explain why it overpredicts basalt depth and demonstrates the uncertainty inherent in the refraction method. It is also possible that basalt elevation is different at the well site than it is along Line B.

Vs along this profile shows a similar correlation to Vp structure, indicating that the H1 and H2 formations are not uniformly thick. Near the center of the profile, a high-velocity anomaly in both Vp and Vs suggests a thinning of the H2 layer.

DISCUSSION

Comparison to PSDM

Williams et al. (2011) compiled all the available seismic reflection data in the Gable Gap area and compared them to well observations and found that the reflection data consistently overpredicted the estimated depth to basalt. Much of the data that Williams et al. (2011) reviewed were time-stacked images converted to depth using a smooth-velocity model derived from check shots. Williams et al. (2011) suggested that the depth prediction errors were likely due to a poor time-to-depth-conversion velocity model. That argument does not apply to the PSDM images, as the PSDM approach simultaneously and iteratively produces a high-resolution velocity model directly from the data (e.g., Sheriff and Geldart, 1995). The final output is a reflection image in depth that can be directly compared to the refraction-derived Vp images.

Compared to the interpreted refraction Vp images, basalt depths predicted using the PSDM images do tend to be greater. However, this is not universally true. Along the northern-most end of Line A North (Figure 5a) and along Line C East (Figure S3), the refraction Vp results are remarkably similar to the PSDM images. Ignoring the depth discrepancies, a close similarity between topography along the basalt
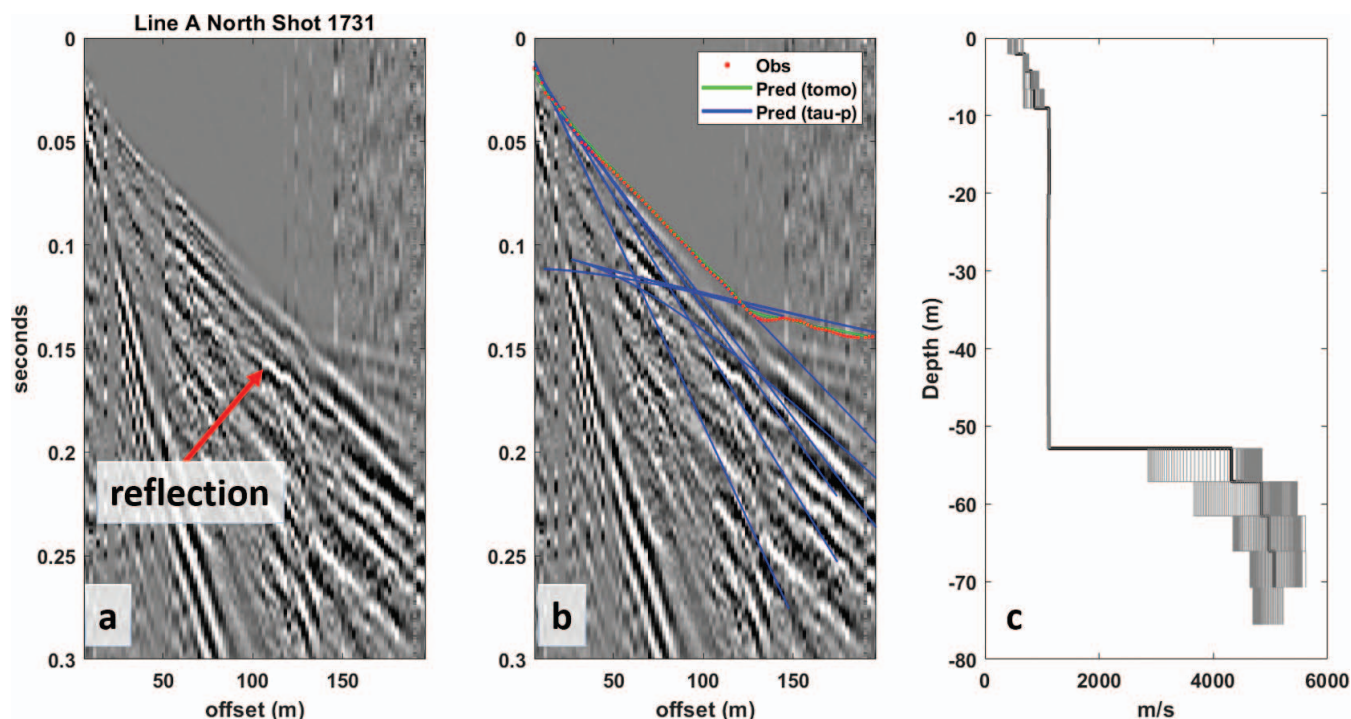
Figure 7. Shot gather 1731 along Line A North with a 200-ms agc. This shot gather corresponds to a profile distance of ~1,362 m in Figure 5a. (a) The raw data where a reflection can be seen at ~0.15 second and 100-m offset. (b) The same shot gather with picked travel times (red dots), predicted travel times for the tomography model (green line), and predicted arrival times of all phases generated by the tau-p approach (blue lines) for the extracted velocity model shown in panel c. The hyperbolic reflection generated by the steep velocity gradient at ~52-m depth agrees with the reflection observed in the raw data. Black curve in panel c indicates the average vertical velocity gradient across the width of shot 1731, and gray lines show vertical velocity profiles extracted at 2-m intervals across the width of the streamer at shot 1731.

surface interpreted from the PSDM images and from the refraction Vp images was observed. This suggests that the structural complexity indicated by both approaches can be reliably interpreted even if the absolute elevations are uncertain.

Raw shot gathers contain visible basalt reflections and can be used to validate the Vp-derived basalt depth estimates. Travel times for a one-dimensional velocity profile extracted from the tomography result were predicted from Line A North in an area that shows relatively little lateral structure. The Vp was extracted along the aperture of a shot gather (196 m) centered at the midpoint between the source and the farthest offset receiver for shot gather 1731. This midpoint lies at profile distance of ~1,362 m in Figure 5a. Predicted travel times for all possible refracted and reflected phases were generated for the averaged, one-dimensional model using a tau-p approach (Shearer, 1999) and were overlain on the raw data. Figure 7a shows the trace-normalized shot gather with a 200-ms AGC applied. The basalt reflection is visible at ~0.15 seconds and 100-m offset. Figure 7b shows the predicted travel-time curves for the one-dimensional model (blue lines); refracted phases have

straight slopes, and reflected phases are hyperbolic. The reflection time predicted by tau-p closely matches the reflection observed in the shot gather. Figure 7b also shows the observed first-arrival times compared to the raytracing predictions, which closely match the tau-p predictions. This suggests that the discrepancy between the two approaches is related to the inherent non-uniqueness of both the Vp tomography and the PSDM approach and reinforces the need to validate geophysical results with multiple independent observations.

Coincident measurements of basalt elevation interpreted from the Vp results along Lines A North, B, and D suggest that the precision of the refraction method is on the order of ±2–4 m. This likely applies to regions where the basalt surface is laterally uniform. In areas where the basalt has rough topography, the refraction data will tend to smooth out the small-scale variations associated with sediment velocity transitions. A good example of this is the comparison of the Vp image and the check shot from well 699-61-62 (Figure 6a). The Vp tomogram shows a smooth gradient from sediment to basalt velocities, whereas 150 m away, the check shot shows a hard boundary. The re-

flection image shows rough topography on the basalt at this location. Since the refraction data can resolve only a smoothed version of the structure, the depth to basalt is poorly constrained.

Variations in Basalt Vp

The Vp tomograms show variations in basalt velocity that may indicate areas where the basalt is fractured and likely to be permeable. The highest basalt Vp ($\sim$5,000 m s^{-1}) on Line A North (Figure 5a) occurs where the PSDM image shows a strong coherent reflection, suggesting a smooth basalt surface (between x = 100–300 m and 1,200–2,000 m). On the edges of these sections, Vp is not as well constrained due to a lack of data coverage. However, basalt Vp is lower at transitions in reflection coherence. These areas may represent a rubbly basalt surface or a region of increased fracture density where communication between the unconfined and confined aquifers could potentially occur. However, well observations are needed to confirm this.

At profile distances greater than 3,000 m for Line A North, Vp in the basalt is $\sim$3,500–4,500 m s^{-1}, and the reflection image indicates several discontinuities. Here, the low Vp along the top of the basalt is well constrained and may indicate fractured and permeable basalt. The combination of low basalt Vp and discontinuous structure in the PSDM image supports an interpretation of folded and/or fractured basalt.

Basalt Elevation Map

The 3,000-m s^{-1} Vp contour marks the transition from suprabasalt sediments to basalt and shows good agreement with well observations (Figures 5 and 6). There are a few sections of Line A North where the top of the basalt is too deep to be imaged with the 196-m streamer offset, and these are areas where paleochannels carved through the basalt have been previously interpreted (Sunwall et al., 2011). Here, the PSDM images were used to interpret basalt elevation with the understanding that they may be biased toward overly deep estimates.

Combining the depth to Vp = 3,000 m s^{-1} where it is well constrained with PSDM interpretations and well observations yields a two-dimensional visualization of the basalt surface in the Gable Gap area. Figure 8 shows a minimum curvature surface fit to the data masking everywhere in the study area that is more than 250 m away from an observation. It shows a complex basalt surface consistent with previous interpretations of paleo-channels and second-order syncline anticline pairs superimposed on the southern limb of the GMA.

Most of the variation in basalt elevation is supported by the seismic results; however, well observa-
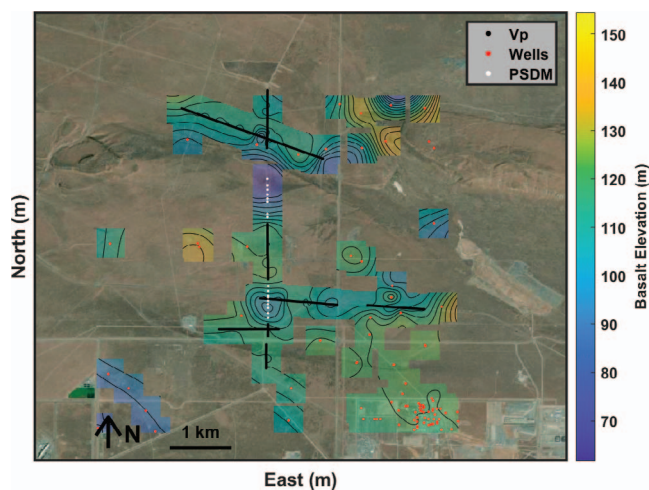
Figure 8. Minimum curvature surface fit to well data (red dots), interpreted depths to Vp = 3,000 m s^{-1} (black lines), and basalt elevations interpreted from reflections on Line A North, where refractions do not constrain basalt elevation (white dots).

tions also show large variations over short distances. For example, two wells north of Line C East show elevation differences of 24 m over a distance of 190 m.

Variations in Shallow Vs and Vp

Both the Vp- and the Rayleigh wave–derived Vs images indicate lateral variations in shallow (<20 m deep) sediment properties. These variations likely represent changes in grain size distribution or sandy versus gravelly deposits of the Hanford formation. For example, the dashed lines in Figures 5b and 6b indicate an interpreted boundary between the sandy H2 and the gravel-dominated H3 unit. Given the different grain size distribution in each unit, a difference in porosity and hydraulic conductivity is also expected, and variations in the distribution and thickness of these two units may impact vertical fluid infiltration and unsaturated flow within the vadose zone. Future studies with lower-frequency geophones could potentially image deeper Vs structure and provide the possibility of using Vp/Vs ratios to discriminate between dry and saturated conditions.

CONCLUSIONS

The seismic landstreamer is an effective tool for characterizing near-surface hydrostratigraphy at the Hanford Site. While previous work (Hyde et al., 2011; Sunwall et al., 2011) focused on the reflected wave field, this analysis demonstrates that the refraction and Rayleigh wave data can provide additional information on basalt elevations and properties.

The integration of reflection, refraction, Rayleigh wave data, and borehole information has revealed previously undetected features within the study area. The refraction data provided an updated estimate of basalt elevation and allowed the identification of low-velocity zones that coincide with discontinuities in the reflection images. These low-velocity zones may be indicative of fractures supporting vertical communication between the confined and unconfined aquifers. Integrating well observations with the seismic interpretations suggests that the refraction approach provided basalt elevation estimates that agree more closely with well observations compared to PSDM. Both methods support the interpretation of a highly variable basalt surface. Vs structure derived from Rayleigh wave analysis was broadly consistent with Vp structure in the upper 10–20 m, indicating variations in the distribution of Hanford formation units. This information, along with continuing geophysical investigations, will be used to refine the site geologic model.

ACKNOWLEDGMENTS

REFERENCES

AJO-FRANKLIN, J. B.; MINSLEY, B. J.; AND DALEY, T. M. 2007, Applying compactness constraints to differential travel-time tomography: *Geophysics*, Vol. 72, No. 4, doi:1190/1.2742496

AKI, K. AND P. G. RICHARDS, 2002, *Quantitative Seismology:* W. H. Freeman, New York.

AULT, T. D., 1981, Appendix D—Geophysical investigations of the Gable Mountain-Gable Butte Area. In Myers, C. W. AND Price, S. M. (Editors), *Subsurface Geology of the Cold Creek Syncline Area:* RHO-BWI-ST-14, Rockwell Hanford Operations, Richland, WA, pp. D-1–D-24.

BJORNSTAD, B. N.; THORNE, P. D.; WILLIAMS, B. A.; LAST, G. V.; THOMAS, G. S.; THOMPSON, M. D.; LUDWIG, J. L.; AND LANIGAN, D. C., 2010, *Hydrogeologic Model for the Gable Gap Area, Hanford Site:* PNNL-19702, Pacific Northwest National Laboratory, Richland, WA.

CUMMINS, G. D., 2009, *Reflection Seismic Survey Report, 200 East Area:* Hanford Site, Rev 0: CH2MHILL Plateau Remediation Company Document SGW-39675, 60 p.

DE WIT, R. W. L.; TRAMPERT, J.; AND VAN DER HILST, R. D., 2012, Toward quantifying uncertainty in travel-time tomography using the null-space shuttle: *J. Geophys. Res.*, Vol. 117, No. B3, pp. 1–20.

DOE/RL (U.S. DEPARTMENT OF ENERGY, RICHLAND OPERATIONS OFFICE), 2012, *Hanford Site Groundwater Monitoring for 2011:* DOE/RL-2011-118, U.S. Department of Energy, Richland Operations Office, Richland, WA.

GRAHAM, M. J.; LAST, G. V.; AND FECHT, K. R., 1984, *An Assessment of Aquifer Intercommunication in the B Pond-Gable Mountain Pond Area of the Hanford Site:* RHO-RE-ST-12P, Rockwell Hanford Operations, Richland, WA.

HARTMAN, M. J.; RICHIE, V. S.; AND REDIKER, J. A., 2009, *Hanford Site Groundwater Monitoring for Fiscal Year 2008:* CH2M Hill Plateau Remediation Company Document DOE/RL-2008-66 Draft A, U.S. Department of Energy, Richland, WA.

HUBBARD, S. S. AND N. LINDE, N., 2010, *Hydrogeophysics,* https://www.osti.govs-1ervlets/purl/1007490

HYDE, E. R.; SPEECE, M. A.; LINK, C. A.; REPASKY, T. R.; THOMPSON, M. D.; AND MILLER, S. F., 2011, A seismic landstreamer survey at the Hanford Site, Washington, U.S.A.: Environmental and Engineering Geoscience, doi:10.2113/gseegeosci.17.3.227

IVANOV, J.; MILLER, R. D.; AND TSOFLIAS, G., 2008. Some Practial Aspects of MASW Analysis and Processing: SAGEEP, https://doi.org/10.4133/1.2963228

MAVKO, G.; MUKERJI, T.; AND DVORKIN, J., 2009, *The Rock Physics Handbook: Tools for Seismic Analysis of Porous Media,* 2nd ed.: Cambridge University Press, Cambridge, U.K.

MIKESELL, T. D.; GRIBLER, G.; XU, Z.; AND HANEY, M. M, 2017. High resolution dispersion images from deblurred MASW: SEG Technical Program Expanded Abstracts, https://doi.org/10.1190s-1egam2017-17650859.1

MOSER, T. J., 1991, Shortest path calculation of seismic rays: *Geophysics*, Vol. 56, No. 1, pp. 59–67.

PARK, C. B.; MILLER, R. D.; AND XIA, J., 1999, Multi-channel analysis of surface waves: *Geophysics*, Vol. 64, No. 3, pp. 800–808.

ROHAY, A. C. AND BROUNS, T. M., 2007, *Site Specific Velocity and Density Model for the Waste Treatment Plant, Hanford, Washington:* PNNL-16652, Revision 1, Pacific Northwest National Laboratory, Richland, WA.

SHEARER, P. M., 1999, *Introduction to Seismology:* Cambridge University Press, Cambridge, U.K., 272 p.

SHERIFF, R. E. AND GELDART, L. P., 1995, *Exploration Seismology*, 2nd ed.: Cambridge University Press, Cambridge, U.K., 253 p.

SSC (SEISMOGRAPH SERVICE CORPORATION), 1979, *Final Report on a Seismic Reflection Survey Conducted in Benton and Grant Counties, Washington, Pasco Basin, Hanford Site, Basalt Waste Isolation Program:* B067305, Seismograph Service Corporation for Rockwell Hanford Operations, Richland, WA, MF 1857.

SSC (SEISMOGRAPH SERVICE CORPORATION), 1980, *Final Report on a Seismic Reflection Survey Conducted in Benton County, Washington, FY-80 Program, Pasco Basin, Hanford Site, Basalt Waste Isolation Program:* B067306, Seismograph Service Corporation for Rockwell Hanford Operations, Richland, WA, MF 1858.

ST. CLAIR, J., 2015, *Geophysical Investigations of Underplating at the Middle American Trench, Weathering in the Critical Zone, and Snow Water Equivalent in Seasonal Snow:* Ph.D. thesis, University of Wyoming.

ST. CLAIR, J. AND LIBERTY, L. M., 2019, Combined first arrival, Rayleigh wave and P-SV converted wave analysis for improved hydrologic characterization: SEG Technical Program Expanded Abstracts, https://doi.org/10.1190s-1egam2019-3216844.1

STEEPLES, D. W., 2005, Shallow seismic methods. In Rubin, Y. AND Hubbard, S. S. (Editors), *Hydrogeophysics*, Vol. 50: Springer, Dordrecht, Netherlands, pp. 215-251.

Sunwall, D. A.; Williams, B. P.; Repasky, T. R.; Link, C. A.; and Speece, M. A., 2011, *Landstreamer and Gimballed Geophones Phase II–200 Areas: A High Resolution Seismic Survey at the Hanford Site:* SGW-52160 Revision 0, Pacific Northwest National Laboratory, Richland, WA.

Williams, B. A.; Thompson, M. D.; and Miller, S. F., 2011, *Interpretation and Integration of Seismic Data in the Gable Gap:* CH2M Hill Plateau Remediation Company, Richland, WA.

Xia, J.; Miller, R. D.; and Park, C. B., 1999, Estimation of near-surface shear-wave velocities by inversion of Rayleigh waves: *Geophysics*, Vol. 64, No. 3, pp. 691–700.

Possible Fault Communication between the Memphis Sand Aquifer and the Mississippi River

RICHARD V. MARTIN*

St. Simons Island, GA 31522

ROY B. VAN ARSDALE
VALARIE J. HARRISON

Department of Earth Sciences, University of Memphis, Memphis, TN 38152

Key Terms: *Memphis Sand, Memphis Aquifer, Faulting, Aquifer, Shelby County, Tennessee*

ABSTRACT

The Eocene Memphis Sand aquifer is the major source of drinking water for municipalities in the upper Mississippi Embayment, with the city of Memphis, TN, being the largest consumer. Concerns about contamination of the Memphis aquifer from surface waters have primarily focused on local groundwater transmission through the Upper Claiborne aquitard and erosional windows through the aquitard. This study used recent fault mapping to show that faults extend upward from the Memphis aquifer to very near the surface in and adjacent to Memphis. The Meeman-Shelby and Cuba faults extend under the Mississippi River and upward to the base of the Mississippi River alluvium. Groundwater levels (potentiometric surface) in Memphis aquifer monitor wells H002 and LdF 004 and the Mississippi River water levels during the years of 2007 through 2011 show strong correlation (0.744829 and 0.779691, respectively). We believe this correlation may be due to direct connection through fault zones.

INTRODUCTION

The Memphis aquifer serves western Tennessee and particularly the city of Memphis and Shelby County as the primary source of potable water. Production from the Memphis aquifer is approximately 794 ML/d in Memphis (Maupin et al., 2014). Water quality of the Memphis aquifer was thought to be very good throughout the aquifer (Parks and Carmichael, 1990c), but Larsen et al. (2003) reported that water quality is better in the lower portion of the aquifer than in the upper portion. They attributed this quality difference to seepage of surface water into the upper portion of the Memphis aquifer. The lower Memphis aquifer beneath Shelby County carries old water from outcrop recharge in Fayette County and is unaffected by modern surface waters (Figure 1).

The most serious potential problem with groundwater quality in the Memphis aquifer is contamination from surface leakage down into the aquifer. Garbage dumps and various contaminate spills are a major concern where the overlying aquitard is absent, thin, or faulted. The aquifer is thick and continuous with good quality water and recharge. If the aquifer can be protected from contamination, the Memphis aquifer should be able to continue to meet the needs of its users.

Possible leakage and recharge from surface waters into the Memphis aquifer have been discussed by several authors (Parks, 1990; Parks and Carmichael, 1990a; Kingsbury and Parks, 1993; Larsen et al., 2003; Carmichael et al., 2018; and Towell, 2021). This paper focuses on possible communication between surface water and subsurface Memphis aquifer water along recently mapped faults in the Memphis area (Hao et al., 2013; Martin and Van Arsdale, 2017) (Figure 1).

Stratigraphy of Shelby County

The Memphis Sand (Memphis aquifer) is composed primarily of fine to coarse sand. It also includes clay, silt, and lignite units (Parks and Carmichael, 1990c) and is up to 275 m (902 ft) thick beneath Shelby County (Martin, 2008). In ascending order, the Eocene Memphis Sand is overlain by the Eocene Cook Mountain Formation, Eocene Cockfield Formation, Pliocene Upland Complex, Pleistocene loess, and Pleistocene–Holocene alluvium (Figure 2). The Cook Mountain Formation is a low-permeability, predominately clay unit, and the Cockfield Formation is an interbedded sand and clay unit. When combined, these two formations serve as the overlying Upper Claiborne aquitard of the Memphis Sand aquifer (Graham and Parks, 1986). Underlying the Memphis Sand, there is the Flour Island Formation. This generally silty clay

*Corresponding author email: docrvmartin@gmail.com
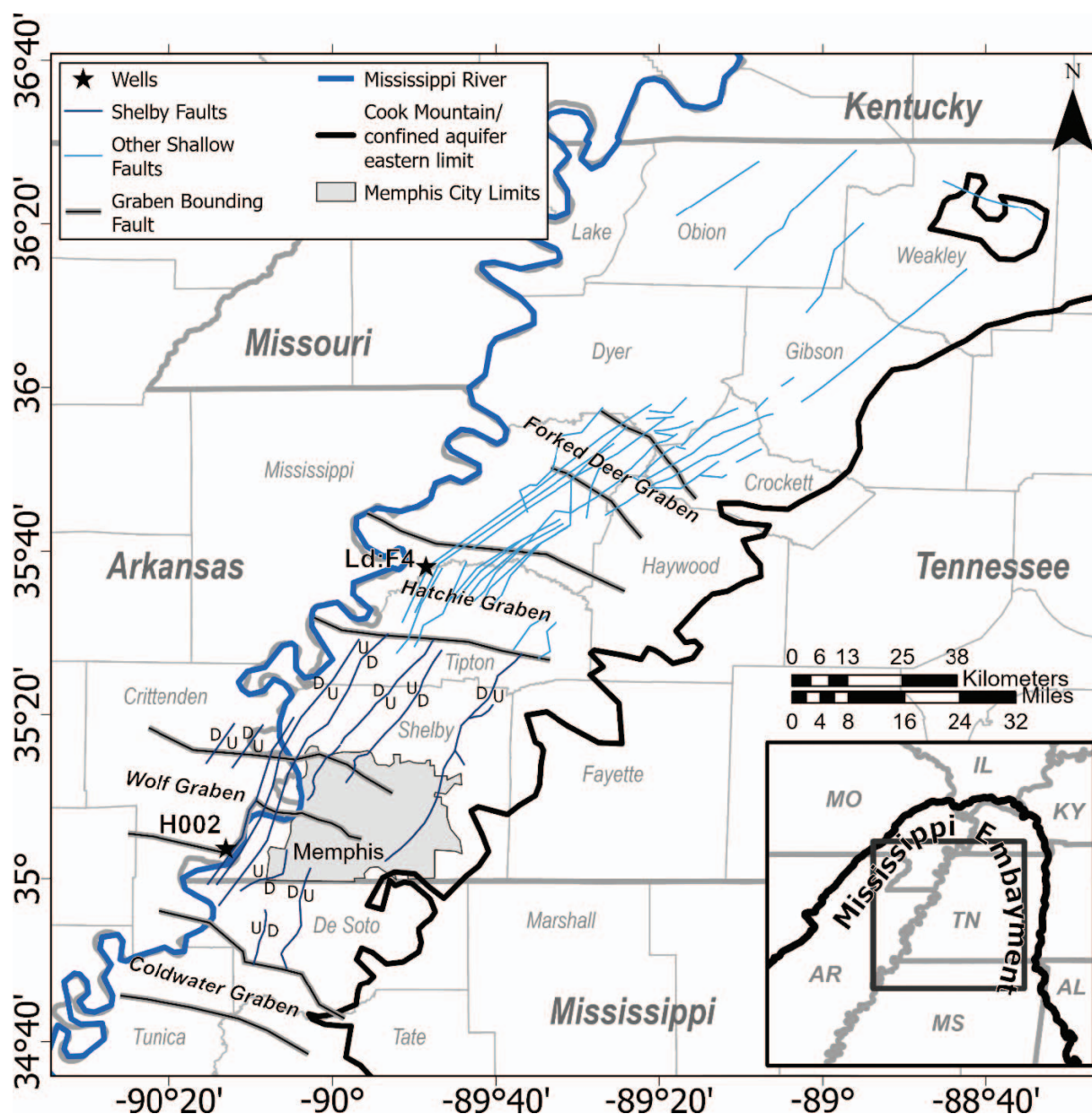
Figure 1. Location map showing western Tennessee faults, LdF 004 (LdF4) well, and H002 well. Faulting is after Martin and Van Arsdale (2017).

unit is the aquitard beneath the Memphis aquifer, which in turn overlies the Fort Pillow Sand aquifer. The Eocene Fort Pillow aquifer is the deepest aquifer in west Tennessee, and it provides approximately 5% of municipal and industrial water (Graham and Parks, 1986).

Memphis Sand Aquifer

Recharge of the Memphis aquifer is from its outcrop belt, beneath Mississippi River tributaries, and through sand facies, erosional windows, and faults through the Upper Claiborne aquitard (Figures 1 and 3) (Parks and Carmichael, 1990a,b). Precipitation and stream-bottom infiltration into the Memphis Sand outcrop belt (unconfined Memphis aquifer) are the principal recharge routes to recharge the Memphis aquifer, after which the water flows westward and northwestward down-gradient along the ~1° structural dip (Larsen et al., 2022). The potentiometric surface of the Memphis aquifer slopes gently westward and northwestward at approximately 0.5 m/km where the aquifer is confined (Figure 1).

		W Tennessee		
Quaternary	Holocene	Alluvium		
	Pleistocene	Loess & Alluvium		
Neogene	Pliocene	Upland Complex		
Paleogene	Eocene			Jackson Fm
		Claiborne		Cockfield Fm
				Cook Mountain Fm
				Memphis Sand
		Wilcox		Flour Island Fm
				Fort Pillow Sand
	Paleocene			Old Breastworks Fm
		Midway		Porter's Creek Clay
				Clayton Fm

Figure 2. Cenozoic stratigraphic section of western Tennessee and eastern Arkansas.

A significant feature in the Memphis aquifer potentiometric surface is a cone of depression under Memphis, which was reported by Parks and Carmichael (1990a) to be the result of over 100 years of water removal (Figure 3). The cone of depression is now stable, indicating that recharge of the aquifer has reached equilibrium with withdrawal.

All the groundwater monitor wells in this study (Figure 3) show a seasonal rise and fall of water levels, with the high levels occurring in the late winter and spring and the low levels occurring in the summer and fall. This seasonal rise and fall pattern is also present in Mississippi River water levels. Parks and Carmichael (1990a) described the water level in the LdF 004 groundwater monitor well (Figures 1 and 3) as fluctuating with the Mississippi River level. The LdF 004 monitor well is in Lauderdale County, north of Memphis, and it is 5 km from the Mississippi River. Well LdF 004 sits atop the loess-covered bluffs at a surface elevation of 133.2 m (437 ft). The Memphis aquifer water levels rise and fall in well LdF 004 in parallel with rising and falling stages in the Mississippi River. Correlation of Memphis aquifer water levels in the LdF 004 monitor well with water levels in the Mississippi River was explained by Parks and Carmichael (1990a) as due to pressure variation in the Memphis aquifer because of Mississippi River water loading. A similar correlation (Anderson, 2005) occurs between the Memphis aquifer water level and Mississippi River stage in the H002 groundwater monitoring well in Crittenden County, AR, 15 km west of Memphis (Figures 1 and 3).

Where the groundwater potentiometric surface is depressed, such as beneath Memphis, the Memphis aquifer may recharge from the overlying Cockfield Formation or modern river alluvium. This is particularly true if the potentiometric depression is at, or near, areas where the overlying Upper Claiborne aquitard is thin, sandy, absent, and/or faulted (Carmichael et al., 2018). The eastern limit of the Upper Claiborne aquitard is a sinuous erosional contact, and there are several windows through the aquitard in Shelby County (Figures 1 and 3). Faulting locally cuts through the Memphis Sand and the overlying aquitard (Figures 3 and 4). Surface drainage along a portion of Nonconnah Creek in south Memphis leaks into the Memphis aquifer where faulting apparently puts the aquifer into communication with the surface drainage (Kingsbury and Parks, 1993; Larsen et al., 2003). Depending upon the potentiometric surfaces at these locations, the Memphis aquifer may be recharged or may expel water along faults (Parks and Carmichael, 1990a).

Possible Fault Communication between Memphis Aquifer and Surface Water

Vertical fault displacement reaching to or near the ground surface in and adjacent to Memphis has been described on the Meeman-Shelby Fault (Williams et al., 2001; Hao et al., 2013; and Van Arsdale et al., 2017), Ellendale Fault (Velasco et al., 2005; Deen, 2006; and Van Arsdale et al., 2012), and Memphis Fault (Velasco et al., 2005; Van Arsdale et al., 2012) (Figures 1 and 3). High-resolution seismic reflection profiles gathered primarily along the Mississippi River show the down-to-the-east Meeman-Shelby Fault extending through the Memphis aquifer upward into the Mississippi River valley alluvium and locally under the Mississippi River (Figures 3 and 4) (Hao et al., 2013; Van Arsdale et al., 2017). Martin and Van Arsdale (2017) mapped the down-to-the-west Cuba Fault that is sub-parallel to the Meeman-Shelby Fault (Figure 3). The Cuba Fault extends upward to the base of the Mississippi River alluvium. Martin and Van Arsdale (2017) also mapped the Wolf and Hatchie graben faults, which are west oriented and extend under the Mississippi River and its alluvium (Figure 3).

Carmichael et al. (2018) described communication between the Memphis aquifer and the surface Mississippi River alluvium at the Tennessee Valley Authority (TVA) Allen plant in Shelby County about 1.6 km (1 mile) east of the Mississippi River (Figure 3). They attributed the communication to local poor quality of the aquitard, a possible erosional window in the aquitard, and/or possible fault communication. Carmichael et al. (2018) mapped two faults at and near the TVA plant site. Their SW/NE-oriented fault lies across the plant site and within their well test pattern. Their north-oriented fault equates to the Cuba Fault of Martin and Van Arsdale (2017). The SW/NE fault indicates cross-faulting within the graben between the Meeman-Shelby and Cuba faults, which adds to the
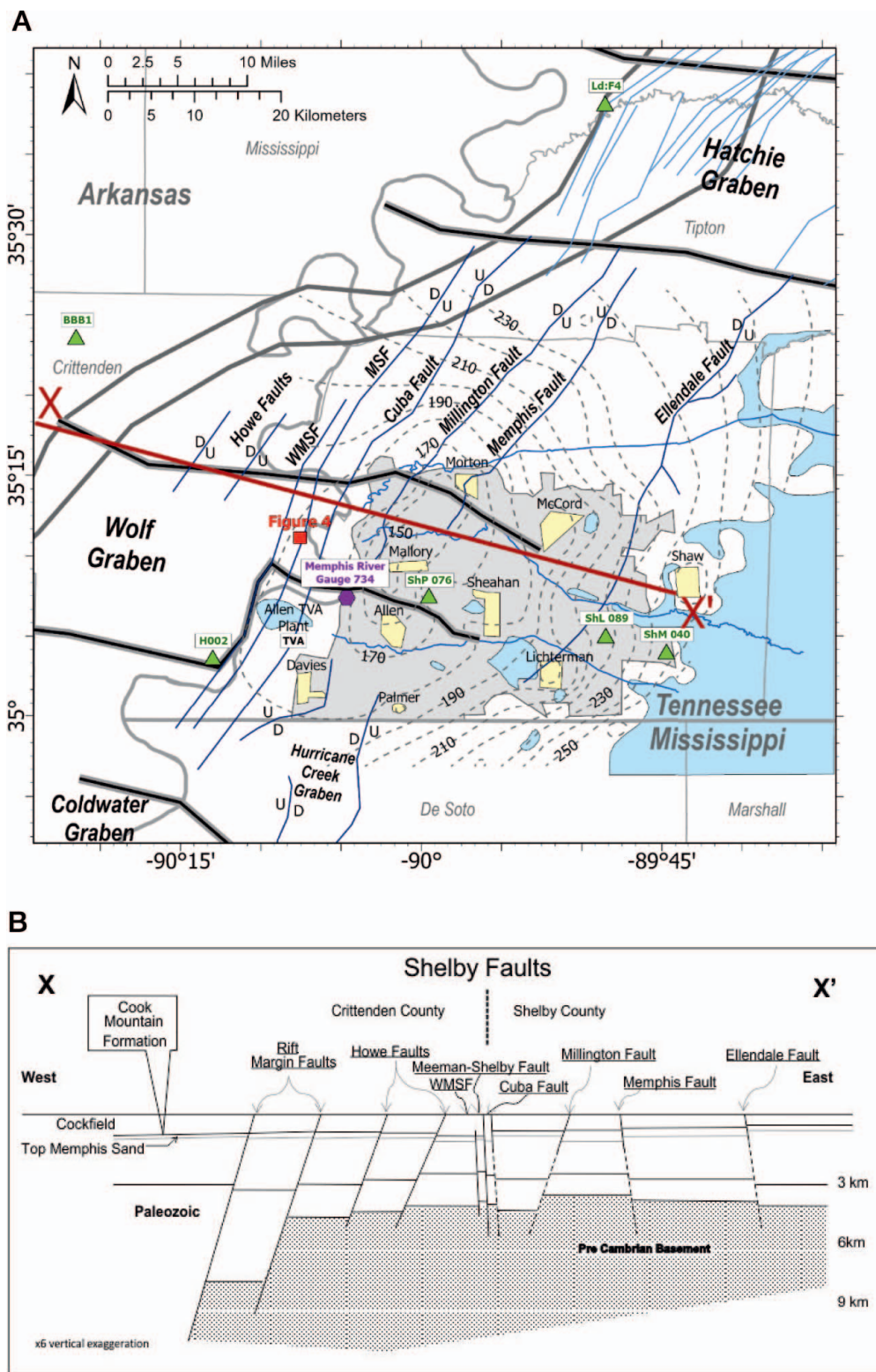
Figure 3. (A) Map of the study area faults, Shelby County, Memphis aquifer potentiometric surface (dashed contours in ft), with cone of depression from Kingsbury (2018), Memphis River Gauging Station 734, TVA Allen plant, groundwater monitoring wells used in this study, water fields (yellow), windows in Upper Claiborne aquitard (blue) from Parks (1990), location of seismic line in Figure 4, and cross section X-X′ location. (B) Cross section X-X′.

Figure 4. Faults within the Meeman-Shelby fault zone displace Upper Claiborne and Holocene Mississippi River alluvium. Seismic line "A" is shown in Figure 3. Red line in A is top of Memphis Sand aquifer. Base of Mississippi River alluvium is 36.5 m (120 ft) in bore hole MS-2 (from Van Arsdale et al., 2017). Line C shows faults extending to near to the top of the Mississippi River floodplain.

number of potentially hydrologically communicative faults. Towell (2021) conducted a groundwater tracer survey and documented downward vertical movement of surface water through at least two different faults, putting the Memphis aquifer in communication with near-surface waters at Davis wellfield.

In discussing the stratigraphic control of the water levels in the Mississippi River alluvium and in

Table 1. *Correlation (R^2 values) between elevation of groundwater in monitoring wells in the Memphis Sand aquifer and Mississippi River stage elevations at the Memphis Mississippi River Gauging Station 734 for the years 2007 through 2011.*

Year	H002	LdF 004	BBB1	ShP 076	ShM 040	ShL 089
2007	0.808366	0.698123	0.651042	0.76291	0.724334	− 0.602999
2008	0.788064	0.876068	0.682933	0.592383	0.606767	− 0.523419
2009	0.699002	0.529907	0.114983	0.788901	0.613209	0.042464
2010	0.892289	0.839887	0.784258	0.607769	0.513163	0.453653
2011	0.857658	0.87697	0.437711	0.721305	− 0.48902	0.154066
2007–2011	0.809076	0.779691	0.547259	0.628341	0.282481	0.090687

the Cockfield Formation, Parks et al. (1985) described probable communication through leakage due to local thinning and ineffective quality of confining beds separating the two units. They then described the presence of faulting that may put the Memphis aquifer and Cockfield Formation in direct hydrologic connection.

The Memphis aquifer and the Mississippi River appear to be in communication, as shown by water-level data from the LdF 004 and the H002 monitor wells (Figures 1 and 3–5). The question is whether the correlation between the groundwater levels and Mississippi River stages is caused by Mississippi River water loading, as suggested by Parks et al. (1985), hydrologic communication through a locally transmissive aquitard, or communication along faults.

Parks et al. (1985) did not map faulting in any detail in their paper. However, they did map a northwest-trending fault near the LdF 004 well roughly equivalent to the Hatchie graben north fault and a northeast-trending fault that we interpret to be one of the Lauderdale faults (Figures 1 and 3) (Martin and Van Arsdale, 2017). More recent mapping in western Tennessee has documented more extensive surface and near-surface faulting in and adjacent to Shelby County (Figures 1, 3, and 4) (Cox et al., 2001, 2006; Van Arsdale et al., 2012, 2017; Hao et al., 2013; and Martin and Van Arsdale, 2017).

We believe surface water may be passing down to the Memphis aquifer through fault leakage (Figure 3). Bense and Person (2006) discussed the mechanics of fault leakage in poorly lithified siliciclastic sediments. Anisotropic permeability along faults is a function of depth of burial, throw along the fault, and clay content of the faulted units. Lateral permeability may be greatly limited by higher clay content and smearing on either side of the fault, sand drag, and grain reorientation. Vertical segmentation of the fault plane, which may be a function of lithology on either side of the fault plane and throw, can also lead to increased vertical permeability and decreased lateral permeability.

In poorly lithified sediment, fault movement can cause clay to smear parallel to the fault plane, but it also drags sand grains into the fault damage zone.

More fault displacement and more clay can reduce lateral permeability. However, more vertical fault displacement may lead to more sand being dragged into the fault damage zone, thereby increasing vertical permeability. Bense and Person (2006) applied this idea to sediment above 500 m depth. Our investigation was within 200 m of the ground surface and thus within the depth range of the Bense and Person (2006) study.

A further concern is that faults may extend through the full thickness of the Memphis Sand (Figure 3). Bense and Person (2006) showed that communication along faults can extend well into the aquifer, which in our study is the thick Memphis Sand, and potentially allow contamination deep into the Memphis aquifer.

RESULTS

The Mississippi River water level varies in an annual pattern, with high water in the late winter and spring due to spring snowmelt and increased rain. Annual low water level occurs in the summer and fall (U.S. Army Corp of Engineers data, https://rivergages.mvr.usace.army.mil/). Mississippi River water levels were accessed from Mississippi River Gauge Station 734 along the Tennessee/Arkansas border (Figure 3) for the time period from January 1, 2007, to December 31, 2011. We chose to make all groundwater level correlations with Gauge 734 because it is approximately in the middle of the six groundwater monitor wells evaluated in this study (Figure 3). These six Memphis aquifer groundwater monitoring wells had complete daily water levels for January 1, 2007, through December 31, 2011 (U.S. Geological Survey data, https://waterdata.usgs.gov/tn/nwis/gw and https://waterdata.usgs.gov/ar/nwis/gw). The geographic distribution of the six wells covered the study area of southwest Tennessee and adjacent Arkansas: LdF 004 well in Lauderdale County, TN; the ShM 040, ShL 089, and ShP 076 wells in Shelby County, TN; and the BBB1 and H002 wells in Crittenden County, AR (Figure 3). All six wells were compared to the Mississippi River Gauge 734 using the Correlation tool in Excel (Table 1).
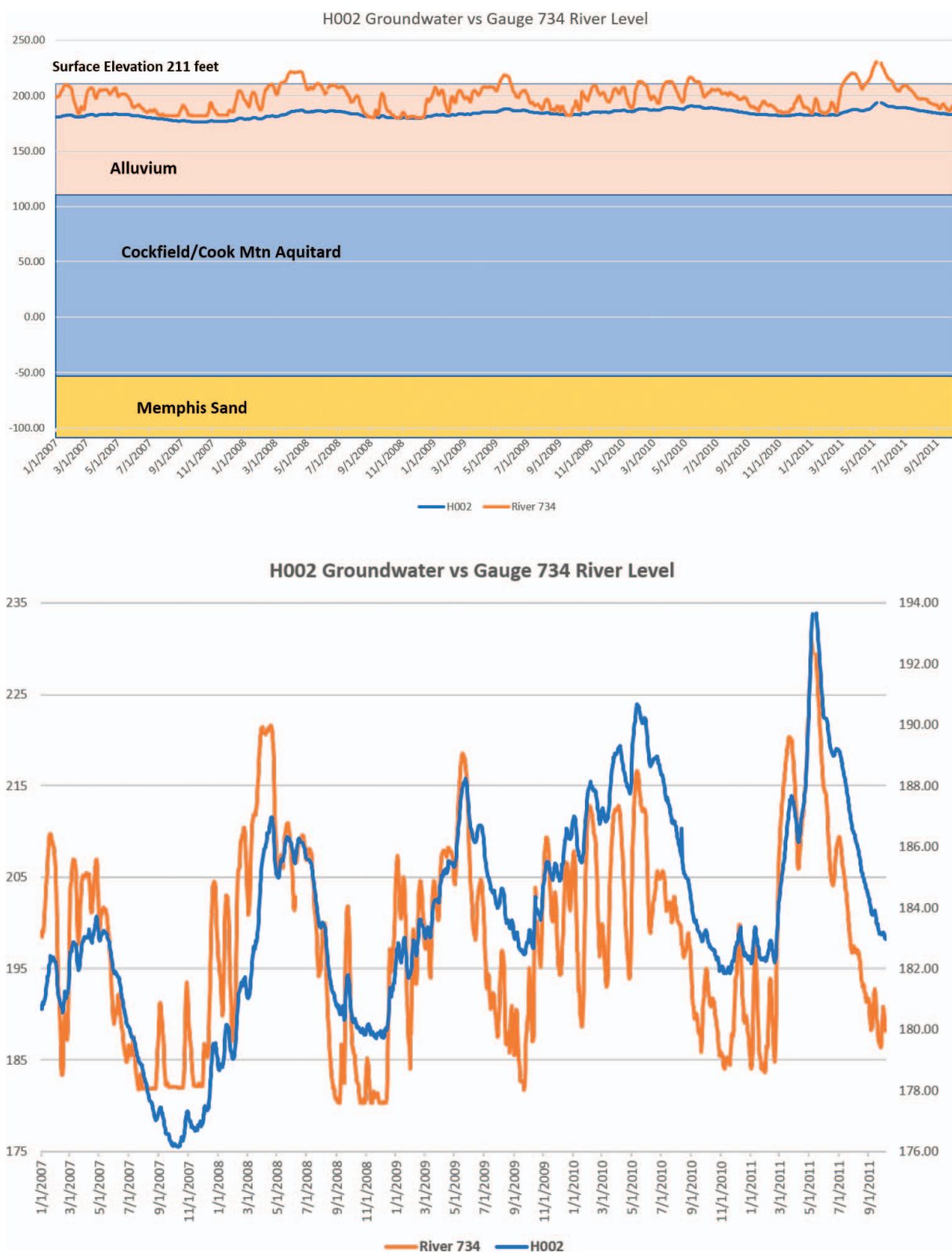
Figure 5. Graphs showing Mississippi River water levels (orange) and H002 groundwater levels (blue) from January 1, 2007, through September 1, 2011.
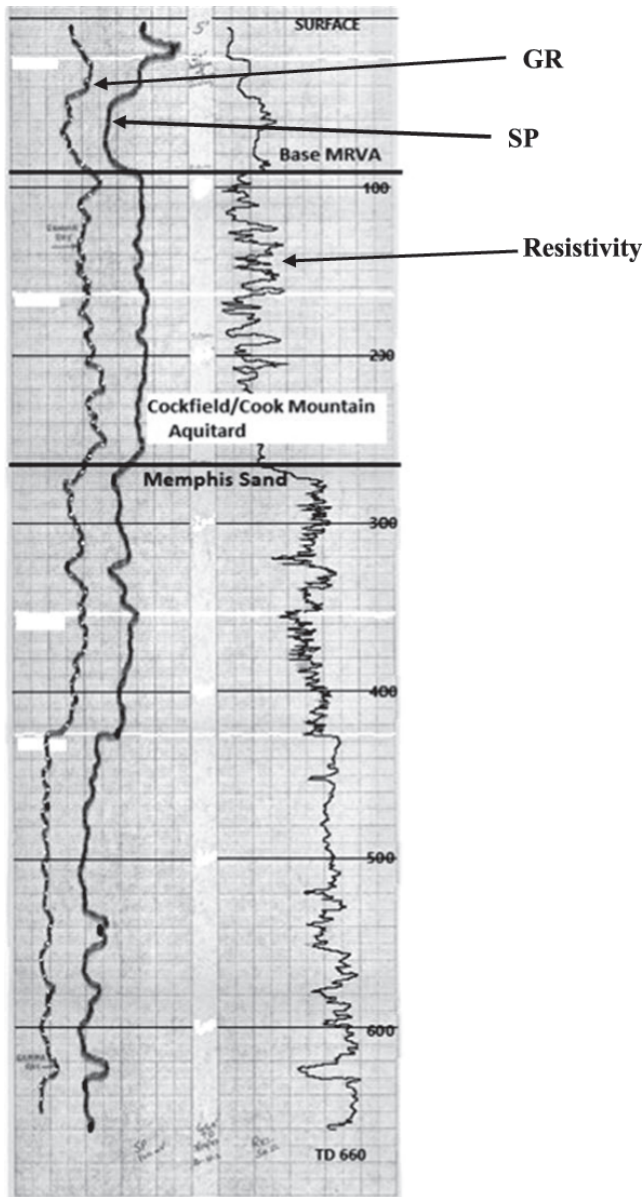
Figure 6. Geophysical log of the H002 groundwater monitoring well with tops. Depths are shown in ft because the original log was measured in feet. The Upper Claiborne aquitard is 175 ft (53 m) thick.

During the time interval of January 1, 2007, through December 31, 2011, correlation coefficients for water elevation in wells BBB1, ShP 076, ShM040, and ShL089 and Mississippi River stages are low (Table 1). However, during this same time, the correlation for well H002 was 0.809076, and that for well LdF 004 was 0.779691.

DISCUSSION

Six monitoring wells with daily groundwater elevation data were compared to Mississippi River water surface elevations at Gauge 734 (Table 1). The Mississippi River has a seasonal pattern of higher water levels in the late winter and in the spring, with low water levels in the summer and fall. Four of the wells (LdF 004, ShP 076, ShM 040, and ShL 089) are located on the loess-covered bluff (Figure 3) east of the Mississippi River. Wells ShP 016, ShM 040, and ShL 089 showed low correlation to the Mississippi River stages (Table 1). The BBB1 monitoring well is on the Mississippi River floodplain, approximately 12 km from the Mississippi River, and it too had a low correlation with the Mississippi River stage.

There are several reasons why correlation between the river and these wells could be low. One obvious reason is distance from the river. However, the BBB1 is 12 km west of the river and had a correlation of 0.547279. The ShL 089 is 12 km east of the river and had a correlation of 0.282481. The ShM 040 is 14 km east of the river and had a correlation of 0.090687. Another factor for poor correlation could be local water production, particularly high-volume production in the city of Memphis. The two eastern wells, ShL 089 and ShM 040, are near three wellfields. The BBB1 is not close to a wellfield but is in an area of intermittently high irrigation water usage.

Water levels in wells LdF 004 and H002 and Mississippi River stage showed high correlation coefficients (0.779691 and 0.809076, respectively). Well LdF 004 is 5 km east of the Mississippi River and located 60 m (200 ft) above the Mississippi River alluvial surface on a narrow loess-covered, east/west-oriented ridge with Mississippi River alluvium on both the north and south flanks of the ridge. Well H002 sits on the Mississippi River floodplain 2.5 km west of the Mississippi River (Figure 3). Wells H002 and LdF 004 (Figure 3) are underlain by 53 m and 54 m, respectively, of Upper Claiborne aquitard (Figure 6), and there is no evidence that the aquitard is of poor quality near the wells. Studies looking for windows in the aquitard in Shelby County (Parks, 1990; Larsen et al., 2022) have not found any windows close to well H002.

The H002 well is very close to the Meeman-Shelby faults (Figures 1, 3, and 4), which trend under the Mississippi River and extend upward into the Mississippi River floodplain alluvium (Van Arsdale et al., 2017). Similarly, well LdF 004 appears to have been drilled into the NE-trending Lauderdale fault zone (Figures 1 and 3).

CONCLUSIONS

The correlation coefficients between the Mississippi River Gauge Station 734 and groundwater levels in monitoring wells BBB1, ShP 076, ShM 040, and ShL 089 were less than 0.63. If, as proposed by Parks et al.

(1985), water levels in the Memphis Sand are controlled by pressure in the Memphis aquifer caused by Mississippi River stages, then we would expect to see higher correlation coefficients among all of the monitoring wells and Mississippi River stage (Table 1). However, the correlation coefficient (0.809076) between the water level in the H002 groundwater monitoring well and the Mississippi River Gauge Station 734 may indicate direct communication between Mississippi River surface water and the Memphis Sand aquifer along a fault. The faults most likely responsible for this communication are the Meeman-Shelby faults (Figures 3 and 5) (Hao et al., 2013; Van Arsdale et al., 2017). Similarly, we postulate that the high correlation (0.779691) between Mississippi River water stage and the water level in the LdF 004 Memphis aquifer monitoring well is due to water moving through the Upper Claiborne aquitard along a Lauderdale fault.

This postulated fault communication raises the concern of potential contamination of the Memphis aquifer by the Mississippi River or other surface contamination. Possible contamination of the Memphis aquifer should also be a concern wherever faulting extends to, or near to, the ground surface throughout the Shelby County area. The principal faults of concern are the Howe, Meeman-Shelby, Millington, Memphis, Hurricane Creek, Ellendale, and Wolf graben faults (Figure 3). We recommend that east-west seismic reflection lines should be acquired across the H002 and LdF 004 monitoring well sites to determine whether a near-surface fault is indeed close to these wells. If this relationship is confirmed, then the other Memphis area faults in Figure 3 should be investigated for potential avenues of contamination of the Memphis aquifer.

REFERENCES

ANDERSON, J. L., 2005, Development of a transducer network in an urban environment. In *Proceedings of the Fifteenth Tennessee Water Resources Symposium*, pp. IC14–IC25.

BENSE, V. F. AND PERSON, M. A., 2006, Faults as conduit-barrier systems to fluid flow in siliciclastic aquifers: *Water Resources Research*, Vol. 42, W05421. doi:10.1029/2005WR004480

CARMICHAEL, J. K.; KINGSBURY, J. A.; LARSEN, D.; AND SHOEFERNACKER, S., 2018, *Preliminary Evaluation of the Hydrogeology and Groundwater Quality of the Mississippi River Valley Alluvial Aquifer and Memphis Aquifer at the Tennessee Valley Authority Allen Power Plants, Memphis, Shelby County, Tennessee*: U.S. Geological Survey Open-File Report 2018-1097, 66 p.

COX, R. T.; CHERRYHOLMES, J.; HARRIS, J. B.; LARSEN, D.; VAN ARSDALE, R. B.; AND FORMAN, S. L., 2006, Paleoseismology of the southeastern Reelfoot Rift in western, Tennessee, U.S.A., and implications for intraplate fault zone evolution: *Tectonics*, Vol. 25, TC3019. doi:10.1029/2005TC001829

COX, R. T.; VAN ARSDALE, R. B.; AND HARRIS, J. B., 2001, Identification of possible Quaternary deformation in the northeastern Mississippi Embayment using quantitative geomorphic analysis of drainage-basin asymmetry: *Geological Society of America Bulletin*, Vol. 113, pp. 615–624. doi:10.1130 0016-7606(2001)113<0615:IOPQDI>2.0.CO;2

DEEN, T. S., 2006, Quaternary fault investigation of southern Shelby County, Tennessee, University of Memphis MS thesis, 93 p.

GRAHAM, D. D. AND PARKS, W. S., 1986, *Potential for Leakage Among Principal Aquifers in the Memphis Area, Tennessee*: U.S. Geological Survey Water-Resources Report 85-4295, 46 p.

HAO, Y.; MAGNAMI, M. B.; MCINTOSH, K.; WALDRON, B.; AND GUO, L., 2013, Quaternary deformation along the Meeman-Shelby fault near Memphis, Tennessee, imaged by high resolution marine and land seismic reflection profiles: *Tectonics*, Vol. 32, pp. 501–515. doi:10.1002/tect.20042

KINGSBURY, J. A., 2018, *Altitude of the Potentiometric Surface, 2000–15, and Historical Water-Level Changes in the Memphis Aquifer in the Memphis Area, Tennessee*: U.S. Geological Survey Scientific Investigations Map 3415.

KINGSBURY, J. A. AND PARKS, W. S., 1993, *Hydrogeology of the Principal Aquifers and Relation of Faults to Interaquifer Leakage in the Memphis Area, Tennessee*: U.S. Geological Survey Water-Resources Investigations Report 93-4075, 18 p.

LARSEN, D.; GENTRY, R. W.; AND SOLOMON, D. K., 2003, The geochemistry and mixing of leakage in a semi-confined aquifer at a municipal well field, Memphis, Tennessee, USA: *Applied Geochemistry*, Vol. 18, pp. 1043–1063.

LARSEN, D.; WALDRON, B.; AND SCHOEFERNACKER, S., 2022, Update map of semi-confined conditions in the Memphis aquifer, Shelby County, Tennessee. In *Proceedings of the 2022 Tennessee Water Resources Symposium*, pp. 2C-3.

MARTIN, R. V., 2008, *Shallow Faulting of the Southeast Reelfoot Rift Margin*: Unpublished Ph.D. dissertation, Department of Earth Sciences, University of Memphis, Memphis, TN, 135 p.

MARTIN, R. V. AND VAN ARSDALE, R. B., 2017, Stratigraphy and structure of the Eocene Memphis Sand above the eastern margin of the Reelfoot Rift in Tennessee, Mississippi, and Arkansas: *Geological Society of America Bulletin*, Vol. 129, No. 7–8, pp. 970–996. doi:10.1130/B31439.1

MAUPIN, M. A.; KENNY, J. F.; HUTSON, S. S.; LOVELACE, J. K.; BARBER, N. L.; AND LINSEY, K. S., 2014, *Estimated Use of Water in the United States in 2010*: U.S. Geological Survey Circular Report 1405, 56 p. doi:10.3133/cir1405

PARKS, W. S., 1990, *Hydrogeology and Preliminary Assessment of the Potential for Contamination of the Memphis Aquifer in the Memphis Area*: U.S. Geological Survey Water-Resources Investigations Report 90-4092, 39 p.

PARKS, W. S. AND CARMICHAEL, J. K., 1990a, *Altitude of the Potentiometric Surface, Fall 1985, and Historic Water Level Changes in the Memphis Aquifer in Western Tennessee*: U.S. Geological Survey Water-Resources Report 88-4180, 8 p.

PARKS, W. S. AND CARMICHAEL, J. K., 1990b, *Geology and Ground-Water Resources of the Cockfield Formation in Western Tennessee*: U.S. Geological Survey Water-Resources Investigations Report 88-4181, 17 p.

PARKS, W. S. AND CARMICHAEL, J. K., 1990c, *Geology and Ground-Water Resources of the Memphis Sand in Western Tennessee*: U.S. Geological Survey Water-Resources Investigations Report 88-4182, 30 p.

PARKS, W. S.; CARMICHAEL, J. K.; AND GRAHAM, D. D., 1985, *Preliminary Assessment of the Ground-Water Resources of Lauderdale County, Tennessee*: U.S. Geological Survey Water-Resources Investigations Report 844104, 35 p.

TOWELL, J. L., 2021, *Identification of Groundwater Recharge Pathways into the Memphis Sand Aquifer Using Geochemical*

Tracers at the Davis Wellfield, Memphis, Tennessee: Unpublished Master's Thesis, Department of Earth Sciences, University of Memphis, Memphis, TN, 88 p.

VAN ARSDALE, R.; LARSEN, D.; COUNTS, R.; WOOLERY, E.; AND EASON, A., 2017, *Quaternary Displacement Rates on the Meeman-Shelby Fault and Joiner Ridge, Second Year: Collaborative Research between the University of Memphis and USGS*: U.S. Geological Survey–National Earthquake Hazards Reduction Program Final Report of Grant G17AP00020, 23 p.

VAN ARSDALE, R. B.; ARELLANO, D.; STEVENS, K. C.; HILL, A. A.; LESTER, J. D.; PARKS, A. G.; CSONTOS, R. M.; RAPINO, M. A.;

DEEN, T. S.; WOOLERY, E. W.; AND HARRIS, J. B., 2012, Geology, Geotechnical Engineering, and Natural Hazards of Memphis, Tennessee, USA. Environmental & Engineering Geoscience, v. 18, p. 113–158. doi:10.2113/gseegeosci.18.2.113

VELASCO, M.; VAN ARSDALE, R.; WALDRON, B.; HARRIS, J.; AND COX, R., 2005, Quaternary faulting beneath Memphis, Tennessee. Seismological Research Letters, v. 76, n. 5, p. 598–614.

WILLIAMS, R.; STEPHENSON, W.; ODUM, J.; AND WORLEY, D., 2001, Seismic-reflection imaging of Tertiary faulting and related post-Eocene deformation 20 km north of Memphis, Tennessee. Engineering Geology, v. 62, p. 79–90.

Shallow Landslide Erosion Rates on Industrially Managed Timberlands: Key Factors Affecting Historical and Contemporary Rates

JASON S. WOODWARD*

Conservation Planning Department, Green Diamond Resource Co., P.O. Box 68, Korbel, CA 95550

Key Terms: *Shallow Landslide, Landslide Inventory, Shallow Landslide Erosion Rates, Mass Wasting Assessment, Timber Harvest, Timberland Management Practices, Forest Practice Rules, Habitat Conservation Plan*

ABSTRACT

Timber harvesting and related management practices associated with industrial timberlands have changed dramatically in the last two decades. Industrial timberlands are now more carefully assessed and mitigated. Recent studies of mass wasting in northern California included a review of historical aerial photographs from the early 1940s through 2016 and field measurements of nearly 3,000 shallow landslides on industrially managed timberlands. Significant improvements have been seen in management practices over time that include but are not limited to reduced harvest unit sizes, increased streamside tree retention, reduced road density, and improved road-building practices. These improvements are a result of a variety of sources such as evolving state regulations, voluntary conservation plans, and increased professional oversight. Subsequently, significant decreases in management-related erosion are being observed across the area included in this study. Observations show that improvements in management practices have positively affected regional mass wasting. In this investigation, significant changes have been noted in both causal mechanisms and landslide erosion rates. The study data shows that before the year 2000, nearly 85 percent of landslide-related erosion was determined to be the result of historical logging, either by harvesting or from roads (generally poor design and/or location). Shallow landslide erosion rates have varied over the duration of time reviewed for this study, peaking in the 1970s. Since 2000, erosion rates across the study area have decreased to 20 m^3/km^2/yr, which is a 92 percent reduction compared with the historical rate.

*Corresponding author email: jwoodward@greendiamond.com

INTRODUCTION

Timberland management can negatively impact the landscape and can lead to increased shallow landslide incidences and erosion rates. The correlation between increased landsliding and timber harvesting is well documented in the literature (Croft and Adams, 1950; Bishop and Stevens, 1964; Swanston, 1974; Sidle, 1992; and Cafferata and Spittler, 1998). These studies were based on reviews of historical management practices and methods, many of which were generally unregulated. Although forestry boards and regulations have been in existence in California since 1885, in general, a lack of enforcement prevented any meaningful environmental protections (Lundmark, 1975). Forest management has changed substantially over time, so it is appropriate to look at historical and long-term trends compared with modern-day practices and corresponding modern-era erosion rates.

Particularly in California, management practices have changed dramatically over the last four decades and probably most significantly over the last two. Regulations have changed, harvest methods have changed, and geologic hazard awareness and oversite have become commonplace. Managing industrial timberlands is no longer as simple as cutting trees for money; it has become more about responsibly managing a forest for multiple resource values.

This study was based on long-term monitoring projects associated with an aquatic habitat conservation plan (AHCP). The development of the AHCP (Green Diamond Resource Co., 2006) that is specific to this study was a collaboration between the private landowner, Green Diamond Resource Co., and federal regulatory agencies (National Marine Fisheries Service and U.S. Fish and Wildlife Service) and included a consistency determination with the California Department of Fish and Wildlife. The data was collected as part of a mass wasting assessment embedded within the AHCP. Shallow-seated landslides were the focus of data collection between 2008 and 2016, covering over 121,500 hectares (300,000 acres) in northern coastal
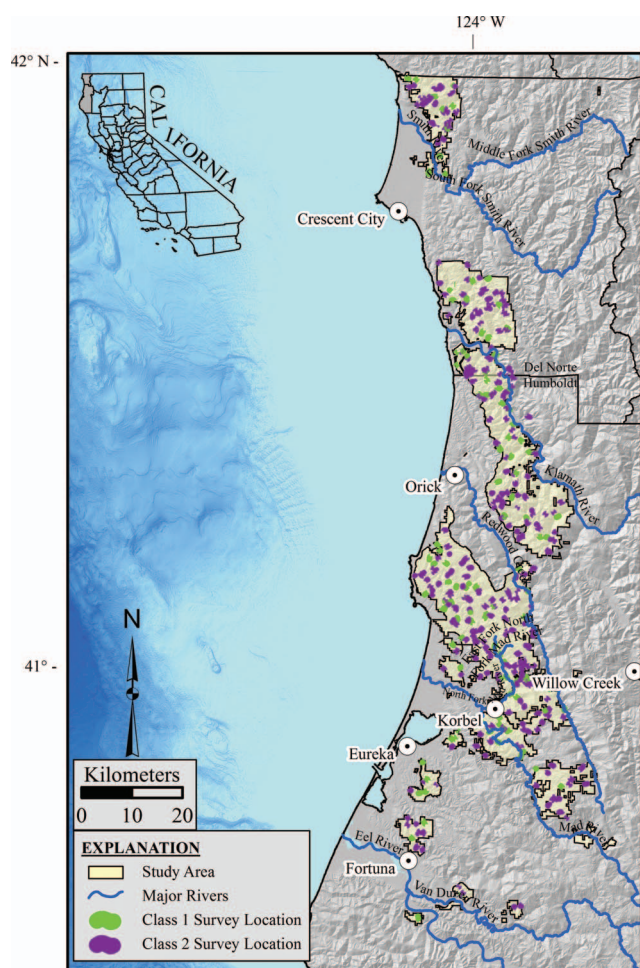
Figure 1. Study area located in Humboldt and Del Norte Counties, northern coastal California. Survey locations shown correspond with randomly selected segments of fish-bearing Class I and non–fish-bearing Class II watercourses. Note: At this scale, survey locations overlap in many instances.

Figure 2. Geologic map, modified from Jennings et al., 2010. Humboldt and Del Norte counties, California, USA. Includes National Weather Service (NWS) Cooperative Observer Program (COOP) Sites.

California. Deep-seated landslides were not evaluated for this study. Randomly selected survey locations included hillside areas adjacent to more than 6.5 percent of the perennial flowing streams within the study area.

STUDY AREA

The study area is on the west coast of the United States of America in northern coastal California. The ownership, shown in Figure 1, covers portions of Humboldt and Del Norte Counties and spans the California–Oregon border on the northern end to timberlands near the city of Rio Dell on the southern end and as far inland as the headwaters of Redwood Creek. The area includes both whole watersheds and portions of watersheds. The primary watersheds include, from north to south, Rowdy Creek, Smith River, Wilson

Creek, Klamath River, Redwood Creek, Maple Creek, Little River, Mad River, and the Eel River. Elevations range from near sea level to over 1,000 m (3,300 ft). Average annual precipitation across the property varies by as much as 100 cm (40 in.) per year. Annual precipitation data was gathered from the Western Regional Climate Center (WRCC) that originated from seven weather observation sites that are part of the National Weather Service's Cooperative Observer Program (COOP). These sites are located between Scotia and Crescent City. Although some of the data from those sites are incomplete, long-term (e.g., 15–130 years) trends are demonstrated, as shown in Table 1. The geographic distribution of the COOP sites is shown in Figure 2. Eureka and Scotia are the only two sites that are still online and presently monitoring and reporting precipitation data. With the Eureka site being more centrally located and containing the most robust data set, it was the primary source of data used in the study's detailed analysis.

Table 1. *Summary of regional climate data from the Western Regional Climate Center. Geographical distribution of the stations is shown in Figure 2.*[*]

Location (station ID)	Time Period of Record	Average Annual Water Year Precipitation (cm [in.])	Average Maximum Temperature (°C [°F])	Average Minimum Temperature (°C [°F])
Scotia, CA (048045)	Jan. 1, 1926, to July 10, 2018	121 (47)	18 (63)	8 (47)
Eureka, CA (042910)	Dec. 1, 1886, to July 27, 2018	99 (39)	15 (59)	8 (47)
Orick, CA (046498)	May 1, 1937, to Oct. 31, 2012	170 (67)	16 (61)	7 (42)
Klamath, CA (044577)	July 1, 1948, to Nov. 30, 2006	201 (79)	16 (61)	7 (45)
Crescent City, CA (042147)	Jan. 1, 1893, to July 22, 2013	181 (71)	16 (60)	7 (45)

[*]Data accessed from: https://wrcc.dri.edu/Climate/west_coop_summaries.php.

Regional and Geologic Setting

The study area is in a tectonically active area just north of the Mendocino Triple Junction (MTJ), where the North American, Gorda, and Pacific Plates collide. Seismogenic fault systems in the area are part of the MTJ and include the north end of the San Andreas Fault zone to the southwest, the Mendocino Fracture Zone to the southwest, and the southern end of the Cascadia subduction zone to the west, just off the coastline. As a result of the compressional forces exerted on the region due to the converging North American, Pacific, and Gorda Plates, there are numerous on-land upper-plate thrust faults throughout the region that are also considered potential sources for seismic shaking (Cao et al., 2003; Kelsey, 2001). They include but are not limited to Little Salmon fault, Mad River fault zone, Bald Mountain-Big Lagoon faults, and Grogan and Surpur Creek faults. The structural orientation of these upper-plate thrust faults is typically northwest-trending.

Earth materials vary throughout the study area because of the highly active tectonic regime described previously. At the southern extent of the study area, the bedrock is dominated by Miocene to Late Pleistocene deposits of the Wildcat Formation (Ogle, 1953). The Wildcat Formation is thought to be a coarsening-upward regressional sediment sequence deposited in the ancestral Eel River basin. To the north, the remainder of the property is dominated by deposits of the Coastal, Central, and Eastern Belts of the Franciscan Complex, which range in age from Pliocene to Early Jurassic (McLaughlin et al., 2000). Bedrock within the Franciscan Complex includes sedimentary, igneous, and metamorphic rock types; the most common earth materials encountered (from north to south) are sandstone and metasandstone, greenstone, mélange, and schist. A simplified illustration of the distribution of these materials, modified from Jennings et al., 2010, is shown in Figure 2. These units are somewhat specific to watersheds within the study area and are typically characterized by: (a) broken to sheared moderately indurated sandstone and metasandstone (largely in the central portion of the study area), (b) highly sheared siltstones and mudstones in an argillaceous matrix (mostly found in the central portion of the study area), (c) quartz-mica schist (primarily found in the eastern portion of the study area), and (d) moderate- to well-indurated fractured graywacke (mainly found in the northern portion of the study area). Throughout the study area, bedrock is found to be capped by Pleistocene to Holocene alluvial sediments or marine terrace deposits (Irwin, 1997).

Geomorphology varies across the study area and is characterized as more subdued in the south, becoming more rugged and incised to the north and inland. Landsliding is prevalent throughout, and types of landslides are typically associated with or attributed to the underlying bedrock. Debris slides and debris flows are the most dominant types of landslides seen across the study area. However, in the south where there are more low-gradient slopes and younger less-consolidated deposits of the Wildcat Group, an increase is seen in earth slides and translational landslides compared with other areas. Inner gorges (Kelsey, 1988) are prevalent in the central portion of the study area where examples are found of the steepest terrains that are commonplace in the Klamath River watershed.

METHODS

The study methods discussed in this section are based on or modified from previous work and literature (Wieczorek, 1984; Keaton and DeGraff,

1996; Washington Forest Practice Board, 1997; and Brardinoni et al., 2003).

Aerial Photograph Interpretation

Historical aerial photographs were assessed by using SOKKISHA MS-27 (Sokkia Co., Ltd., Atsugi, Japan) and Abrams CB-1 stereoscopes (Abrams Instrument Co., Lansing, MI). Attributes were recorded of active landslides while reviewing aerial imagery and were mapped into Esri ArcMap based Geographic Information System (GIS) using light detection and ranging (LiDAR) bare earth 1-meter digital elevation model (DEM) as a base. Post processing of the raw LiDAR data and development of the DEM was done at Green Diamond Resource Co in 2008 & 2009. Age classifications were based on Keaton and DeGraff (1996). Most of the aerial photographs in the study's collection were at a scale of 1:12,000, with some as small as 1:38,000. Stereo-paired aerial imagery years included 1942, 1948, 1954, 1958, 1962, 1966, 1969, 1975, 1978, 1984, 1988, 1997, and 2001. Orthographically rectified aerial imagery was also reviewed and included the years 2005, 2006, 2009, 2010 2012, 2014, and 2016. In total, the study covered a 74-year period. The availability of orthographically rectified imagery is changing rapidly. In the past, aerial photo flights had to be contracted and purchased. Flights were typically flown every three years or so. More recently, however, orthographically rectified imagery has been available every one to two years, either through public access sources or through contracted flights. Although the photo resolution is not as good in some cases, landslide detection using orthographically rectified photos is still adequate, in part due to the greater frequency of photo sets available.

The earliest aerial photographs reviewed were flown in 1942 and, as available, at least one set from each decade thereafter was reviewed. Aerial photo coverage across the sample area was good. However, because of the aerial extent of the project and changes in ownership over the years, not all photo sets covered the entire study area. In most cases, there was at least one photo set that covered each watershed or group of watersheds for each decade. In several cases, aerial photographs were used from two different photo years to fully review an area for a particular decade; hence, the extensive list of aerial photographs used.

Fieldwork

The data for the study was composed of information gathered as part of a mass wasting assessment. This process included surveying hillsides for shallow-seated landslides between 2008 and 2016. Surveys for landslides were completed on hillslopes adjacent to half-mile long perennial flowing Class I (fish bearing) and Class II (non-fish bearing) stream segments (Woodward et al., 2017), as well as Steep Streamside Slope (SSS) buffers that were retained for landslide prevention. Survey locations were randomly selected as described in Woodward et al. (2012) and they are shown in Figure 1. Following a review of aerial photographs, two- to three-person crews reviewed each of the survey locations. The general purpose of each of these field surveys was to confirm any landslides identified in aerial imagery and review the sample area in the field for any additional landslides that may have been missed through remote sensing. In all, hillslopes were surveyed adjacent to 298 km (185 mi) of stream segments (over six percent of the perennial stream network), as well as 37 hectares (92 acres) of SSS buffers (15 percent of the total SSS buffers). Primary data collected for each landslide included dimensions (length, width, and depth) for both the source area and the displaced landslide debris remaining on the slope, and topographic profiles, cross sections, activity levels, delivery estimates, average slope gradients, and distance to nearest watercourse. Landslide depths were estimated using information from scarp heights and field-developed topographic profiles of each landslide. Landslides were mapped in the field onto base maps generated from LiDAR with 1 meter or better resolution and later transferred into GIS. Global Positioning System (GPS) coordinates were also collected for the head and toe of each landslide. All landslides greater than 19 m^2 (200 ft^2) in aerial extent were field reviewed as part of this work.

ANALYSIS

All landslides were entered into a GIS database for analysis. Landslide volumes (Vol$_{ls}$) were calculated using the equation of half an ellipse from Cruden and Varnes (1996); see Eq. 1. Volumes were calculated for both the source area and displaced landslide debris that remained on the hillside. Cumulative or total volumes are referred to in this study in terms of the source areas. Landslide delivery is defined as the amount of material that evacuated the hillside and entered a watercourse. Delivery volumes are calculated by subtracting the volume of landslide debris remaining on the hillside from the volume of the source area:

$$\text{Vol}_{ls} = \frac{1}{6}\pi L \times W \times D, \quad (1)$$

where D = depth of landslide source area, L = length of landslide source area, and W = width of landslide source area.

Erosion rates were calculated using the sum of the total volume of mobilized landslide sediment (as measured in the field from the identified source area) of all landslides over the time span of aerial photographs reviewed (Eq. 2). Due to the extensive span of time of the aerial photo record, erosion rates have been further divided by decade and other key periods of time. For decadal rates, the ratio was extrapolated of the landslide volume of sediment (Vol_{ls}) observed from the review of aerial photographs for each decade to the total volume of sediment of all landslides in the data:

$$\text{Erosion rate} = \sum Vol_{ls}/t, \qquad (2)$$

where t = time.

Analysis of the data focused on several key aspects of management-related mass wasting. Landslide visibility and detection were assessed by comparing the ability to identify landslides using both stereo-paired aerial photographs and orthographically rectified aerial photography. Erosion rates were compared with evolving state regulations and industrial timberland management practices, by decade. Additionally, causal mechanisms were reviewed for both contemporary and historical management practices. Each of these aspects is discussed in the next section.

FINDINGS

Landslide Visibility and Detection

Comparing the review of aerial imagery with intensive field reconnaissance, an aerial photo-detection rate of 12 percent was established, which was within the range of similar studies (Robison et al., 1999; Brardinoni et al., 2003). Higher landslide detection rates may have been locally unattainable due to the lush environment of the redwood region with its more robust vegetation cover that obscures the landscape. The distribution of the landslides observed by class size compared to count and volume is shown in Figure 3a. The size of landslides that are detectable varies depending on the scale and type of imagery. Using stereo-paired aerial photographs, typically at a scale of 1:12,000, it was found that landslides were detectable down to 20 m^2 (215 ft^2) in planar view, which was smaller than similar work by Imaizumi et al. (2008), who found slides detectable to 50 m^2 (538 ft^2). However, our findings here represent the smallest landslides detected, and it was found that their legitimacy was typically questionable and required ideal photo conditions to be identified with any consistency. Although some landslides are detectable in aerial imagery at that size, many factors can come into play, such as sun angle, vegetation, and shade, all of which can obscure or hide smaller landslides, making it difficult to consider
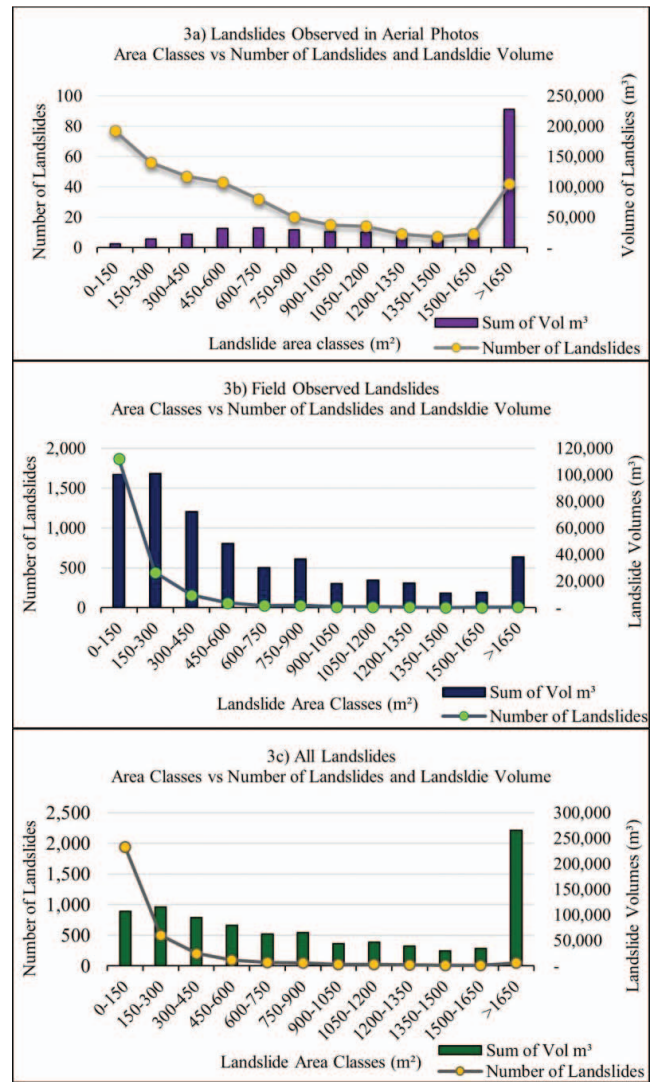
Figure 3. Landslide data. (a) Landslide area (m^2) classes versus number of slides versus volume (m^3) (includes only landslides observed in aerial photos). (b) Landslides that were observed in the field but not observed in aerial photographs. (c) All landslides; landslides less than 150 m^2 ($\leq$1,600 ft^2) in aerial extent account for only 11% of the total volume of landslides in this study yet consist of over half (65%) of the slides in the data set.

this a reliable size for detection. Considering this, an attempt was made to better define the smallest landslides that were more readily detectable. To do so, landslides that were found during the field reconnaissance but were unable to detect in aerial photographs were assessed.

Figure 3b highlights landslides that were observed on the ground but were not able to be detected with aerial photography. As landslides become larger and/or more recent, they are easier to see and then would be detectable on aerial imagery. Therefore, it is logical that most of the landslides seen on the ground

were concentrated in the smaller size classes. If the smaller class sizes are compared in Figure 3a and b, only 4 percent in the 0–150-m^2 class of the landslides could be identified, which is only one-third of the detection rate seen overall. However, in the next class size up (150–300 m^2), 11 percent of the landslides were detectable in that class, which is consistent with the overall rate of 12 percent. Frequently when reviewing watersheds, aerial photo sets were not available at more frequent time intervals than 10 years. Historical landslides, roughly 10 years old or more, were likely to have significant vegetation growth and were more difficult to discern. Although landslides were identified down to 20 m^2, landslides 150–300 m^2 in size appeared to be the smallest mappable unit that was still reliably detectable for the study area.

The smallest landslides, in the 0–150-m^2 class, dominated the population of landslides in the sample set as shown in Figure 3c, but only accounted for a small portion of the total volume. This area class represents nearly two-thirds (65 percent) of the landslides observed but accounted for only 11 percent of the total volume. Conversely, the larger landslides dominated the total volume of sediment, especially those in the greater than 1,650-m^2 size class, which accounted for 27 percent of the total volume (Figure 3c) and accounted for only 2% of the landslides observed. These data allowed a reevaluation of the minimum map unit of landslides necessary to be reviewed in future studies. Omitting these smaller landslides had a negligible impact on the overall data, including erosion rates. In doing so one could conduct a similar study with less than half the effort and without compromising the results.

Detecting landslides using aerial photography is an essential element of the work because they are used to establish decadal erosion rates. Figure 3a shows that eliminating the review of landslides less than 150 m^2 would reduce the number of landslides observed in the photo record by 21 percent (77 of the 371 landslides) yet have a negligible impact on overall cumulative volume as those landslides account for 1 percent of the total volume. That portion of the sample set is well distributed over time and therefore would not likely have a significant impact when estimating average annual rates. Ultimately, setting a minimum map unit size of 150 m^2 will allow better use of time and make work more efficient by significantly reducing the amount of fieldwork and costs involved while still producing a robust sample set to work with.

Sediment Volume and Erosion Rates

A total of 2,995 landslides were reviewed and measured in the field and of those, 371 were also identified
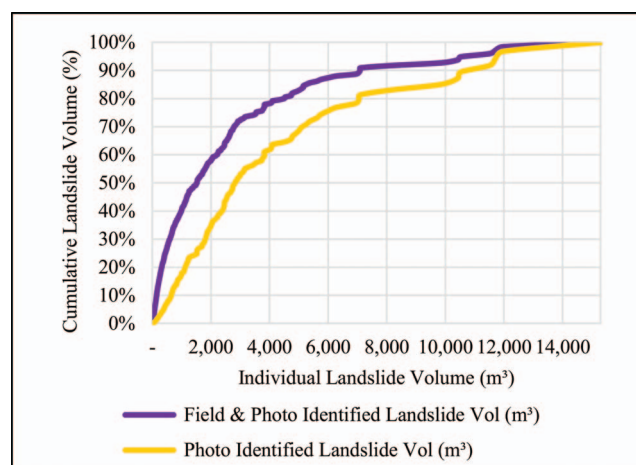

Figure 4. A comparison of cumulative volume of sediment of both field- and photo-identified landslides versus photo-only identified landslides.

during the review of historical aerial imagery. Active to dormant historic landslides were detected in each of the decades reviewed with aerial imagery. Although the landslides observed in aerial imagery accounted for only 12 percent of the number of landslides that were reviewed, they accounted for 49 percent of the total volume of sediment. As a result, those identified with historical aerial imagery provided an opportunity to look at both long-term and decadal erosion rates in coastal northern California.

In some cases, a landslide inventory and analysis may only be feasible through remote sensing. This may be due to a variety of reasons such as time constraints, access limitations, or budget issues. A comparison was made of the cumulative volume of landslide-related sediment between field and photo-identified landslides to the photo-only identified landslides in Figure 4. The variation between the two was apparent throughout most volume classes. The gap was largest with smaller landslides which are typically harder to detect in aerial photography. Brardinoni et al. (2003) saw similar variations in their survey in coastal British Columbia. These data highlight the importance of field-based data to accurately evaluate landslide volumes. Without a field-based component, volume estimates can vary by as much as 25 percent, depending on size class, because of the multitude of landslides that cannot be detected with aerial photographs. When conducting landslide inventories without the ability to conduct field reconnaissance, data should be considered to compensate for this missing component. Larger landslides are more readily detectible in aerial photographs; therefore it is important to have a wide temporal range of aerial photographs to capture the majority of those landslides which would help compensate for the data

that would be missed (the smaller size class) from field reconnaissance.

Erosion rates are typically evaluated from available aerial imagery, which is often during a brief period for the specified study area. The imagery in this study spans a much longer period (74 years) than many previous studies (e.g., Cafferata and Spittler, 1998 [38 years]; Brardinoni et al., 2003 [30 years]; and Imaizumi et al., 2008 [38 years]), and covers key periods encompassing the broad evolution of timberland management practices and regulations. The onset of aerial photography begins at a time (1942 and 1948) when the study area is largely characterized by old- and second-growth timber with virtually no forest regulations, allowing a unique opportunity to evaluate erosion rates over both historical and modern times of industrial timberland management.

Driven by evolving technology, regulations, and environmental awareness, timberland management practices have been changing for more than a century resulting in significant impacts, both positive and negative. The evolution of each of these factors has significantly influenced slope stability and erosion rates associated with shallow landsliding. The period of this study is unique as it captures old-growth and mature second-growth forests of the 1940s and early 1950s. As a result, a strong correlation can be seen between increasing erosion rates and the largely unregulated harvesting of the late 1950s through the mid-1970s that was driven by advancements in the technology of ground-based/tractor yarding. This is followed by decreasing erosion rates after the establishment of forest practice regulations and advancements in technology (mid-1970s to present). Some examples of this technology are the use of cable yarding which replaced tractors on steep slopes while the passing of the Z'berg-Nejedley Forest Practice Act of 1973 led to improved road building practices and to the establishment of stream-protection zones. Additionally, timberland management practices have seen significant changes in areas such as self-imposed Habitat Conservation Plans and yarding methods. The latest changes, over the last two to three decades, may very well be driving the continued decreasing trend in erosion rates seen in recent years. For these reasons, erosion rates were evaluated over decadal time periods, as well as determining three significant periods in the industry. These are defined as long term (1942–2016), the historical logging era (1954–1997), and the modern logging era (2000–2016). The date ranges chosen were based on a combination of observed trends combined with the dates of aerial photographs reviewed (Figure 5).

Long-term erosion rates for the study area are 145 m³/km²/yr and cover the entire period of aerial photo sets reviewed. On average it was found that
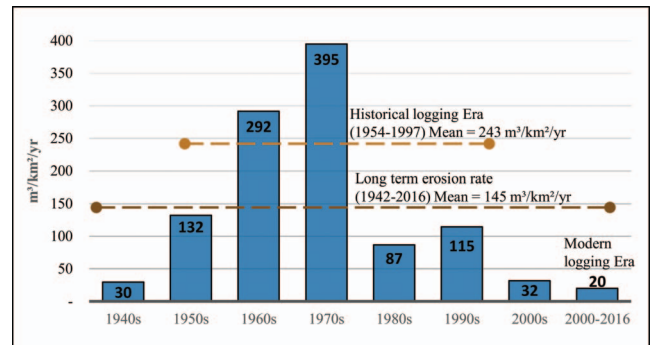

Figure 5. Erosion rates for shallow landsliding. Temporal limits for historical and modern logging eras and long-term erosion rates are based on aerial photograph dates used in the study.

delivery rates were 52 percent of the erosion rates (48 percent of landslide debris remained on the hillside). Historical logging era erosion rates were 60 percent greater at 243 m³/km²/yr and were defined as the period from the mid-1950s through the late 1990s. This period is characterized by the largely unregulated era of the 1950s and 1960s, combined with a transitioning period of the mid-1970s through the 1990s that included significant regulatory changes in the industry. As noted earlier, there was a significant rise in forest practice regulations in the mid-1970s and the regulations continued to evolve throughout the following decades. Geologic considerations quickly became part of the process beginning in the late 1970s when the California Department of Forestry (CDF), now the Department of Forestry and Fire Protection (CAL FIRE), contracted the California Division of Mines and Geology (CDMG), now the California Geologic Survey (CGS), to map the geology and landslides in several sensitive watersheds along the north coast of California (Bedrossian, 2015). The 1940s were excluded from this period as most of the study area was characterized as old-growth or mature second-growth forests at that time and closely represented the conditions of a mature or virtually unharvested forest. The modern era is characterized by key influences from the regulatory aspect as well as advances in technology that began around the year 2000. Erosion rates in the modern logging era (post-2000) have declined significantly to 20 m³/km²/yr and are down more than 90 percent compared with peak rates in the 1970s. To better understand these trends, it is essential to look at external factors that have affected erosion rates, examined in the *Discussion* section.

Causal Mechanisms

Determining causal mechanisms for historical landslides can be difficult. There are rarely firsthand

Table 2. *Causal mechanisms attributed to landslides observed in aerial photographs. Results are expressed as a percentage of erosion volumes. Note that there was no determination between legacy road-related influences and modern road-related influences. As a result, road-related causes identified in the Modern Logging Era may be a result of either or potentially both.*

Cause	Historical Logging Era, 1950–1999, N = 366 (%)	Modern Logging Era, 2000–2016, N = 12 (%)
Harvesting	44	0
Road	40	23
Natural	15	77

accounts of the landslide failure and establishing the timing of and correlation with contributing factors is difficult. Relative timing can be established using differences in vegetation type and age. However, it is often difficult for an estimate to be more accurate than a couple of decades. Aerial photographs are a key component in this analysis as they can allow the capture of anthropogenic influences before the event and can be constrained between photo sets. Table 2 shows a comparison of causal mechanisms of the historic logging era to the modern logging era using the study's data set of landslides that have been verified in aerial photographs. The table groups landslide causal mechanisms into three categories; harvesting, road, and naturally occurring (natural). Landslides characterized as related to harvesting are those having occurred in a harvested area within 20 years of operations. Road-related landslides are characterized as those that offset or truncate all or a portion of a haul road or skid trail prism or were determined to have been directly influenced by road drainage. While there are significant differences in the impacts on slope stability in legacy and contemporary roads, these have been lumped into one category for simplicity as differentiating the two was not part of the scope of this work. Naturally occurring landslides are characterized as those that have no observable connection with anthropogenic influences such as roads or harvesting as defined above. In Table 2, a reversal is seen in causal mechanisms of shallow landsliding between the historical and modern logging eras. Within the study area, it was observed that anthropogenic influences of landslides and related erosion rates were reduced to 23 percent in the modern era, whereas they accounted for 88 percent of historical erosion. To date, there has been no landslide sediment volume attributable to harvesting, as defined above, in the modern logging era. While realizing that the periods are not equal, landslides are not occurring as frequently as they used to and management-related landsliding has declined.

DISCUSSION

Key Influences Affecting Erosion Rates

This study evaluated the decadal erosion rates in comparison with the evolution of forest practice rules and private management practices, as well as regional climatic and seismic influences. In doing so, a strong correlation was found between erosion rates and evolving forest management practices and regulations. Be it intentionally or inadvertently, both management practices and regulations have been affecting the most sensitive areas on the landscape regarding slope stability and are doing so in positive ways. Seismic and climatic influences also appear to have been factors influencing rates as well. During the period of this study, there was significant seismic activity and elevated precipitation events within the region. Additionally, the role of geologic oversight and general knowledge on harvest activities has changed over time and may also be influencing landslide rates.

Changes in California State Forest Regulations

Before 1973, the timber industry was virtually unregulated with no limits to the size of harvest areas, and there were no protection measures for streams or wildlife or for unstable or potentially unstable slopes. Changes in forestry were observed after the approval of the Z'berg-Nejedley Forest Practice Act of 1973. The Act, administered by the State Board of Forestry, came with a declaration that "the forest resources and timberlands of the state furnish high-quality timber, recreational opportunities, and aesthetic enjoyment while providing watershed protection and maintaining fisheries and wildlife" (California, 1974, Chapter 8, Article 1, Section 4512 (b)). In response to the Act, the California Forest Practice Rules were revised and were regionally specific to three *Forest Districts*. These more stringent rules included limits to harvest unit sizes, riparian protection that included tree retention along streamside slopes, and new road building standards, all of which have continued to evolve and have had significant impacts on management-related mass wasting (California, 2022).

Key periods of time in changing the state of California's forest regulations that have impacted mass wasting are listed below:

- 1970s – The passing of the Z'berg Nejedley Forest Practice Act of 1973 (California, 1974) drives significant changes to the California Forest Practice Rules (CA FPR). Through a Timber Harvest Plan (THP) process, fish-bearing streams were protected by 30-meter-wide (100 ft) tree-retention buffers and

15-meter-wide (50 ft) buffers on some non–fish-bearing streams. Prior to the Act there were no protection measures for streams. Additionally, harvest blocks were limited to 32 hectares (80 acres) in size in the coast district, although there were exemptions that allowed many harvest blocks to be up to 48 hectares (120 acres).

- 1980s – The first significant revisions to stream protection areas within the CA FPRs established the Watercourse and Lake Protection Zone (WLPZ) rules in 1983 (Martin, 1989). This defined specific criteria for identifying types of watercourses and associated WLPZs in the field and expanded the widths of the zones, up to 61 meters (200 ft) on Class I, fish-bearing, streams and up to 46 meters (150 feet) on Class II, perennial-flowing non fish-bearing, streams (CDF, 1985).

- 1990s – Revisions to the California Forest Practice Rules WLPZ and roads and landings rules in 1991 resulted in restrictions on the placement of fill material on steep slopes (CDF, 1992). Additional changes to the WLPZ rules at that same time, which included elevated canopy retention, increased the overall level of protection of streamside slopes. In 1994, changes to CA FPR silviculture rules (silviculture is the theory and practice of controlling the establishment, composition, and growth of forests) and sustained-yield plans (the yield of commercial wood that an area of commercial timberland can produce continuously at a given intensity of management consistent with required environmental protection and which is professionally planned to achieve over time a balance between growth and removal) resulted in smaller harvest blocks and reduced harvest rates (CDF, 1994). Even-aged management (the goal of attaining or maintaining one age class of a stand of timber as opposed to many age classes under uneven-aged management) was now limited to a maximum of 16 hectares (40 acres). The silviculture used was mandated to maximize sustained production, which for industrial timberland owners was based on a sustained yield plan.

- 2000s – Increased protection of streamside slopes was mandated through modifications to WLPZ rules. Integration of the Threatened and Impaired (T&I) Watershed rules into the CA FPRs in 2001 increased the width of Class I watercourse zones (CDF, 2001). In 2010, the CA FPRs added the Anadromous Salmonid Protection (ASP) rule package, resulting in greater protection of streamside slopes in terms of area and elevated levels of canopy retention (CAL FIRE, 2010. Note that due to state rebranding of the Department of Forestry and Fire Protection, CDF became known as CAL FIRE in 2008.)

Many of these changes can be seen over time in aerial photographs. Figure 6 illustrates a visual evolution of portions of the study area over a 68-year period. In Figure 6a, mature second-growth and old-growth forests of the 1940s are seen. This transitions to largely unregulated industrial timberlands in the 1950s to 1970s, as seen in Figure 6b and c, at a time when there was essentially no harvest acreage limit and no watercourse protection. Figure 6d and e highlight an evolving regulated state of industrial timberlands of the 1980s and 1990s. The evolution finishes with a contemporary view of industrially managed timberlands shown on a 2016 orthophotograph with smaller harvest unit blocks of varying ages and a dendritic network of wider riparian buffers along watercourses with scattered geologic protections applied to unstable slopes and other wildlife retention areas (Figure 6f). The data shows that erosion rates drop off sharply in the 1980s, which coincides with the aftereffects of the most significant regulatory changes in the timber industry of that era (Figure 5). These changes began with the Z'berg Nejedley Forest Practice Act of 1973 (California, 1974) and appeared to be showing results by the end of the 1980s. Limiting the size of harvest blocks would have had a dramatic impact on slope stability alone. However, the new forest practice rules also provided an adjacency restriction for clear-cut blocks (the rule stipulated that historical clear-cut blocks must be at least 3 years old or more than 91 meters [300 ft] away from proposed clear-cut blocks), which spread out these harvest areas spatially and temporally rather than allowing the basin-wide clearings of the past (Figure 6b and c). In addition, fish-bearing streams were now protected with a tree retention buffer that retained root strength and allowed evapotranspiration to continue in some of the areas most sensitive to slope stability—the slopes immediately adjacent to streams. These retention areas varied over the years and by forest district but some of the early zones (mid- to late-1970s) were 15–30 meters wide (50–100 ft).

In the 1980s, new standards for planning, building, and maintaining roads were implemented, which required landowners to size culverts for specifically sized storm events, required new road drainage and design methods, and required maintenance of roads after completion of logging operations (Martin, 1989). In addition, erosion control rules were implemented that addressed watercourse crossings by tractors, brought extra precautions for winter period logging, and provided specific requirements on water-break construction. Each standard was significant as the changes simply did not exist before the 1973 Forest Practice Act and the forest practice rules that were derived from it. Driven in part by the Forest Practice Act, section 208
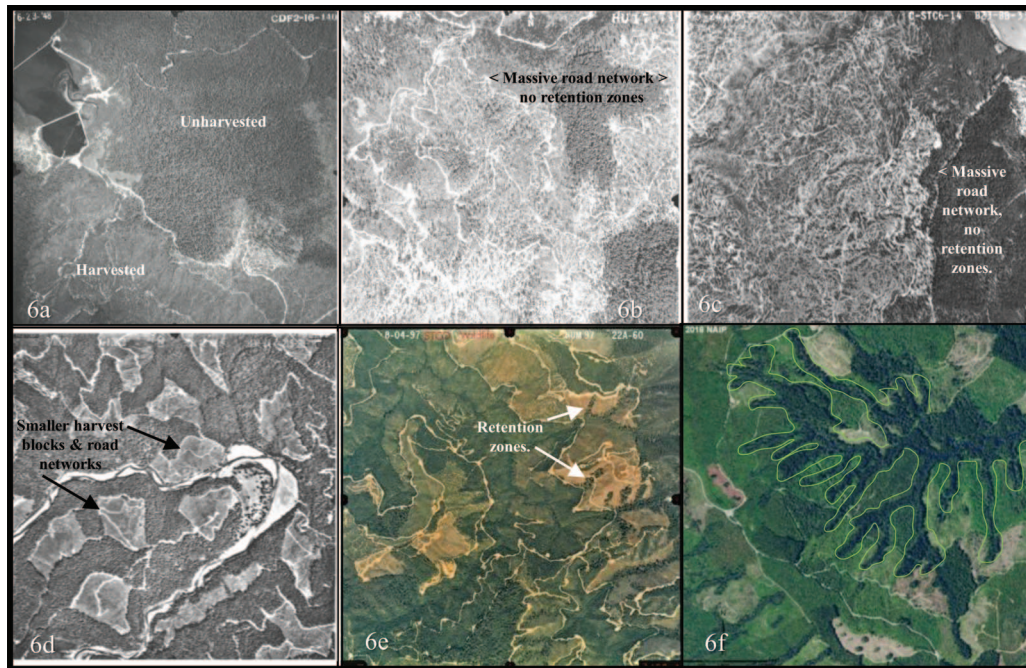
Figure 6. An evolution of timber harvesting through aerial photographs. (a) 1948 photo showing both recently harvested timberlands in the lower left corner and unharvested old-growth timberlands in the central and upper right portion of the photo. (b and c) 1958 and 1975 photos showing unregulated ground-based tractor-harvesting (white squiggly lines). At that time, there were no limits on the size of a harvest area and no riparian retention or slope stability retention standards. (d) 1984 photo showing ground-based and cable-yarding harvest that was then limited to less than 48 hectares (120 acres) (harvest blocks in this photo are less than 20 hectares [50 acres]). Road building is significantly reduced compared to previous decades/photos. Some riparian protection areas can be seen along the main river and in a smaller stream in the upper right corner of the photos. (e) 1997 photo with multiple harvest units shown in the area; at this time riparian protection areas are much more prevalent. (f) 2016 imagery of basin showing harvesting in the modern era of logging. Notice the extensive dendritic pattern of riparian protection zones (outlined in green). Note: Photos not to scale. Photo (a) original scale was 1:24,000. Photos (b), (c), (d), (e), and (f) original scale was 1:12,000. All photos were reduced by the same percentage for this figure.

of the federal Clean Water Act also played a key role in changes that came about in the latter half of the 1980s. In 1985, the chairmen of the State Water Board and Board of Forestry (BOF), the directors of the California Department of Forestry (CDF) and Department of Fish and Game (DFG), and the executive director of the California Forest Protective Association signed an agreement to assess forest practices. This agreement established a multidisciplinary team that conducted a one-year qualitative field assessment of the impacts on water quality resulting from contemporary timber operations (Martin, 1989). The team was comprised of resource specialists from DFG, CDF, the State Water Quality Control Board, and the forest products industry, and was known as the 208 Assessment Team. The team examined 100 completed state-issued Timber Harvest Plans throughout the state and the final report was completed in 1987 (Martin, 1989). Known as the 208 Report, this report spawned many changes to regulations that affected slope stability.

As a direct result of the 208 Report, new roads and landings rules and WLPZ rules were implemented in 1991 (CDF, 1992). New rules for roads and landings covered all aspects of construction with an emphasis placed on construction techniques and activities that would aid in the reduction of excessive soil displacement, the avoidance of unstable areas, an overall reduction of erosion, and the potential for sediment deposition in watercourses. That same year, the WLPZ rules were amended for the first time since 1983, also as a direct result of the 208 Report. Among those changes was the recognition of torrent salamander habitat, which increased the recognition of Class II streams and associated protection zones. In the mid-1990s, these new rules broadened the review team agency's regulatory role by adding specific protection measures and operational limitations to protect or enhance water temperature, filter strip properties, upslope stability, fish and wildlife values, and sustained-yield rules.

These continued changes have contributed to a further reduction in erosion rates over time. However, despite these changes to regulations, an increase in erosion rates was observed in the 1990s compared with the 1980s (Figure 5). This may be explained by two factors working in conjunction with each other: strong to major earthquakes followed by several years

with substantial precipitation, all of which occurred in the 1990s; and, more significantly, nearly all of this happened before the 1997 photo set. This is discussed later in the section *Seismic and Climatic Influences*.

Regulations have continued to progress in recent times and are more protective than previously. In 2001, the implementation of the T&I Watershed rules required mapping of habitat for anadromous salmonids and thereby increased the amount of Class I watercourses that were identified and then protected, resulting in additional protection of streamside slopes in those areas (CDF, 2001). More recently, in 2010, the ASP rule package was implemented as part of the updated CA FPRs at that time (CAL FIRE, 2010). This brought forth the largest and most complex changes to WLPZs to date, especially on lower-order non–fish-bearing streams. At that time, the WLPZs saw increases in overall width as well as elevated levels of canopy retention. The goal of these regulatory changes was to address wildlife habitats. However, these WLPZs were also some of the most sensitive areas potentially impacting slope stability. Additionally, significant improvements in road management were seen that led to a reduction in road-related landslides. The most recent CA FPR road rule package (CAL FIRE, 2015. Developed in 2013 and implemented in the 2015 CA FPRs) highlighted road surface drainage improvements that helped prevent road-related landslides. In the modern era, culverts are sized for 100-year storms, including sediment and debris, and ditch-relief culvert spacing, sizing, and placement are improved to avoid triggering shallow landslide and road-edge failures. Although these specifications are enforced via the CA FPRs, the specific design requirements are attributed to the work of Cafferata et al., 2004. Improved road management and increased protection of the WLPZs have certainly played a key role in the reduction of observed erosion rates. Others have noticed this correlation as well. For example, Klein and Anderson (2012) noted similar effects to these regulatory changes elsewhere in the region by assessing total sediment load.

Management Practices

Along with the continuing changes to the California Forest Practice Rules, timberland management practices have also evolved and improved over time. Such changes have been noted throughout the redwood region (Valachovic and Standiford, 2017). Among those changes are modified riparian buffers, preventative mass wasting zones, road-management plans, and low-impact harvest methods. Factors impacting erosion rates that have been associated with management practices include voluntary habitat conservation plans (HCPs), development and implementation of preventative landslide buffers, innovative riparian management zones (RMZs) that protect aquatic habitat, low-impact ground-based yarding methods, and improved road management planning. (Note: riparian management zones or RMZs are streamside habitat retention areas located along rivers and streams. These areas are analogous to the WLPZ that was established as part of the CA FPRs.) The advancement of these management practices over time has aided in the decline of erosion rates and may have had their most dramatic effect in the modern logging era when many of these factors were developed and implemented (Figure 5).

Habitat conservation plans have been under development in the study region since the early 1990s. The Simpson Timber Company established the first HCP in the industry for northern spotted owls in 1992, which increased tree retention levels in Class I and Class II streams (Simpson Timber, 1992). In 1999, the Pacific Lumber Company, now known as Humboldt Redwood Company, established an HCP for their ownership that elevated retention in RMZs when compared to the CA FPR (Humboldt Redwood Company, 2019). Their HCP also addressed slope stability issues by establishing preventative protection measures for areas defined as Mass Wasting Areas of Concern.

In 2007, an Aquatic Habitat Conservation Plan (AHCP) was implemented across the study area which included numerous measures that have influenced the observed decline in erosion rates (Green Diamond Resource Co., 2006). Among the most effective were revisions to the RMZs mentioned earlier, seen in Figure 6f. The RMZs varied in width and were characterized by two zones of canopy retention—an inner zone of 85 percent and an outer zone of 70 percent overstory canopy closure—that were applied to slopes adjacent to perennial flowing streams. At the time of implementation of this AHCP in 2007, the RMZs resulted in an increase in tree retention in these streamside areas relative to the CA FPR WLPZ. The widths of the areas were generally the same; however, the canopy retention of the WLPZ was less. By comparison, the WLPZ required the retention of only 50 percent of the overstory and understory canopy cover on perennial streams at that time. Although generally the same, in some circumstances, depending on stream classification and yarding methods, these RMZs also provided a wider buffered area in comparison to the CA FPR WLPZ.

Preventative streamside landslide protection zones were also developed as part of the Green Diamond AHCP. These areas target steep streamside slopes and enhance tree retention in areas that are typically prone to producing shallow landslides. Implemented in 2007, these buffers were revised in 2011 (Woodward et al., 2012) and 2015 (Woodward et al., 2017). A sample set

Steep Streamside Slopes
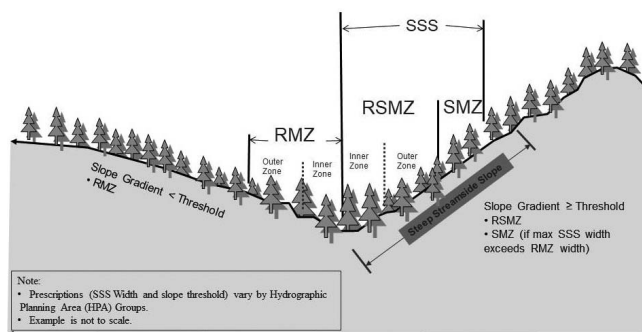### As Compared with an RMZ

Figure 7. Preventative landslide buffers known as Steep Streamside Slopes (SSS). These buffers are similar to a riparian management zone (RMZ) but have elevated tree retention standards. Each SSS is further broken into a riparian stability management zone (RSMZ) and, depending on slope steepness, a stability management zone (SMZ). The application of the SSS is determined by the steepness of slope threshold that is specific to different groups of watersheds.

of these areas is reviewed periodically for effectiveness and to date, no post-harvest management-related landslides have been detected in those areas. A schematic diagram of an SSS buffer is shown in Figure 7 along with a comparison of a standard RMZ.

Private landowners also address road building and management. Poor road building and management have been known to be significant contributors to landslide initiation and sediment input associated with timber harvesting (Swanson and Dyrness, 1975; Amaranthus et al., 1985). As part of the Green Diamond AHCP (Green Diamond Resource Co., 2006), a comprehensive road management plan was implemented, a three-part plan intended to address all roads across the property by the end of the plan design. The first part is a timber harvest plan assessment that addresses all appurtenant roads within the plan area by upgrading roads that are going to be used and decommissioning unnecessary roads. The second is a road-maintenance program that reviews all truck- and ATV-accessible roads every six years for maintenance and upkeep. The third part is a watershed-by-watershed complete assessment of all roads with an inventory of sediment sources and determination of imminent risk of failure that is to be completed by the end of the plan design.

Technology Changes

Technological advancement is another area where notable changes in the timber industry have had benefits for the environment. Cable yarding began to replace ground-based tractor yarding in the late 1970s and early 1980s, which significantly reduced road building and associated erosion. Yarding methods utilizing "shovels" were regionally introduced around 2004 and have helped reduce surface erosion associated with timber operations. Shovel yarding is a ground-based yarding method, an alternative to tractor yarding. Unlike tractor yarding, shovel yarding does not require the construction or use of skid trails to operate within a harvest block. Shovels are track-mounted machines that operate on top of slash within a harvest block and rarely expose bare mineral soil (i.e., bare dirt without the cover of organic debris). These machines "leapfrog" logs across the slope as the machine pivots and moves from one spot to the next, working toward a nearby road or landing (Figure 8c). Logs are typically fully suspended as they are moved from one location to the next. This method is utilized on slopes with inclinations up to 45 percent (approximately 24 degrees). Figure 8 illustrates a visual comparison between historical tractor-yarding methods and modern shovel-yarding methods.

Seismic and Climatic Influences

Historical records indicate that the region has shown elevated levels of seismic activity (Youd and Hoose, 1978; McPherson and Dengler, 1992; and Dengler et al., 1995) that have resulted in increased landsliding (Youd and Hoose, 1978; McPherson and Dengler, 1992). Research regarding seismically induced landsliding has shown that earthquakes can generate long-term landsliding and subsequent slide debris (Keefer, 1994). Keefer (1994) also notes that the smallest earthquake likely to generate landsliding is around a magnitude (M) of 4 and that these earthquakes generally produce only a few landslides. The effects of larger earthquakes occurring in the region, M 6 and greater, have been evaluated during the study period.

According to the United States Geological Survey (USGS) earthquake database, there have been 32 strong to major (M 6 to M 7.9) earthquakes in the region between 1940 and 2016. A graph is presented of those earthquakes and their temporal distribution by decade in Figure 9. Comparatively, the average magnitude and number of earthquakes that occurred were greatest in the 1990s. Compounding this, in April of 1992, three earthquakes, M 7.2, M 6.6, and another M 6.6, struck within 24 hours of each other near Petrolia, California, delivering modified Mercalli shaking intensities of moderate and greater across the study area. This cluster of strong to major earthquakes was preceded and followed by major earthquakes (each M 7.0) in 1991 and 1994. These earthquakes resulted in numerous landslides throughout the region (McPherson
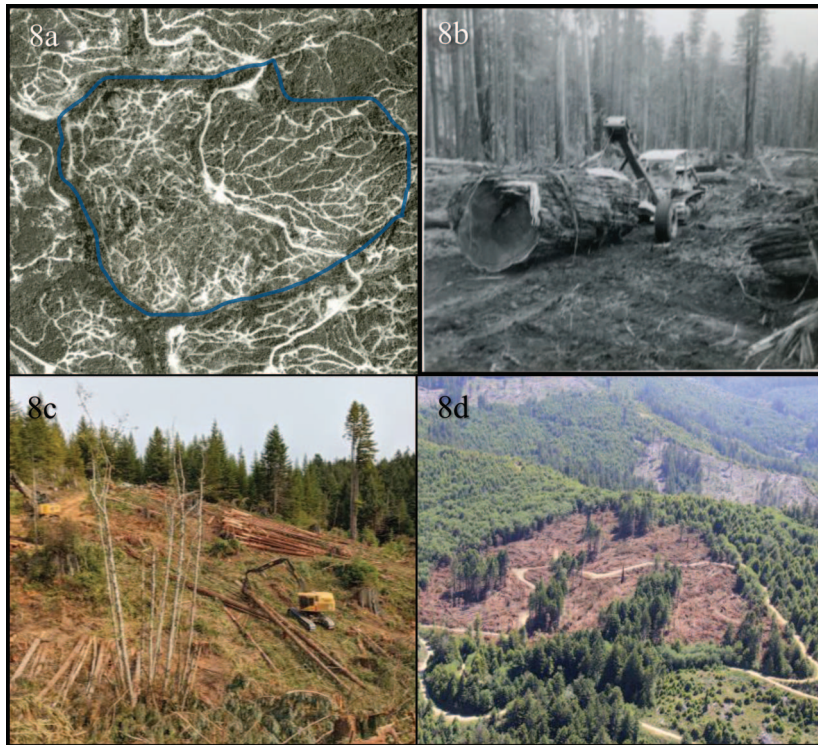
Figure 8. Tractor- and shovel-based logging. (a) Aerial imagery of tractor-based logging in the early 1980s. A dense skid road network occupies the entire harvest block exposing bare soil throughout the 54-hectare (134-acre) area. (b) Tractor-based logging in Klamath River watershed. (c) Track-mounted shovel is operating on top of slash; no skid roads are necessary for this type of machinery. (d) Harvest block utilizing shovel yarding harvest methods in an 8.9-hectare (22-acre) clear-cut. Notice there is no bare soil exposed within the block except for the logging road crossing through the block. The reddish/brown color in the harvested area is dried fir and redwood slash.

and Dengler, 1992). By comparison, according to the USGS earthquake database, the 1940s and 1950s produced a similar number of earthquakes; however, the average magnitude was less than in the 1990s. Based on these data, a higher landslide incidence would be

Figure 9. A look at seismicity over the study period. A comparison of the number of regional earthquakes ≥M 6.0 versus average magnitude, by decade. Data accessed from USGS Earthquake Hazards website: https://www.usgs.gov/programs/earthquake-hazards/earthquakes.

expected in the 1990s compared with other decades in this study and may, in part, explain the rise in erosion rates during the 1990s which are seen in Figure 5.

Research also shows that high rainfall intensity and duration can trigger an increase in landslide events (Campbell, 1975; Cannon and Ellen, 1985; and Wieczorek, 1987). To further evaluate the rise in erosion seen in the 1990s (Figure 5), average decadal rainfall and storm events were reviewed. Studies have shown that it may be necessary to review peak hourly precipitation to identify landslide triggering storm events (Cannon and Ellen, 1985, Wieczorek, 1987). Unfortunately, hourly precipitation is not available and there is no historical hourly precipitation data available for this region to accurately assess rainfall intensity. Using the limited available data from the WRCC Eureka Weather Forecast Office (WFO) COOP site, landslide-triggering storm events were assessed by summarizing elevated monthly precipitation events. These storm events, characterized as elevated monthly precipitation events that recorded 25 cm (10 in.) or more of precipitation, have a recurrence interval of one and a half years throughout this study period. Included are six noteworthy events where rainfall exceeded 35 cm (14 in.): Nov. 1973, Dec. 1983, Nov. 1984, Dec. 1996, Feb.
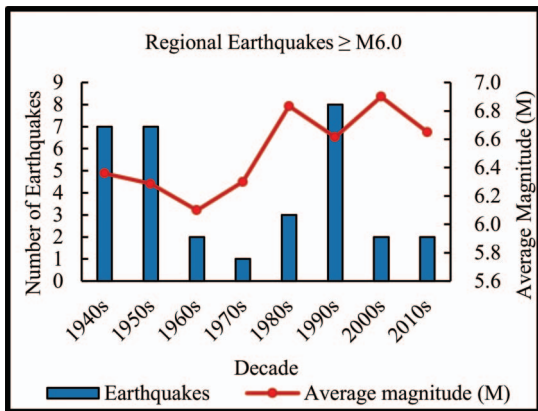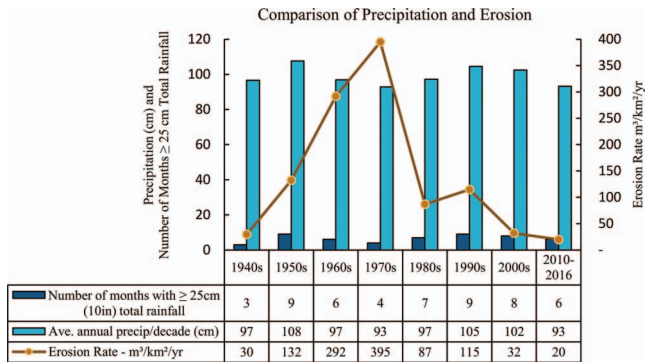
Figure 10. A comparison of average decadal precipitation, monthly storm events, and erosion. Precipitation data from Eureka weather forecast office at Woodley Island, CA. Data are shown by decade and calculated using water years (October to September), not calendar years. Each of the storm events for the 1990s follows the three strong to major earthquakes of 1992. Note: as shown in Table 1, Eureka represents the least amount of rainfall across the study area and therefore these data represent the low end of extreme climate conditions for the periods across the study area. Data accessed from https://wrcc.dri.edu/Climate/west_coop_summaries.php.

1998, and Dec. 2002; both 1996 and 2002 exceeded 53 cm (21 in.). It is assumed that peak hourly events capable of triggering landslides are most likely to occur during monthly storm events like these where precipitation is higher than normal. These data are summarized in Figure 10, which shows that high-intensity storm events and annual precipitation were elevated in the 1990s compared to most decades in this study. Only the 1950s and 2000s saw similar average annual precipitation and elevated monthly precipitation events. The average annual precipitation in the 1990s was three to five inches greater than that of the previous three decades. The assessment of storm events in this study shows that there were nine months with greater than 25 cm (10 in.) of rainfall in the 1990s with only 17 months in the previous three decades. Most of these large storm events occurred after the 1992 earthquakes, discussed earlier.

Climate records demonstrated that both annual precipitation and storm events (months with greater than 25 cm of rainfall) were greater in the 1990s than in most decades within this study; the bulk occurred during four years from 1995 to 1998. Seismic records also showed that the 1990s saw both more frequent and higher magnitude earthquakes than in any other decade in the study. With the increases in annual precipitation, storm events, and seismicity, an increase would be expected in erosion rates, which is seen in the 1990s compared with the 1980s and 2000s. Figures 9 and 10 both illustrate this correlation. After the 1990s, another sharp drop in erosion rates is noted in the modern logging era. While there was elevated precipitation in the 2000s (Figure 10), seismicity

was significantly less when compared with the 1990s (Figure 9) and, when coupled with improving management practices as discussed earlier, it may be part of the reason a drop in erosion rates was seen over this period (Figure 10).

Increased Geologic Knowledge and Oversight

Geologic input associated with timber harvesting began in the mid-1970s with the passing of the Z'berg-Nejedley Forest Practice Act of 1973. In 1978, under provisions of Section 208 of the Federal Water Pollution Control Act and with funding from the Environmental Protection Agency (EPA), the California Department of Forestry hired several geologists under *Title II Geologic Data Compilation Project* to map the geology and landslides in several sensitive watersheds in northern California (Bedrossian, 2015). The goal was to better understand non-point sources of sediment pollution from landslides within prospective THPs. It also made geologic and geomorphic mapping available to foresters for THP layout as well as for reviewing agencies. However, a review of local plans by California Division of Mines and Geology, was limited until the 1990s. With the addition of the T&I rules into the 2001 CA FPRs (CDF, 2001), the California Geologic Survey's involvement with THPs grew. At that time, CGS staffing in Humboldt and Del Norte Counties went from one employee to five employees. Licensed geologists from CGS reviewed all submitted THPs and plans with complex geologic issues and typically received on-site field evaluations known as Pre-Harvest Inspections. As a result of the increase in state review, more foresters began to seek private consulting geologists to review THPs during the layout phase. THPs with complex geologic issues typically included a geologic evaluation from a licensed geologist. Some industrial timber companies have geologists on staff to review harvest plans including Weyerhaeuser, Green Diamond Resource Co., and Humboldt and Mendocino Redwood Co., to name a few. Geologists typically review in-house LiDAR and geologic mapping, as well as published geologic mapping. At Green Diamond Resource Co., most plans receive some level of field review and 20 percent, on average, receive input in the form of a modified geologic and geomorphic map or a geologic report that is submitted with the THP. Additionally, the level of knowledge of geology, and more specifically slope stability, for a forester is likely at an all-time high. Various associations provide geologic seminars for foresters and some industrial companies provide ongoing geologic training for their forestry staff. The California Licensed Foresters Association (CLFA) has a guideline that helps foresters determine the need for input from a geologist (CLFA,

1999). This guideline, coupled with training, can help foresters during harvest plan layout to identify potential hazards and seek appropriate professional input when needed. The level of awareness regarding slope stability has increased over time and has likely contributed to a reduction in erosion rates.

CONCLUSIONS

Minimum map units can have a significant impact on the level of effort required for a mass wasting assessment. According to observations in northern California, one could increase the efficiency of future landslide inventories by setting a minimum map unit of 150 m^2 (1,615 ft^2). Using this size threshold, 89 percent of the total landslide sediment volume would be recorded from only 35 percent of the landslides surveyed, a 65 percent reduction in fieldwork. A case could also be made to reduce field efforts even further by evaluating a minimum map unit of 300 m^2 (3,230 ft^2), which would reduce the field evaluation efforts by more than 80 percent and still capture 78 percent of the total landslide sediment volume. In either case, for efficiency or economics, a minimum map unit should be carefully considered and designed to capture a balance that will accurately characterize sediment volumes with a practical number of data points.

The time span of this study provides a rare and insightful look at the effects of timberland management practices in northern California. With mostly mature forests occupying the study area during the 1940s, premanagement and post-management looks can be captured at these watersheds. As management activities increased in the decades following the 1940s, a compounding rise was clearly seen in landslide-related erosion. The Z'berg-Nejedley Forest Practice Act passed while erosion rates were at their peak and although it took several years to implement, there is no mistaking the dramatic effects it had on reducing erosion rates which were seen by the end of the 1980s. The continuing downward trend in decadal erosion rates correlates strongly with the evolution of regulations and management practices, especially those related to roads and streams.

The ability to detect and record landslides is at an all-time high thanks to the improved quality and the increased frequency of remotely sensed data and imagery. Today it is easier to track landslide-related erosion than it was previously. This study of historical landslide erosion shows that rates in the modern logging era in northern California have declined by more than 90 percent since their peak in the 1970s. Technological advances have contributed to this change and have been key in reducing ground disturbance associated with modern-day operations.

However, evolving government regulations have been the catalyst in making these changes occur beginning with the establishment of the Z'berg-Nejedley Forest Practice Act of 1973. This in turn has led to an evolution of management practices and for more landowners, that includes self-imposed regulation-like habitat-conservation plans and road-management plans, which may be the most significant factors associated with the improvements seen in the modern logging era. Observations show that conscientious landowners can and are conducting timber harvesting without significant adverse impacts on watershed resources. Once a destructive process, managing industrial timberlands has evolved to become the responsibility of managing a healthy functioning forest.

REFERENCES

Amaranthus, M. P.; Rice, R. M.; Barr, N. R.; and Ziemer, R. R., 1985, Logging and forest roads related to increased debris slides in southwestern Oregon: *Journal Forestry*, Vol. 83, No. 4, pp. 229–233.

Bedrossian, T. L., 2015, *Summary Report of OFR79-18, Title II Geologic Data Compilation Project, Geology and Landslides in Selected North Coast Quadrangles of Northern California*: California Geologic Survey, Electronic document, available at https://www.conservation.ca.gov/cgs/Documents/Publications/Open-File-Reports/OFR_79-18-Title-II-Geology-Landslides-North-Coast/Title%20II%20Maps%20Project%20Summary%202015.pdf

Bishop, D. M. and Stevens, M. E., 1964, *Landslides on Logged Areas in Southeast Alaska, Paper NOR-1: Northern Forest Exper-*

iment Station, U.S. Department of Agriculture, Juneau, AK. 30 p.

BRARDINONI, F.; SLAYMAKER, O.; AND HASSAN, M., 2003, Landslide inventory in a rugged forested watershed: A comparison between air-photo and field survey data: *Geomorphology*, Vol. 54, No. 3, pp. 179–196. DOI: 10.1016/S0169-555X (02)00355-0

CAFFERATA, P. H. AND SPITTLER, T. E., 1998, Logging impacts of the 1970's vs. the 1990's in the Caspar Creek watershed. In Ziemer, R. R. (Technical Coordinator), *Proceedings of the Conference on Coastal Watersheds: The Caspar Creek Story, May 6, 1998, Ukiah, California*. General Tech. Rep. PSW GTR-168: Pacific Southwest Research Station, Forest Service, U.S. Department of Agriculture, Albany, CA, pp. 103–115.

CAFFERATA, P. H.; SPITTLER, T. E.; WOPAT, M.; BUNDROS, G.; AND FLANAGAN, S., 2004, *Designing Watercourse Crossings for Passage of 100-Year Flood Flows, Wood, and Sediment:* California Forestry Report No. 1, California Department of Forestry and Fire Protection, Sacramento, CA., 39 p. (Revised 2017).

CALIFORNIA, 1973, *Z'berg-Nejedley Forest Practice Act of 1973*: State of California, Sacramento CA, Public Resource Code, Division 4, Part 2, Chapter 8, Articles 1-9, 18 p. Electronic document, available at https://california.public.law/codes/ca_pub_res_code_div_4_part_2_chap_8

CALIFORNIA DEPARTMENT OF FORESTRY (CDF), 1985, *California Forest Practice Rules*. Prepared for Timber Operators of California by the California Department of Forestry, Sacramento, CA., 105 p.

CALIFORNIA DEPARTMENT OF FORESTRY AND FIRE PROTECTION (CDF), 1992, *California Forest Practice Rules*: Prepared for California's Timber Operators by the California Department of Forestry and Fire Protection, Sacramento, CA., 210 p.

CALIFORNIA DEPARTMENT OF FORESTRY AND FIRE PROTECTION (CDF), 1994, *California Forest Practice Rules:* Prepared for California's Timber Operators by the California Department of Forestry and Fire Protection, Sacramento, CA., 172 p. Electronic document, available at https://bof.fire.ca.gov/regulations/bills-statutes-rules-and-annual-california-forest-practice-rules/#collapse-367f980d-a3d9-4ac2-a434-ab468387379f

CALIFORNIA DEPARTMENT OF FORESTRY AND FIRE PROTECTION (CDF), 2001, *California Forest Practice Rules*: Prepared for California Licensed Timber Operators and Registered Professional Foresters by the California Department of Forestry and Fire Protection, Sacramento, CA., 256 p. Electronic document, available at https://bof.fire.ca.gov/regulations/bills-statutes-rules-and-annual-california-forest-practice-rules/#collapse-367f980d-a3d9-4ac2-a434-ab468387379f

CALIFORNIA DEPARTMENT OF FORESTRY AND FIRE PROTECTION (CAL FIRE), 2010, *California Forest Practice Rules:* Prepared for California Licensed Timber Operators and Registered Professional Foresters by the California Department of Forestry and Fire Protection, Sacramento, CA., 338 p. Electronic document, available at https://bof.fire.ca.gov/regulations/bills-statutes-rules-and-annual-california-forest-practice-rules/#collapse-367f980d-a3d9-4ac2-a434-ab468387379f

CALIFORNIA DEPARTMENT OF FORESTRY AND FIRE PROTECTION (CAL FIRE), 2015, *California Forest Practice Rules:* Prepared for California Licensed Timber Operators and Registered Professional Foresters by the California Department of Forestry and Fire Protection, Sacramento, CA., 375 p. Electronic document, available at https://bof.fire.ca.gov/regulations/bills-statutes-rules-and-annual-california-forest-practice-rules/#collapse-367f980d-a3d9-4ac2-a434-ab468387379f

CALIFORNIA, 2022, *California Forest Practice Rules:* State of California, Sacramento Calif, Title 14 California Code of Regulations, Division 1.5, Chapter 4. Electronic record with revision history, available at https://govt.westlaw.com/calregs/Browse/Home/California/CaliforniaCodeofRegulations?guid=I2AAE54005B4D11EC976B000D3A7C4BC3&originationContext=documenttoc&transitionType=Default&contextData=(sc.Default)

CALIFORNIA LICENSED FORESTERS ASSOCIATION, 1999, *Guide to Determining the Need for Input from a Licensed Geologist during THP Preparation:* California Licensed Foresters Association, Electronic document, available at https://www.clfa.org/resources

CAMPBELL, R. H., 1975, *Soil Slips, Debris Flows, and Rainstorms in the Santa Monica Mountains and Vicinity, Southern California*: U.S. Geological Survey Professional Paper 851, 51 p.

CANNON, S. H. AND ELLEN, S., 1985, Rainfall conditions for …Abundant debris avalanches, San Francisco Bay region, California: *California Geology*, Vol. 38, No. 12, pp. 267–272.

CAO, T. C.; BRYANT, W. A.; ROWSHANDEL, B.; BRANUM, D.; AND WILLS, C. J., 2003, The revised 2002 California probabilistic seismic hazard maps, June 2003: *California Geological Survey*, Electronic document available at https://www.conservation.ca.gov/cgs/Documents/PSHA/2002_CA_Hazard_Maps.pdf

CROFT, A. R. AND ADAMS, J. A., 1950, *Landslides and Sedimentation in the North Fork of Ogden River,* May 1949: U.S. Department of Agriculture Forest Service, Forest and Range Experimental Station, Ogden, UT, Research Paper 21, 4 p.

CRUDEN, D. M. AND D. J. VARNES, 1996, Landslide types and processes. In Turner, K. A. and Schuster, R. L. (Editors), *Landslides: Investigation and Mitigation: Special Report* 247, Transportation Research Board, Washington DC, pp. 36–75.

DENGLER, L.; MOLEY, K.; MCPHERSON, R.; PASYANOS, M.; DEWEY, J.; AND MURRAY, M., 1995, The September 1, 1994, Mendocino Fault earthquake: *California Geology*, Vol. 48, pp. 43–53.

GREEN DIAMOND RESOURCE COMPANY, 2006. *Aquatic Habitat Conservation Plan and Candidate Conservation Agreement with Assurances*, Vol. 1–2, Final report: Prepared for the National Marine Fisheries Service and U.S. Fish and Wildlife Service, Green Diamond Resource Co., Seattle, WA, 568 p.

HUMBOLDT REDWOOD COMPANY, 2019. *Habitat Conservation Plan for the Properties of The Pacific Lumber Company, Scotia Pacific Holding Company, and Salmon Creek Corporation (Under the ownership and management of Humboldt Redwood Company, LLC, As of July 2008):* Humboldt Redwood Company, Scotia, CA, 160 p., Electronic document available at: https://www.hrcllc.com/sites/default/files/inline-files/HCP%20updated%20to%2003-2019.pdf

IMAIZUMI, F.; SIDLE, R. C.; AND KAMEI, R., 2008, Effects of forest harvesting on the occurrence of landslides and debris flows in steep terrain of central Japan: *Earth Surf. Processes Landforms*, Vol. 33, No. 6, pp. 827–840.

IRWIN, W. P., 1997, *Preliminary Map of Selected Post-Nevadan Geologic Features of the Klamath Mountains and Adjacent Areas, California, and Oregon*: U.S. Geological Survey, Reston, VA, *Open File Report* 97-465, doi:10.3133/ofr97465.

JENNINGS, C. W.; WITH UPDATES BY GUTIERREZ, C.; BRYANT, W.; SAUCEDO, G.; AND WILLS, C., 2010, *Geologic Map of California*: California Geological Survey, Sacramento, CA, Geologic Data Map No. 2, scale 1:750,000.

KEATON, J. R. AND DEGRAFF, J. V., 1996, Surface observation and geologic mapping. In Turner, K. A. and Schuster, R. L. (Editors), *Landslides: Investigation and Mitigation: Special Report* 247, Transportation Research Board, Washington DC, pp. 178−230.

KEEFER, D. K., 1994, The importance of earthquake-induced landslides to long-term slope erosion and slope-failure hazards in seismically active regions: *Geomorphology*, Vol. 10, No. 1–4, pp. 265–284.

KELSEY, H. M., 1988, *Formation of inner gorges: Catena*, Vol. 15, No. 5, pp. 433–458.

KELSEY, H. M., 2001, Active faulting associated with the southern Cascadia subduction zone in northern California. In Ferriz, H. and Anderson, R. (Editors), *Engineering Geology Practice in Northern California*: Division of Mines and Geology Bulletin 210, Association of Engineering Geologists Special Publication 12, Association of Engineering Geologists, Sacramento, CA, p. 259–274.

KLEIN, R. D. AND ANDERSON, J. K., 2012, Declining sediment loads from Redwood Creek and the Klamath River, north coastal California. In Standiford, R. B.; Weller, T. J.; Piirto, D. D.; AND Stuart, J. D. (Technical Coordinators), *Proceedings of Coast Redwood Forests in a Changing California: A Symposium for Scientists and Managers:* Gen. Tech. Rep. PSW-GTR-238, Pacific Southwest Research Station, Forest Service, U.S. Department of Agriculture, Albany, CA, pp. 79–88.

LUNDMARK, T., 1975, Regulation of private logging in California: *Ecology Law Quarterly*, Vol. 5, No. 1, pp 139–188.

MARTIN, E. F., 1989, *A Tale of Two Certificates the California Forest Practice Program 1976 Through 1988*: California Department of Forestry and Fire Protection, Sacramento, CA, 296 p.

MCLAUGHLIN, R. J.; ELLEN, S. D.; BLAKE, M. C., JR.; JAYKO, A. S.; IRWIN, W. P.; AALTO, K. R.; CARVER, G. A.; AND CLARKE, S. H., JR., 2000, *Geology of the Cape Mendocino, Eureka, Garberville, and Southwestern Part of the Hayfork 30 × 60 Minute Quadrangles and Adjacent Offshore Area, Northern California*: U.S. Geological Survey, Miscellaneous Field Studies Map MF-2336, various scales, 6 plates.

MCPHERSON, R. C. AND L. A. DENGLER, 1992, The Honeydew earthquake of 1991: *California Geology*, Vol. 45, No. 2, pp 31–39.

OGLE, B. A., 1953, Geology of the Eel River valley area, Humboldt County, California: *California Department of Natural Resources Division of Mines and Geology*, *Bulletin* 164, 128 p, 6 plates.

ROBISON, E. G.; MILLS, K.; PAUL, J.; DENT, L.; AND SKAUGSET, A., 1999, *Storm Impacts and Landslides of 1996: Final Report*: Forest Practices Technical Report, Vol. 4, Oregon Department of Forestry, Corvallis, OR, 145 p.

SIDLE, R., 1992, A theoretical model of the effects of timber harvesting on slope stability: *Water Resources Research*, Vol. 28, No. 7, pp. 1897–1910.

SIMPSON TIMBER CO., 1992, *Habitat Conservation Plan for the Northern Spotted Owl on the California Timberlands of Simpson Timber Company:* Prepared for U.S. Fish and Wildlife Service, 1992, Simpson Timber Co., Arcata, CA, 332 p.

SWANSON, F. J. AND DYRNESS, C. T., 1975, Impact of clearcutting and road construction on soil erosion by landslides in western Cascade Range, Oregon: *Geology*, Vol. 3, No. 7, pp. 393–396.

SWANSTON, D. N., 1974, *Slope Stability Problems Associated with Timber Harvesting in Mountainous Regions of the Western United States:* Gen. Tech. Rept. PNW-GTR-021, U.S. Department of Agriculture, Forest Service, Pacific Northwest Research Station, Portland, OR, 19 p.

VALACHOVIC, Y. AND STANDIFORD, R. B., 2017, Changes in the redwood region from 1996–2016. In Standiford, R. B. and Valachovic, Y. (Technical Coordinators), *Coast Redwood Science Symposium—2016: Past Successes and Future Direction. Proceedings of a Workshop: Gen*. Tech. Rep. PSW-GTR-258. U.S. Department of Agriculture, Forest Service, Pacific Southwest Research Station, Albany, CA, pp. 3–8.

WASHINGTON FOREST PRACTICES BOARD, 1997, *Standard Methodology for Conducting Watershed Analysis, Version 4.0, Appendix A. Mass Wasting:* Washington Department of Natural Resources, Olympia, WA., 48 p.

WIECZOREK, G. F., 1984, Preparing a detailed landslide-inventory map for hazard evaluation and reduction: *Environmental Engineering Geoscience*, Vol. 21, No. 3, pp. 337–342.

WIECZOREK, G. F., 1987, Effect of rainfall intensity and duration on debris flows in central Santa Cruz Mountains, California: *Reviews Engineering Geology*, Vol. 7, pp. 93–104.

WOODWARD, J. S.; HOUSE, M. R.; AND LAMPHEAR, D. L., 2017, Development of preventative streamside landslide buffers on managed timberlands. In Standiford, R. B. and Valachovic, Y. (Technical Coordinators), *Coast Redwood Science Symposium—2016: Past Successes and Future Direction. Proceedings of a Workshop:* Gen. Tech. Rep. PSW-GTR-258. U.S. Department of Agriculture, Forest Service, Pacific Southwest Research Station, Albany, CA, pp. 149–161.

WOODWARD, J. S.; LAMPHEAR, D. W.; AND HOUSE, M. R., 2012, Delineation of preventative landslide buffers along steep streamside slopes in northern California. In: Standiford, R. B.; Weller, T. J.; Piirto, D. D.; AND Stuart, J. D. (Technical Coordinators), *Proceedings of Coast Redwood Forests in a Changing California: A Symposium for Scientists and Managers*. Gen. Tech. Rep. PSW-GTR-238. U.S. Department of Agriculture, Forest Service, Pacific Southwest Research Station, Albany, CA, pp. 213–223.

YOUD, T. L. AND HOOSE, S. N., 1978, *Historic Ground Failures in Northern California Triggered by Earthquakes*: U.S. Geological Survey Professional Paper 993, 177 p.

Research on Side-Slope Monitoring by Integrating Terrestrial Laser Scanning and UAV-Based Photogrammetry

YUNCHUAN WANG

Faculty of Geography, Yunnan Normal University, Kunming 650500, China, and Key Laboratory of Virtual Geographic Environment, Ministry of Education, Nanjing Normal University, Nanjing 210023, China

PING DUAN*
JIA LI
ZHIKE ZHANG

Faculty of Geography, Yunnan Normal University, Kunming 650500, China

Key Terms: *Side Slope, Terrestrial Laser Scanning, Photogrammetry, Deformation Detection*

ABSTRACT

Side-slope deformation monitoring compares monitoring data from the same area over different periods and measures the deformation variables. Because of the gaps and coarseness of side-slope monitoring data, a side-slope monitoring method that integrates terrestrial laser scanning (TLS) and unmanned aerial vehicle (UAV)–based photogrammetry point clouds is proposed, aiming to solve the problem of slope monitoring in complex scenes. First, TLS and UAV-based photogrammetry point clouds are acquired. Then, the two types of point clouds are registered by an iterative closest point algorithm. Next, the data gap areas in the TLS point cloud are detected, and a gap-filling method is used to integrate the UAV-based photogrammetry point cloud with the TLS point cloud. Finally, side-slope deformation is detected based on a multiscale model-to-model cloud comparison algorithm. A side slope in Chenggong, Kunming, China, is taken as an example. The surface deformation of the side slope was monitored during January and June 2021. The experimental results show that the registration errors of the two-phase integration point cloud are 0.039 m and 0.035 m. The root mean square errors of the four ground checkpoints are 0.033 m and 0.038 m. Finally, the side slope is found to have deformed and formed a main deformation area, which shows that this side slope was in an active state.

*Corresponding author email: dpgiser@163.com

INTRODUCTION

A side slope is a critical surface with a certain inclination formed by natural gravity or human factors in rock and soil. Side slopes have a large inclination, and natural disasters such as landslides and rockslides occur when the longitudinal tensile force exceeds the shear strength (Ferrero et al., 2010; Bonneau and Hutchinson, 2019). The state of a side slope can be periodically investigated and monitored to obtain its deformation pattern, which has an important role in stability assessments and evaluation of disaster susceptibility (Passalacqua et al., 2015).

At present, there are several methods used to monitor side slopes (Scott et al., 2020). (1) In traditional side-slope monitoring methods, the side slope is measured with a total station, extensometers, inclinometers, and other traditional tools. Then, the stability of the side-slope form, area, volume, cracks and their lengths and widths, side-slope angle, surface roughness, and other parameters are assessed (Brückl et al., 2006; Dewitte et al., 2008). Side-slope and deformation information can be expressed only abstractly and inefficiently via traditional methods, which makes it difficult to meet the current demand for efficient and timely side-slope monitoring. (2) Terrestrial laser scanning (TLS) and airborne laser scanning (ALS) are also used for side-slope monitoring (Abellán et al., 2014; Rana et al., 2014; Carey et al., 2019; Pan et al., 2019; Delaney et al., 2020; Son et al., 2020; and Ali et al., 2021). Light detection and ranging (LiDAR) is used to obtain three-dimensional (3D) laser point clouds of side slopes, which are used to detect the deformation area. This method has a high accuracy, but the TLS point cloud is challenged by terrain and environmental occlusion, and it is difficult to obtain complete side-slope data. The high cost, large amount of data, and low processing efficiency are all limitations of ALS.
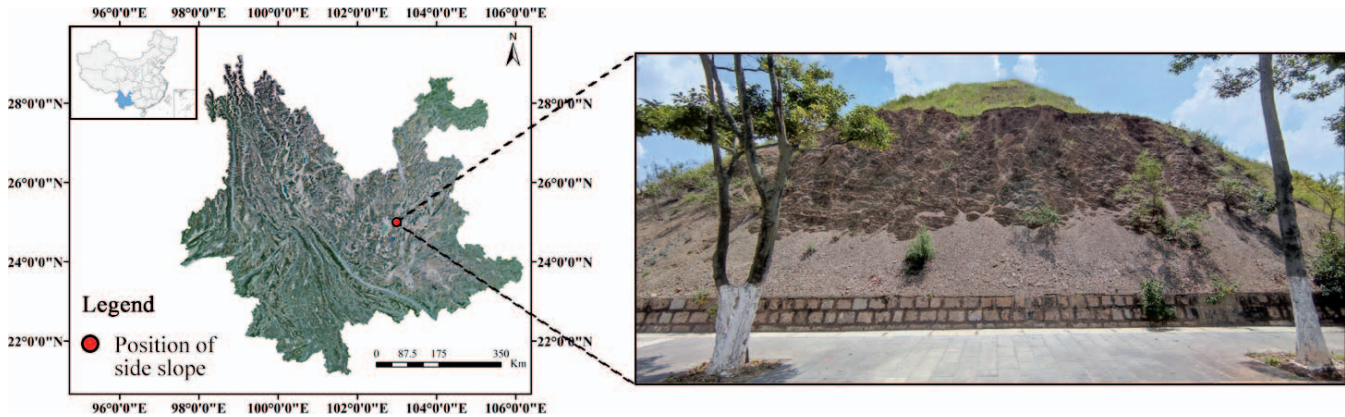
Figure 1. Study area map.

Furthermore, the monitoring accuracy is significantly affected by weather, such as clouds and rain, and it is difficult to capture small deformations in the early stages of disasters (Pitkänen et al., 2019; Kovanič et al., 2020), which makes it less applicable in the detection of small slopes and their cracks. (3) In side-slope monitoring based on high-resolution remote-sensing technology, high-resolution remote-sensing images, such as satellite images or aerial images from unmanned aerial vehicles (UAVs), can visually, graphically, and comprehensively represent the characteristics of side slopes. Rich geometric structure and texture information and multiperiod images can be obtained, and multiview and multiscale dynamic monitoring of the side-slope development process can be performed (Fourniadis et al., 2007; Lazzari and Gioia, 2017; Liu et al., 2019; Wang et al., 2019; and Rodriguez et al., 2020). However, satellite images have a long revisit period, and the images are easily affected by clouds and foggy weather. It is also difficult to meet the accuracy requirements over vertical or near-vertical slopes. The shortcomings of satellite images in timeliness, spatial resolution, and accuracy are resolved by the flexible advantages of UAVs. Previous research has shown that a dense point cloud (photogrammetry point cloud) constructed based on UAV images and photogrammetry technology provides an efficient and low-cost method for side-slope monitoring (Westoby et al., 2012; Zhang et al., 2018; and James et al., 2019).

A side slope is often characterized by steep slopes and disordered vegetation cover. When instrument portability, operational requirements, and terrain conditions of the slope are considered, UAV and TLS techniques can provide an effective solution. However, any one of these measurement techniques may have certain problems when used alone, such as data gaps caused by occlusion or insufficient resolution. In some scenarios, the gaps can be reduced to a certain extent by performing TLS at multiple locations, but this greatly increases the workload and time required, and this is inconsistent with our purpose of reducing field work. While UAV-based photogrammetry point clouds have become a low-cost alternative to TLS point clouds, the combination of TLS point clouds and photogrammetry point clouds can effectively improve the quality, accuracy, and acquisition efficiency of the data set, providing satisfactory results for capturing the complex combined details of the region of interest (Balsa-Barreiro and Fritsch, 2018; Šašak et al., 2019). Side-slope monitoring has more stringent data requirements, which puts forward new challenges to data integration methods.

Therefore, TLS devices and UAVs were used for joint air–ground monitoring in this study. The ability of TLS high-precision point clouds in the monitoring of small side-slope deformation is highlighted, and a UAV photogrammetry point cloud was used to compensate for the TLS data gap problem arising from perspective and occlusion. The integrated TLS and UAV photogrammetry point cloud method was used to achieve side-slope surface deformation monitoring on a typical side slope in Yunnan Province, China.

STUDY AREA AND DATA

Study Area

A side slope was chosen as the research object (Figure 1), located in Chenggong District, Kunming City, Yunnan Province, China. The average elevation of the area exceeds 1,900 m. The target slope was excavated during highway construction to form a relatively high and steep side slope, with prominent source and accumulation areas, and the dip angle is nearly vertical. The upper part of the source area of the side slope is mainly exposed rock, mainly composed of shale,
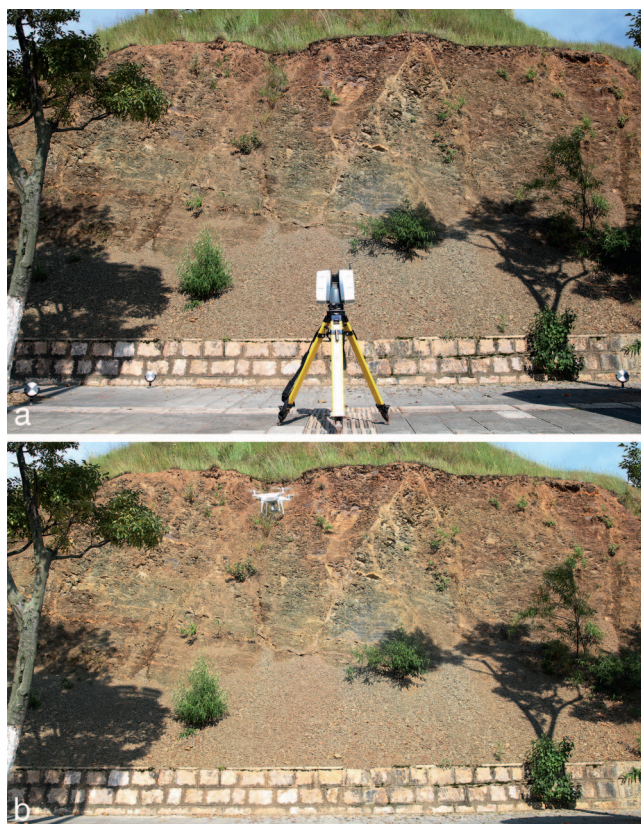
Figure 2. (a) TLS data acquisition and (b) UAV image acquisition.

with thin laminations, a rough texture, small cracks, weak weathering resistance, and the continuous flaking of fine sandy material. There are prominent block and debris deposits on the lower part of the side slope, mainly from the wall ditch at the upper part, and a few plants are distributed at the edge.

The regional climate is mainly controlled by subtropical high pressure. The annual average temperature is 14.7°Celsius, and the average precipitation is 790 mm. From May to October each year, the climate is controlled by the warm and humid air currents of the Indian Ocean and the Pacific Ocean, with abundant water vapor and high precipitation. The side slope is in a state of alternating dry and wet conditions due to the unique plateau climate, which is not conducive to the stability of the side slope and can easily induce landslide disasters.

TLS Data Acquisition

The TLS point cloud data for the side slope were obtained in January and June 2021. The surfaces of the side slope were surveyed with a Leica P40 TLS (Figure 2a), with an effective scanning distance of 270 m and an angular accuracy of 8″. Three black and white circular targets were placed on stable ground,

and real-time kinematic (RTK) technology was used to obtain the geodetic coordinates of the three target centers, which were used to convert the TLS data into the geodetic coordinate system. The global navigation satellite system (GNSS) equipment was a Leica GS15, and the measurement error of the target was within ±0.03 m.

UAV Image Acquisition

UAV images of the study area were collected in January and June 2021. A DJI Phantom 4 Pro was used for this research (Figure 2b). The trajectory of the UAV flight was set in advance; the image overlap was 85 percent, the side overlap reached 75 percent, and a relative flight height of 60 m from the ground was maintained at the bottom of this side slope. The acquisition of image data in the study area was achieved by autonomous UAV flight, the horizontal route with the best versatility was used, and the UAV image was acquired from the vertical perspective to acquire image data in a short time and reduce data redundancy. The same flight route and related parameters were used in the two aerial flight operations. In total, 153 UAV images were acquired the first time and 154 UAV images were acquired the second time, with an average ground resolution of 0.016 m/pixel.

Five ground control points (GCPs) were evenly distributed around the side slope. An L-shaped sign was drawn with red paint on the stable area as the sign for the GCPs, with dimensions of approximately 0.8 m × 0.8 m. Ten locations were randomly selected as checkpoints (CPs), and the locations of the CPs included the ground and some side-slope positions accessible to the operators. Measurements of the GCPs and CPs were performed using a GNSS-RTK, and the measurement error was within ±0.03 m.

Side-Slope Point Cloud Generation

A Leica cyclone was used for TLS point cloud processing. First, the TLS point cloud was georeferenced. Three target points in the point cloud were assigned geographic coordinates as measured by GNSS-RTK and projected. The final TLS point cloud was converted to the World Geodetic System 1984 (WGS84) Universal Transverse Mercator (UTM) Zone 48N (EPSG:32648) projection coordinate system. The average registration error of the three targets in the January TLS point cloud was 0.012 m, and that in June was 0.011 m. Then, the point cloud was imported into CloudCompare software, and the vegetation and noise were removed with the moving least squares smoothing and statistical outlier removal algorithms.
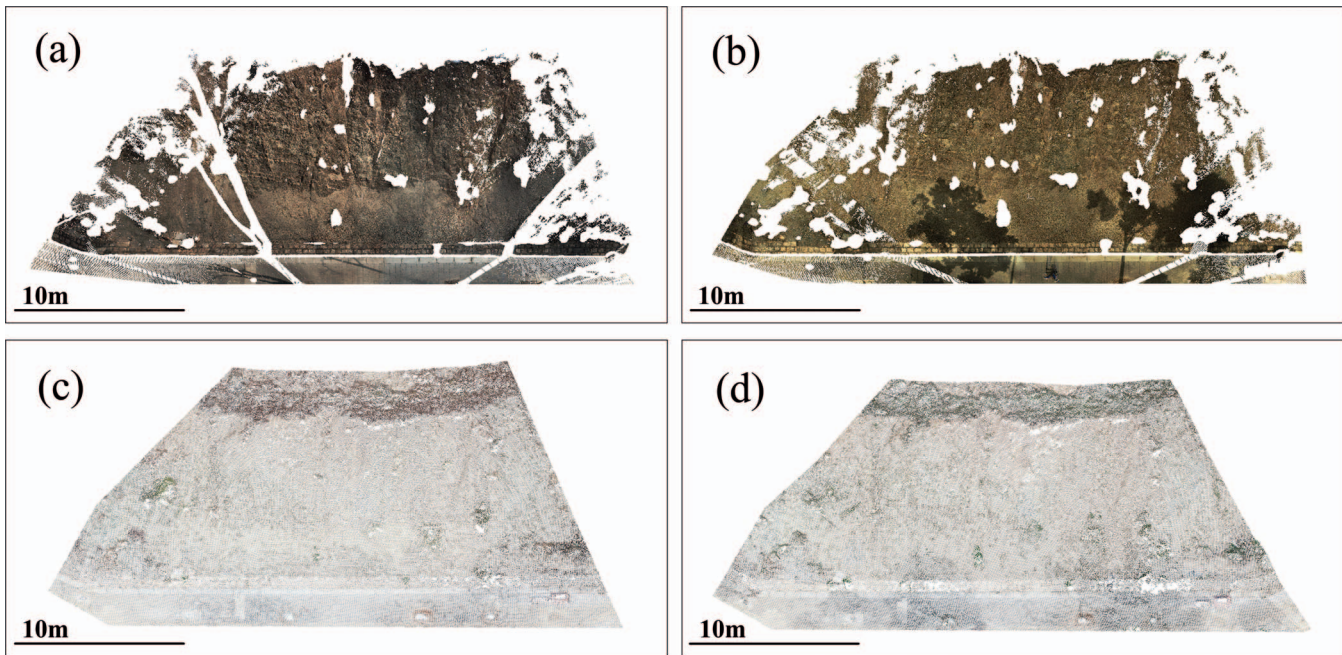
Figure 3. (a) TLS point cloud in January 2021, (b) TLS point cloud in June 2021, (c) UAV-based photogrammetry point cloud in January 2021, and (d) UAV-based photogrammetry point cloud in June 2021.

The final TLS point clouds in January and June are shown in Figure 3a and Figure 3b, respectively, with a spatial resolution of 0.015 m. The TLS point clouds contain many data gap areas. The main reason is that the vegetation on the ground and side slopes caused obstruction, and point cloud information in the obscured area could not be obtained. Therefore, the TLS point clouds with gaps lack spatial continuity and cannot be used to monitor side-slope surface deformation.

The UAV images were processed using Pix4D Mapper software. First, the key points in UAV images were detected and matched, followed by automatic bundle adjustment. In the two periods of photogrammetry processing, five identical and uniformly distributed GCPs were involved in this step. Sparse 3D point clouds of the side slope with WGS84 UTM 48N (EPSG:32648) projection coordinates were generated. The aerial triangulation results show that the average root mean square error (RMSE) was 0.021 m, which meets the accuracy requirements. Finally, dense point clouds were constructed by the multiview stereo (MVS) technique.

The trees on the ground and top of the side slope were removed by the cloth simulation filter (CSF) algorithm in CloudCompare software (Zhang et al., 2016), and the final photogrammetry point clouds in January and June are shown in Figure 3c and Figure 3d, respectively. The average point cloud densities in January and June were 589 points/m^2 and 575 points/m^2, respec-

tively. More importantly, the photogrammetry point cloud was very complete and uniform.

SIDE-SLOPE MONITORING METHOD INTEGRATING TLS AND UAV PHOTOGRAMMETRY POINT CLOUDS

Method

The side-slope monitoring method integrating TLS and UAV photogrammetry point clouds is shown in Figure 4. The method consists of three main steps: point cloud registration, point cloud integration, and side-slope deformation monitoring. The TLS point cloud and UAV photogrammetry point cloud for the same period were registered to the same reference coordinates in the first step. The data gap areas in the TLS point cloud were filled by the photogrammetry point cloud during point cloud integration to produce a complete data set. The TLS–UAV photogrammetry point clouds in the two periods were analyzed via time series, thereby monitoring the deformation of the side slope over the relevant time range. The following subsections introduce the point cloud registration, point cloud integration, and side-slope deformation monitoring methods.

Point Cloud Registration

TLS point clouds and UAV photogrammetry point clouds must be georeferenced before integration. The
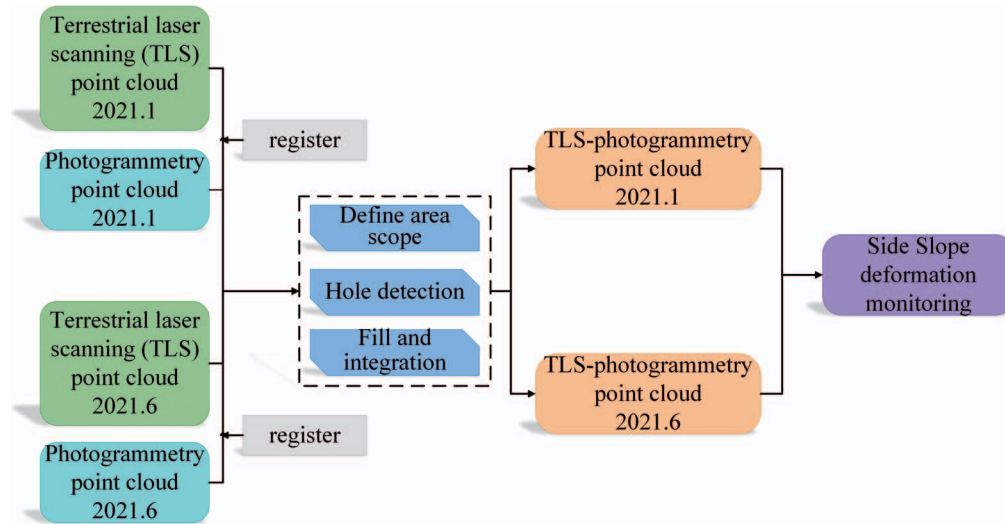
Figure 4. Schematic workflow.

iterative closest point (ICP) algorithm (Besl and McKay, 1992) was used to accurately register the point clouds. Since the number of UAV photogrammetry point cloud points was substantially less than that of the TLS point cloud, to avoid the phenomenon of redundant points not finding corresponding points during the search-for paired points, the UAV photogrammetry point cloud and TLS point cloud data sets were used as the reference data and the target data, respectively. The 3D distance was minimized between the photogrammetry and TLS point clouds by finding the best translation and rotation parameters, as shown in Eq. 1,

$$E\left(R, T\right) = \frac{1}{n} \sum_{i=1}^{n} \| q_i - (R \cdot p_i + T) \|^2 \qquad (1)$$

where q and p represent the UAV photogrammetry point cloud and TLS point cloud, respectively; n is the number of point clouds; R and T are the rotation matrix and translation matrix, respectively; and E is the distance error under the current registration parameters.

Point Cloud Integration

The final TLS point cloud and UAV photogrammetry point cloud data sets (Figure 3) show the difference in detail on the side-slope surface. The TLS point cloud is highly detailed and has a high spatial density, with a density of approximately 8000 points/m^2, so that the surface texture of the side slope can be observed. Uniform and large spatial separation is characteristic of UAV photogrammetry point clouds, with a point cloud density of approximately 600 points/m^2.

Therefore, the surface topography and slight undulations can be only approximately represented by the photogrammetry point cloud. Here, the point clouds obtained based on TLS and UAV are compared, as shown in Table 1. Among them, TLS point clouds have advantages in point cloud density and accuracy, while UAV photogrammetry point clouds have advantages in point cloud integrity and acquisition efficiency. Therefore, the shortcomings of a single method can be remedied by point cloud integration.

If the two kinds of point clouds are integrated directly, then the accuracy of the TLS point cloud is reduced, producing a final point cloud that contains substantial ambiguity. Therefore, only the gaps in the TLS point cloud were filled with the UAV photogrammetry point cloud. MATLAB software was used for point cloud integration, and the computer processer was an AMD Ryzen R5-5600X CPU with 16 GB RAM. The algorithm process is as follows.

- Step 1: Definition of the scope of the area. The TLS point cloud and UAV photogrammetry point cloud are projected onto the x-y axis plane. The side-slope distribution range in the TLS point cloud is used as

Table 1. *Comparison of TLS and UAV-based photogrammetry point clouds.*

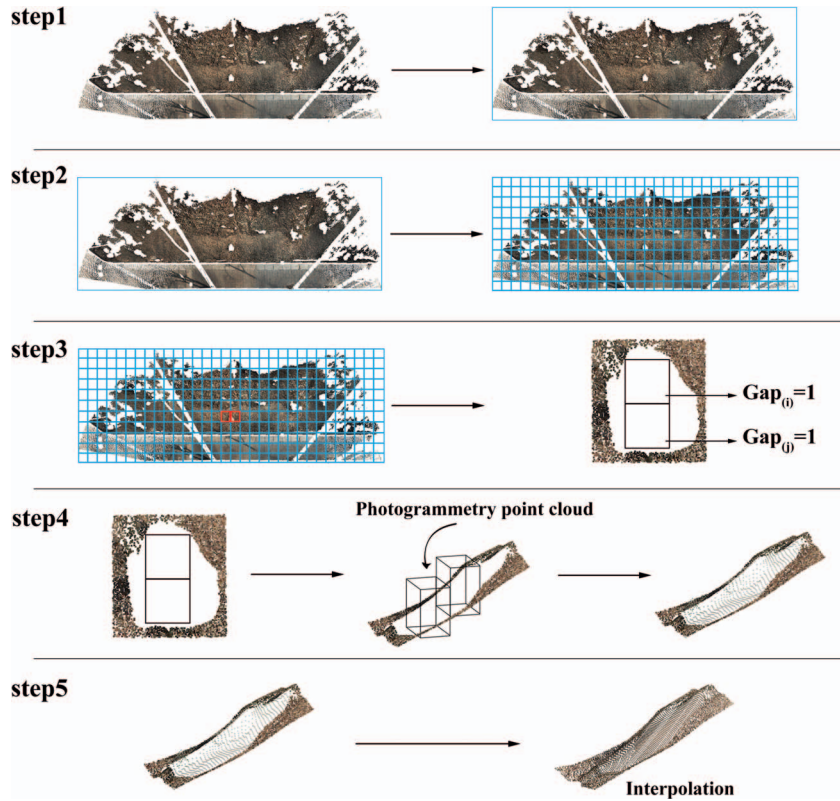|	TLS Point Cloud	UAV-Based Photogrammetry Point Cloud
Density	High	Low
Precision	High	Low
Integrity	Low	High
Acquisition efficiency	Low	High

Figure 5. Point cloud integration schematic: (step 1) defining the scope of the area; (step 2) creating a detection grid; (step 3) gap detection; (step 4) point cloud filling; (step 5) photogrammetry point cloud cryptographic interpolation.

a reference to calculate the minimum bounding rectangle of the side slope. See "step 1" in Figure 5.

- Step 2: Detection grid creation. Taking the minimum bounding rectangle as the boundary range, the actual size of the side slope and the results of multiple experiments are considered. Finally, the minimum bounding rectangle of the side slope is divided by a 2.5 cm × 2.5 cm regular grid, which is used as an area threshold to detect the gap area in the TLS point cloud. See "step 2" in Figure 5.
- Step 3: Gap detection. The grids are traversed to obtain the gap grid based on Eq. 2, which represents the gap area in the TLS point cloud. See "step 3" in Figure 5.

$$Gap_{(i)} = \begin{cases} 0, & n_i \geq 1 \\ 1, & n_i = 0 \end{cases} \quad (2)$$

where i is the current grid, and n is the number of TLS point clouds in the grid. When Gap is 1, the current grid is a gap grid.

- Step 4: Point cloud filling. The UAV photogrammetry point cloud corresponding to the gap areas is extracted and used to fill the gaps by traversing all the gap grids and integrating it with the TLS point cloud. See "step 4" in Figure 5.

- Step 5: Photogrammetry point cloud cryptographic interpolation. To ensure that the spatial density of the integrated point clouds is uniform, the UAV photogrammetry point cloud in the filled areas is interpolated by the natural neighbor interpolation method (Sibson, 1981; Watson, 1994). The resulting point cloud density is close to that of the TLS point cloud. See "step 5" in Figure 5.

Side-Slope Deformation Monitoring

A multiscale model-to-model cloud comparison (M3C2) was used to monitor the side-slope deformation (Lague et al., 2013). The basic steps to monitor the side-slope surface deformation process in this study are as follows (Figure 6):

- Point cloud normal vector calculation. The two final TLS–UAV photogrammetry point clouds in January and June are defined as Clouds 1 and 2 (same below), and the entire original point clouds are fully involved in the computation. We define the radius as $D/2$ (The diameter D is used to limit the search range of the normal vector calculation, which is set to 0.25 m in this paper) for each point in Cloud 1. The points within $D/2$ of the current point are fitted
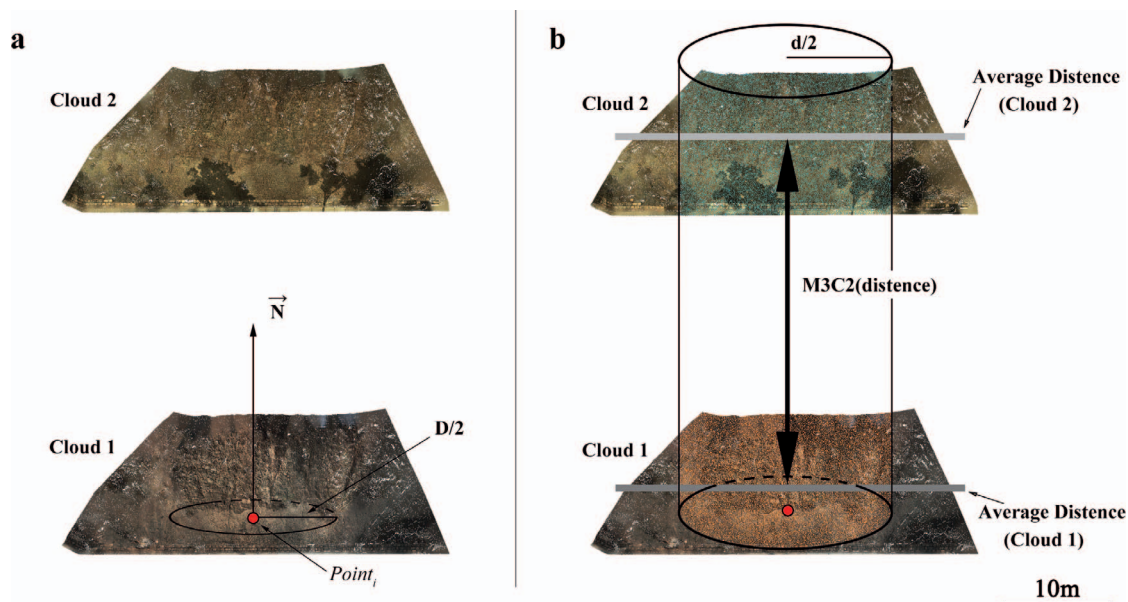
Figure 6. M3C2 distance calculation process: (a) point cloud normal vector calculation, where Clouds 1 and 2 are the TLS–UAV photogrammetry point clouds in January and June, respectively, and (b) M3C2 distance calculation.

to the local surface, and the normal is calculated as the normal vector of the point, as shown in Figure 6a.

- Point cloud distance calculation. We define a search cylinder with radius $d/2$ (The d is used to limit the search range of the point cloud calculation distance, which is set to 0.15 m in this paper) where the axis passes through each point and points in the direction of its normal vector. Then, the cylinder truncates subsets of the Clouds 1 and 2 point clouds (i.e., the point clouds located inside the cylinder). These two subsets of Clouds 1 and 2 are projected onto the axis of the cylinder, and their average positions are calculated. The distance difference between the average position of the two subsets along the normal direction represents the M3C2 distance of the point, as shown in Figure 6b.
- Side-slope deformation area characterization. All point clouds are executed with the above steps, and the M3C2 change for the entire point cloud represents the deformation result for the side slope. Here, positive values represent positive deformation (deposition), and negative values represent negative deformation (erosion).

RESULTS

Point Cloud Integration Results

Figure 7 shows the final TLS–UAV photogrammetry integrated point clouds. The problem of single data defects (Figure 3) is well solved by the integration of the TLS and UAV photogrammetry point clouds. Figure 7 shows a comparison of local slope details among the TLS point cloud, the UAV photogrammetry point cloud, and the integrated point cloud, which highlights the advantages of the proposed method, as well as the shortcomings of a single point cloud. The TLS point cloud has voids and uneven point cloud density, and the UAV photogrammetry point cloud is slightly sparse. The real surface morphology of the slope is reproduced by the TLS–UAV photogrammetry integrated point cloud.

Point Cloud Accuracy Analysis

Point Cloud Registration Error—The RMSE was used to evaluate the registration error of TLS and UAV photogrammetry point clouds; its formula is as follows:

$$RMSE = \sqrt{\frac{1}{n}\left[\sum_{i=1}^{n}\left(x_i - x_i^{co}\right)^2 + \sum_{i=1}^{n}\left(y_i - y_i^{co}\right)^2 + \sum_{i=1}^{n}\left(z_i - z_i^{co}\right)^2\right]}$$

(3)

where x, y, and z are the coordinate points in the UAV photogrammetry point cloud; x^{co}, y^{co}, and z^{co} are the corresponding points of the photogrammetry in the TLS point cloud, respectively; and n is the number of point clouds.
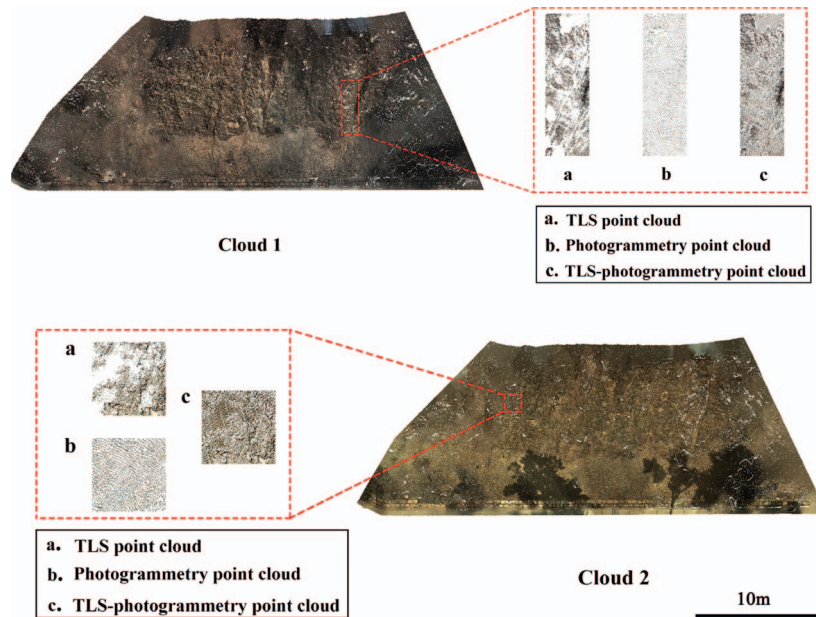
Figure 7. Final TLS–UAV integrated photogrammetry point clouds.

The final point cloud registration error is shown in Table 2. The registration RMSE between the TLS and UAV photogrammetry point clouds was 0.039 m in January and 0.036 m in June, indicating a low registration error. In the registration process of the ICP algorithm, the UAV photogrammetry point cloud looks for the closest point in the TLS point cloud as its corresponding point and shortens the spatial distance between them. However, there are still some differences between the original UAV photogrammetry point cloud and the TLS point cloud in sensor resolution and coverage. Therefore, the best corresponding points cannot be found at some points, affecting the entire registration and accuracy evaluation process and resulting in the final point cloud registration error being maintained at approximately 0.03–0.04 m.

Point Cloud Absolute Accuracy—The absolute accuracy of the final point clouds was verified by a direct cloud-to-cloud comparison with the closest point distance (C2C) between 10 independent CPs and the TLS–UAV photogrammetry point clouds, and the results are shown in Tables 3 and 4. Four of the 10 CPs are on stable ground, and six are on the slope. The final RMSEs of the CP C2C distances for the two periods were 0.051 m and 0.093 m. The CP distribution is shown in Figure 8.

Four ground CPs were found to maintain nearly the same range of C2C distances in the two periods of accuracy validation. The maximum increase was 0.013 m, which is less than the acquisition error of the GNSS measurement equipment and can therefore be considered a systematic error introduced by the measurement. Four ground CPs were used as the accuracy index. Because of the instability of the slope, the measured coordinates of the CPs on the slope may be different from their actual positions, and the deformation of the slope itself leads to a change in the positions of the CPs. The separately calculated C2C RMSEs of the four ground CPs in the two periods were 0.033 m and 0.038 m. Moreover, the RMSE of all CPs of the first-phase point cloud was 0.051 m (considering that no deformation occurred at this time), which confirms that the absolute accuracy of the final point cloud was relatively high.

Except for point 10, the C2C distances of the CPs on the side slope all increased significantly, exceeding the scope of system error. Point 10 was located in the middle edge of the side slope among the six side-slope CPs, and the others were located in the lower part of the side slope. Therefore, it can be considered that the second-phase point cloud exhibited prominent signs of deformation compared with the first-phase point cloud.

Then, the absolute precision of the TLS point clouds and UAV photogrammetry point clouds in the two periods before the integration were calculated and compared with the integrated point cloud, and the results are shown in Table 4. From the results, the accuracy of TLS point clouds and UAV photogrammetry point

Table 2. *Registration accuracy.*

	Cloud 1	Cloud 2
RMSE (m)	0.039	0.035

Table 3. *Absolute accuracy of integrated point cloud.*[1]

	Cloud 1				Cloud 2			
Number	Δx (m)	Δy (m)	Δz (m)	D (m)	Δx (m)	Δy (m)	Δz (m)	D (m)
01	0.020	−0.022	0.037	0.048	−0.023	0.004	0.050	0.055
02	−0.017	−0.002	0.022	0.028	−0.054	−0.018	0.136	0.147
03	0.008	0.006	−0.016	0.019	−0.019	−0.005	0.057	0.060
04	−0.001	0.003	0.021	0.021	−0.029	−0.003	0.100	0.104
05	−0.063	0.030	0.089	0.113	−0.084	0.009	0.139	0.162
06	0.017	0.010	0.034	0.040	−0.046	−0.007	0.080	0.093
07	−0.010	0.008	0.053	0.054	−0.006	−0.001	0.066	0.067
08	−0.002	0.005	0.051	0.051	−0.005	−0.001	0.054	0.054
09	0.004	0.004	0.063	0.063	0.018	−0.012	0.073	0.076
10	0.021	0.004	−0.006	0.023	0.000	−0.005	0.003	0.006

[1]D represents the C2C distance of CPs and integrated point clouds, and Δx, Δy, and Δz represent the three components of the C2C distance (m).

Table 4. *Accuracy of point cloud data sets.*

	TLS				UAV				TLS-UAV Photogrammetry	
Number	D_1 (m)	$RMSE_1$ (m)	D_2 (m)	$RMSE_2$ (m)	D_1 (m)	$RMSE_1$ (m)	D_2 (m)	$RMSE_2$ (m)	$RMSE_1$ (m)	$RMSE_2$ (m)
01	0.048	0.508	0.151	0.583	0.076	0.063	0.055	0.098	0.051	0.093
02	0.028		0.131		0.047		0.147			
03	0.019		0.066		0.042		0.060			
04	0.021		0.090		0.027		0.110			
05	0.125		0.177		0.113		0.162			
06	0.074		0.160		0.040		0.093			
07	0.083		0.044		0.054		0.082			
08	0.051		0.043		0.068		0.082			
09	1.597		1.813		0.074		0.076			
10	0.023		0.010		0.040		0.033			

clouds is low before integration. Most of these CPs have the same distance in the TLS point cloud as after integration; however, there are individual points, such as point 9, located in the missing area of the TLS point cloud, that make the absolute accuracy of this kind of point poor. In the UAV photogrammetry point cloud, this situation does not exist because there are no gaps, but because its overall accuracy is relatively low, the accuracy of the CPs is slightly lower than that of the integrated point cloud. This result shows the advantage of the integration method in terms of precision.

While maintaining the high absolute precision of the TLS point cloud, the integrated UAV photogrammetry point cloud makes up for the resulting precision loss by filling in the missing areas so that the final integrated point cloud has higher precision than the point cloud before integration.

Deformation Monitoring

To quantify the surface deformation process during this period, the M3C2 algorithm was used to moni-
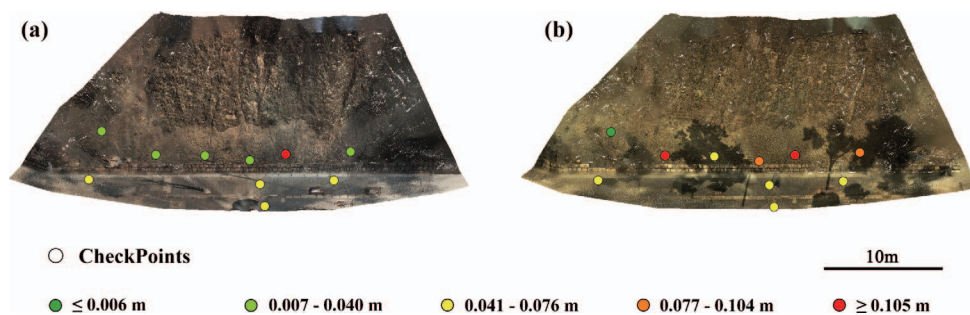

Figure 8. Checkpoint distribution and C2C distance: (a) Cloud 1 and (b) Cloud 2.
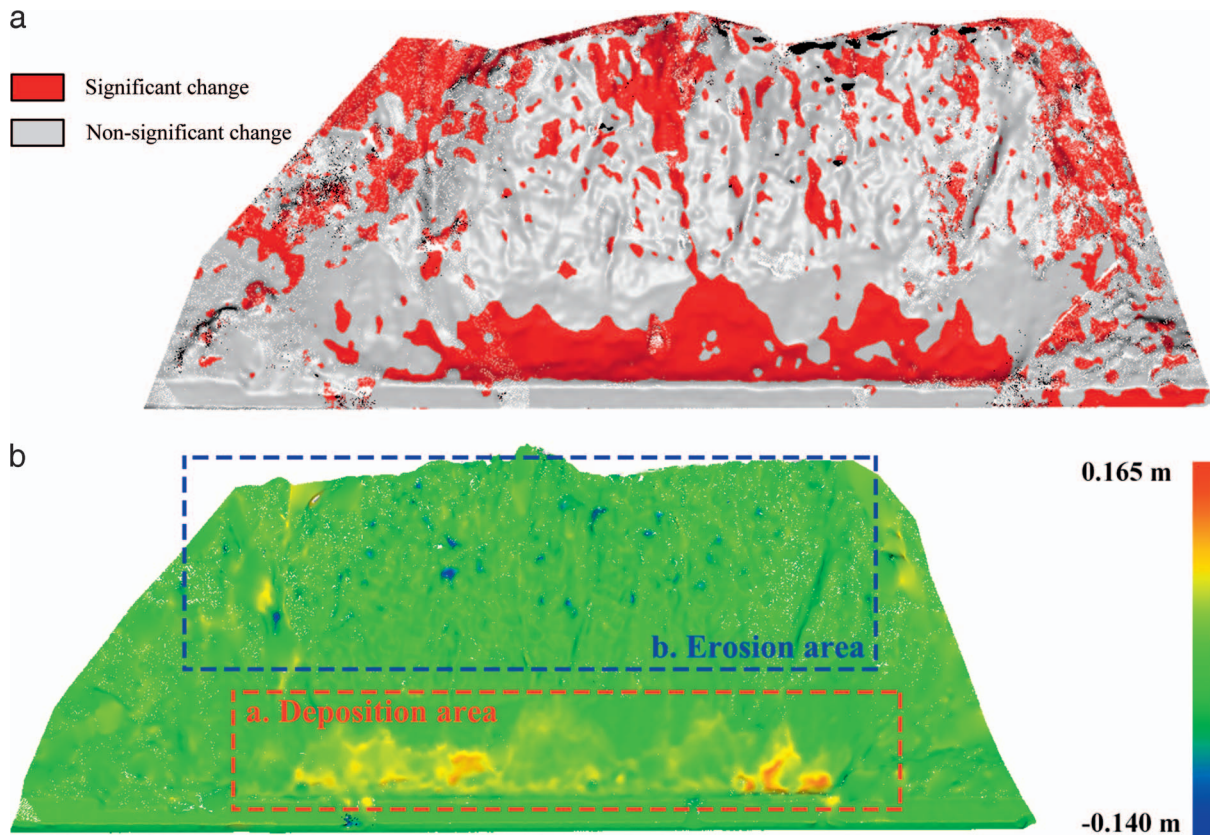
Figure 9. Deformation results: (a) Significant change. (b) M3C2 results for Clouds 1 and 2.

tor the deformation of the TLS–UAV photogrammetry point clouds between the two periods. The M3C2 algorithm calculates the distance between point clouds along the direction normal to the surface, estimating a spatially variable uncertainty for each point cloud in accordance with terrain roughness and coregistration error, which provides more accurate results (DiFrancesco et al., 2020; Hout et al., 2020). The difference models for the main deformation area and significant change area are shown in Figure 9a and Figure 9b. The significant change area (<-0.05 m and >0.05 m) is mainly the lower debris accumulation area of the side slope and upper exposed rock area, i.e., the yellow, red, and blue areas in Figure 9b. Based on this, the area was divided into an erosional area represented by the blue box and a depositional area represented by the red box in Figure 9b. The deformation results of the upper part of the side slope showed negative values (blue part in Figure 9b), indicating that the surface rock weathered and spalled over nearly half a year. Furthermore, multiple small-scale cracks were observed to have developed (e.g., Figure 10). In the differential model, most of the rock spalling area exists near the surface cracks, which are more prominent in certain rock blocks.

The positive deformation in the differential model (red part in Figure 9b) corresponds to the debris accumulation area at the foot of the side slope. The results showed continuous distribution characteristics, and the increase reached a value of approximately 0.100 m in some areas. Due to the continuous spalling of rock debris, the bottom surface of the side slope gradually increased in elevation, forming an increasingly large inclined surface, and when the continuous spalling exceeded the bearing range of the side-slope surface, material gradually started to pile up on the ground, as shown in Figure 10b. Therefore, although the time interval between the two periods of data collection was only 6 months, the rock mass of the side slope experienced unambiguous weathering during this time, which means that the side slope is not safe. There is a risk of rockfall or collapse of the side slope with near-vertical form and little vegetation cover.

DISCUSSION

The data acquisition aspects are as follows. TLS offers better performance in detecting small terrain displacements, but practical applications are very limited
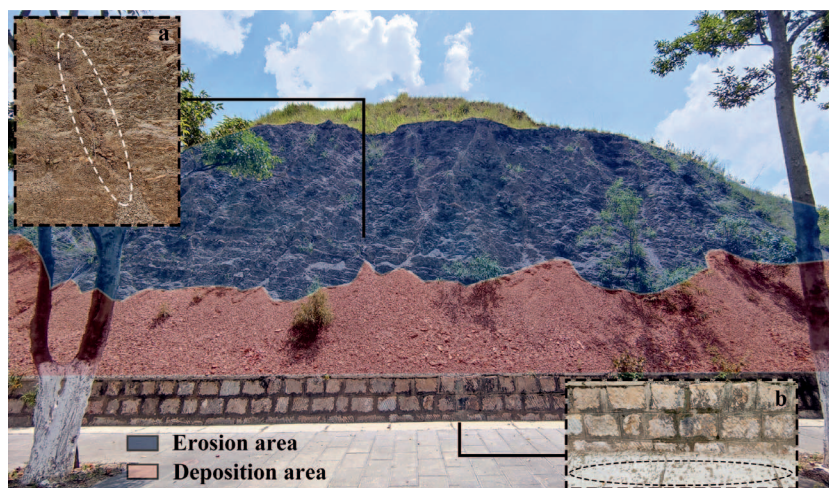
Figure 10. Side-slope surface and foot characteristics. (a) Cracks on the side-slope surface. (b) The debris on the side-slope surface begins to accumulate on the ground after it exceeds the tolerance range of the surface.

in some specific scenarios. In one study (Kovanič et al., 2020), the authors performed a large number of TLS measurements in a single day, and it was difficult to collect a complete point cloud without a data gap. Therefore, only the most likely deformation area of the side slope is usually measured by TLS to improve the work efficiency. At the same time, to a certain extent, the ground surface of the side slope covered by vegetation is captured by TLS, which provides more accurate results for surface deformation detection. In these areas, the point cloud provided by UAV-based photogrammetry is insufficient. UAV-based photogrammetry is relatively inexpensive and easy to implement, covering almost the entire area of the research object in a short period. The high-resolution topography of the entire area can be surveyed. In addition, UAVs have better applicability in a variety of environments, especially for slopes or landslide objects with large drops and inclinations. TLS usually has difficulty generating effective point clouds due to the lack of a suitable location, while side-slope information can be obtained by oblique photography, which can build a denser and higher quality photogrammetry point cloud, allowing the final TLS–UAV photogrammetry point cloud to provide slope deformation monitoring.

The GCPs contributed to the implementation of the method in this study. On the one hand, the accurate registration of TLS and UAV photogrammetry point clouds is the basis of point cloud integration and multitemporal deformation monitoring. The georeferences of the TLS point cloud and UAV photogrammetry point cloud are provided by the GCPs, thus avoiding the coarse matching process in the integrated point cloud. Moreover, the TLS and UAV photogrammetry point clouds that are to be registered are acquired in the same period. The main difference between the two is the spatial density of the point cloud, so the UAV photogrammetry point cloud can be approximated as a subset of the TLS point cloud. Therefore, the purpose of precise point cloud registration can be achieved by the ICP algorithm. On the other hand, GCPs are involved in the process of constructing dense point clouds from UAV images, which greatly reduces the elevation distortion of photogrammetry point clouds. In this article, the same GCPs were used for the UAV photogrammetry point clouds in both periods (Peppa et al., 2019). The positioning uncertainty error caused by RTK measurement was avoided to ensure the accuracy of the final deformation detection.

In addition, a gap-filling method was used to integrate UAV-based photogrammetry point clouds with the TLS point cloud in this study. The 3D terrain is described more realistically and orderly with this method than directly mixing two types of point clouds, and it reduces data redundancy, as shown in Figure 11. Clouds a and b show the differences between the gap-filling and integration method and the direct mixing method, with Cloud a and Cloud b converging in different ways based on Cloud 1. The purpose of supplementing data integrity can be achieved with both methods, but the accuracy of the TLS point cloud is reduced by the point cloud density of the UAV photogrammetry point cloud in Cloud b, which loses the surface details of the slope. A digital surface model (DSM) of Clouds a and b was built by creating a triangulated irregular network. The results show that directly mixing the UAV photogrammetry and TLS point clouds introduces more noise to the final DSM, while the gap-filling and integration method shows a smoother and more realistic result.
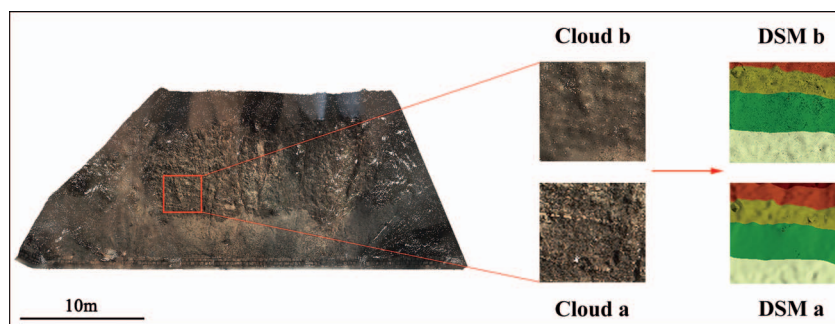
Figure 11. Comparison of point cloud integration methods. Cloud a and DSM a based on the filling and integration method (based on Cloud 1). Cloud b and DSM b based on direct mixing (based on Cloud 1).

In addition to side-slope monitoring, the proposed TLS and UAV photogrammetry point cloud integration scheme can be applied to a variety of geological applications. For example, terraces in agricultural landscapes are a special type of land use. They are distributed in steps along steep slopes, which can effectively improve the productivity of land in mountainous areas. Therefore, it is of great significance to record and observe the evolution of agricultural landscapes such as terraces to achieve sustainable development in mountainous areas (Capolupo et al., 2018; Mauri et al., 2021; and Pijl et al., 2021). However, terraces show some special morphological characteristics, such as the existence of vertical slopes and surfaces and sides usually covered with messy vegetation, and TLS is very difficult to perform on steep slopes. UAVs can easily acquire information on the top surface of terraces, but it is difficult to capture high-precision elevation information. Therefore, the proposed integration scheme can be effectively used for the construction of high-precision topographic data for terraced environments to facilitate their geomorphological and evolutionary analysis. Similarly, the proposed method can be applied to the geological investigation of slopes in open-pit mines, where, after a long service life, high and steep slopes are often generated, and the assessment of their stability state is relevant to the safety of operators (Tong et al., 2015; Esposito et al., 2017; and Bamford et al., 2020). Due to the scale and form of open-pit mines, TLS can usually only be performed at the bottom, which can obtain most of the side information of the mining area slope, while the UAV photogrammetry point clouds can supplement information in data shadow areas to build a 3D model of the open-pit mining area slope and further obtain information on the rock mass structural plane. In addition, the proposed method can be applied to postdisaster investigations and rapid road rescue work after earthquakes and landslides (Stringer et al., 2021). After a disaster, the harsh geological environment can generate great difficulties for the rescue and geological survey staff, and it is difficult for the investigators to reach the upper areas of slopes and landslides. At this time, a UAV can make use of its fast and flexible characteristics to achieve large-scale rapid modeling of disasters and their surrounding areas, while TLS can be applied to specific main areas on slopes and landslides. Through the effective integration of the two, efficiency and accuracy can be balanced, and after characterizing the basic condition of the surrounding area, zoning, dangerous rock positioning, and structural surface yield measurements can be effectively carried out for the main area of the disaster, providing basic data about the geological disaster and providing a scientific basis for emergency decision-making.

CONCLUSION

Solutions for deformation monitoring in special side-slope environments were explored in this study. To overcome the limitations of a single measurement method and consider the particularity of the terrain environment, UAV-based photogrammetry and TLS point cloud data sets were combined to create an integrated data set. The integrated TLS–UAV photogrammetry method was proven to be an effective method with high acquisition efficiency, high spatial resolution, and complete reconstruction of side slopes. In this method, precise 3D point clouds of the key area of the side slope are measured by TLS, which removes the need to reposition the station multiple times and thus reduces the field workload. The data gaps in the TLS point cloud and the rest of the target slope are measured by UAV-based photogrammetry, which improves operational efficiency. Ultimately, the UAV photogrammetry point cloud fills in the gaps in the TLS point cloud to generate a data set that covers the target slope completely. Based on the two phases of integrated point cloud data, the deformation variables and deformation zones on the side slope can be successfully detected, which provides an important reference for the current state assessment of side slopes.

ACKNOWLEDGMENTS

REFERENCES

ABELLÁN, A.; OPPIKOFER, T.; JABOYEDOFF, M.; ROSSER, NJ.; LIM, M.; AND LATO, M. J., 2014, Terrestrial laser scanning of rock slope instabilities: *Earth Surface Processes and Landforms*, Vol. 39, No. 1, pp. 80–97.

ALI, M.; TAHA, L.; MOHAMED, M.; AND MANDOUH, A. A., 2021, Generation of digital terrain model from multispectral LiDAR using different ground filtering techniques: *Egyptian Journal of Remote Sensing and Space Science*, Vol. 24, No. 2, pp. 181–189.

BALSA-BARREIRO, J. AND FRITSCH, D., 2018, Generation of visually aesthetic and detailed 3D models of historical cities by using laser scanning and digital photogrammetry: *Digital Applications in Archaeology and Cultural Heritage*, Vol. 8, pp. 57–64.

BAMFORD, T.; MEDINAC, F.; AND ESMAEILI, K., 2020, Continuous monitoring and improvement of the blasting process in open pit mines using unmanned aerial vehicle techniques: *Remote Sensing*, Vol. 12, No. 17, 2801.

BESL, P. J. AND MCKAY, H. D., 1992, A method for registration of 3-D shapes: *IEEE Transactions on Pattern Analysis & Machine Intelligence*, Vol. 14, No. 2, pp. 239–256.

BONNEAU, D. A. AND HUTCHINSON, D. J., 2019, The use of terrestrial laser scanning for the characterization of a cliff-talus system in the Thompson River Valley, British Columbia, Canada: *Geomorphology*, Vol. 327, pp. 598–609.

BRÜCKL, E.; BRUNNER, F. K.; AND KRAUS, K., 2006, Kinematics of a deep-seated landslide derived from photogrammetric, GPS and geophysical data: *Engineering Geology*, Vol. 88, No. 3–4, pp. 149–159.

CAPOLUPO, A.; KOOISTRA, L.; AND BOCCIA, L., 2018, A novel approach for detecting agricultural terraced landscapes from historical and contemporaneous photogrammetric aerial photos: *International Journal of Applied Earth Observation and Geoinformation*, Vol. 73, pp. 800–810.

CAREY, J. A.; PINTER, N.; PICKERING, A. J.; PRENTICE, C. S.; AND DELONG, S. B., 2019, Analysis of landslide kinematics using multi-temporal unmanned aerial vehicle imagery, La Honda, California: *Environmental & Engineering Geoscience*, Vol. 25, No. 4, pp. 301–317.

DELANEY, R. K.; SHAKOOR, A.; AND WATTS, C. F., 2020, Evaluating the use of unmanned aerial systems (UAS) for collecting discontinuity orientation data for rock slope stability analysis: *Environmental & Engineering Geoscience*, Vol. 26, No. 4, pp. 427–447.

DEWITTE, O.; JASSELETTE, J. C.; CORNET, Y.; VAN DEN EECKHAUT, M.; COLLIGNON, A.; POESEN, J.; AND DEMOULIN, A., 2008, Tracking landslide displacements by multi-temporal DTMs: A combined aerial stereophotogrammetric and LIDAR approach in western Belgium: *Engineering Geology*, Vol. 99, No. 1–2, pp. 11–22.

DIFRANCESCO, P. M.; BONNEAU, D.; AND HUTCHINSON, D. J., 2020, The implications of M3C2 projection diameter on 3D semi-automated rockfall extraction from sequential terrestrial laser scanning point clouds: *Remote Sensing*, Vol. 12, No. 11, 1885.

ESPOSITO, G.; MASTROROCCO, G.; SALVINI, R.; OLIVETI, M.; AND STARITA, P., 2017, Application of UAV photogrammetry for the multi-temporal estimation of surface extent and volumetric excavation in the Sa Pigada Bianca open-pit mine, Sardinia, Italy: *Environmental Earth Sciences*, Vol. 73, No. 3, pp. 1–16.

FERRERO, A. M.; MIGLIAZZA, M.; RONCELLA, R.; AND RABBI, E., 2010, Rock slopes risk assessment based on advanced geostructural survey techniques: *Landslides*, Vol. 8, No. 2, pp. 221–231.

FOURNIADIS, I. G.; LIU, J. G.; AND MASON, P. J., 2007, Landslide hazard assessment in the Three Gorges area, China, using ASTER imagery: *Wushan–Badong: Geomorphology*, Vol. 84, No. 1–2, pp. 126–144.

HOUT, R.; MALEVAL, V.; MAHE, G.; ROUVELLAC, E.; CROUZEVIALLE, R.; AND CERBELAUD, F., 2020, UAV and LiDAR data in the service of bank gully erosion measurement in Rambla de Algeciras lakeshore: *Water*, Vol. 12, No. 10, 2748.

JAMES, M. R.; CHANDLER, J. H.; ELTNER, A.; FRASER, C.; MILLER, P. E.; MILLS, J. P.; NOBLE, T.; ROBSON, S.; AND LANE, S. N., 2019, Guidelines on the use of structure-from-motion photogrammetry in geomorphic research: *Earth Surface Processes and Landforms*, Vol. 44, No. 10, pp. 2081–2084.

KOVANIČ, L'.; BLISTAN, P.; URBAN, R.; ŠTRONER, M.; BLIŠŤANOVÁ, M.; BARTOŠ, K.; AND PUKANSKÁ, K., 2020, Analysis of the suitability of high-resolution DEM obtained using ALS and UAS (SfM) for the identification of changes and monitoring the development of selected geohazards in the alpine environment—A case study in High Tatras, Slovakia: *Remote Sensing*, Vol. 12, No. 23, 3901.

LAGUE, D.; BRODU, N.; AND LEROUX, J., 2013, Accurate 3D comparison of complex topography with terrestrial laser scanner: Application to the Rangitikei canyon (NZ): *ISPRS Journal of Photogrammetry and Remote Sensing*, Vol. 82, pp. 10–26.

LAZZARI, M. AND GIOIA, D., 2017, UAV images and historical aerial-photos for geomorphological analysis and hillslope evolution of the Uggiano medieval archaeological site (Basilicata, southern Italy): *Geomatics, Natural Hazards and Risk*, Vol. 8, No. 1, pp. 104–119.

LIU, C.; LIU, X.; PENG, X.; WANG, E.; AND WANG, S., 2019, Application of 3D-DDA integrated with unmanned aerial vehicle–laser scanner (UAV-LS) photogrammetry for stability analysis of a blocky rock mass slope: *Landslides*, Vol. 16, No. 9, pp. 1645–1661.

MAURI, L.; STRAFFELINI, E.; CUCCHIARO, S.; AND TAROLLI, P., 2021, UAV-SfM 4D mapping of landslides activated in a steep terraced agricultural area: *Journal of Agricultural Engineering*, Vol. 52, No. 1.

PAN, Z.; ZHOU, Y.; ZHAO, C.; HU, C.; ZHOU, H.; AND FAN, Y., 2019, Assessment method of slope excavation quality based on point cloud data: *KSCE Journal of Civil Engineering*, Vol. 23, No. 3, pp. 935–946.

PASSALACQUA, P.; BELMONT, P.; STALEY, D. M.; SIMLEY, J. D.; ARROWSMITH, J. R.; BODE, C. A.; CROSBY, C.; DELONG, S. B.; GLENN, N. F.; KELLY, S. A.; LAGUE, D.; SANGIREDDY, H.; SCHAFFRATH, K.; TARBOTON, D. G.; WASKLEWICZ, T.; AND WHEATON, J. M., 2015, Analyzing high resolution topography for advancing the understanding of mass and energy transfer through landscapes: A review: *Earth-Science Reviews*, Vol. 148, pp. 174–193.

PEPPA, M. V.; MILLS, J. P.; MOORE, P.; MILLER, P. E.; AND CHAMBERS, J. E., 2019, Automated co-registration and calibration in SfM photogrammetry for landslide change detection: *Earth Surface Processes and Landforms*, Vol. 44, No. 1, pp. 287–303.

PIJL, A.; QUARELLA, E.; VOGEL, T. A.; D'AGOSTINO, V.; AND TAROLLI, P., 2021, Remote sensing vs. field-based monitoring of agricultural terrace degradation: *International Soil and Water Conservation Research*, Vol. 9, No. 1, pp. 1–10.

PITKÄNEN, T. P.; RAUMONEN, P.; AND KANGAS, A., 2019, Measuring stem diameters with TLS in boreal forests by complementary fitting procedure: *ISPRS Journal of Photogrammetry and Remote Sensing*, Vol. 147, pp. 294–306.

RANA, P.; KORHONEN, L.; GAUTAM, B.; AND TOKOLA, T., 2014, Effect of field plot location on estimating tropical forest aboveground biomass in Nepal using airborne laser scanning data: *ISPRS Journal of Photogrammetry and Remote Sensing*, Vol. 94, pp. 55–62.

RODRIGUEZ, J.; MACCIOTTA, R.; HENDRY, M. T.; ROUSTAEI, M.; GRÄPEL, C.; AND SKIRROW, R., 2020, UAVs for monitoring, investigation, and mitigation design of a rock slope with multiple failure mechanisms—A case study: *Landslides*, Vol. 17, No. 9, pp. 2027–2040.

ŠAŠAK, J.; GALLAY, M.; KAŇUK, J.; HOFIERKA, J.; AND MINÁR, J., 2019, Combined use of terrestrial laser scanning and UAV photogrammetry in mapping alpine terrain: *Remote Sensing*, Vol. 11, No. 18, 2154.

SCOTT, A.; MARK, J. V.; AND COLE, C., 2020, *Advances in Unstable Slope Instrumentation and Monitoring*: The National Academies Press, Washington, D.C.

SIBSON, R., 1981, A brief description of natural neighbor interpolation. In Barnett, V. (Editor), *Interpreting Multivariate Data*: John Wiley and Sons, New York, pp. 21–36.

SON, S. W.; KIM, D. W.; SUNG, W. G.; AND YU, J. J., 2020, Integrating UAV and TLS approaches for environmental management: A case study of a waste stockpile area: *Remote Sensing. Vol.* 12, No. 10, 1615.

STRINGER, J.; BROOK, M. S.; AND JUSTICE, R., 2021, Post-earthquake monitoring of landslides along the Southern Kaikōura Transport Corridor, New Zealand: *Landslides*, Vol. 18, No. 1, pp. 409–423.

TONG, X.; LIU, X.; CHEN, P.; LIU, S.; LUAN, K.; LI, L.; LIU, S.; LIU, X.; XIE, H.; AND JIN, Y. J. R. S., 2015, Integration of UAV-based photogrammetry and terrestrial laser scanning for the three-dimensional mapping and monitoring of open-pit mine areas: *Remote Sensing*, Vol. 7, No. 6, pp. 6635–6662.

WANG, S.; ZHANG, Z.; REN, Y.; AND ZHU, C., 2019, UAV photogrammetry and AFSA-Elman neural network in slopes displacement monitoring and forecasting: *KSCE Journal of Civil Engineering*, Vol. 24, No. 1, pp. 19–29.

WATSON, D., 2013 *Contouring: a guide to the analysis and display of spatial data*. Elsevier.

WESTOBY, M. J.; BRASINGTON, J.; GLASSER, N. F.; HAMBREY, M. J.; AND REYNOLDS, J. M., 2012, 'Structure-from-motion' photogrammetry: A low-cost, effective tool for geoscience applications: *Geomorphology*, Vol. 179, pp. 300–314.

ZHANG, K.; SHENG, Y.; WANG, M.; AND FU, S., 2018, An enhanced multi-view vertical line locus matching algorithm of object space ground primitives based on positioning consistency for aerial and space images: *ISPRS Journal of Photogrammetry and Remote Sensing*, Vol. 139, pp. 241–254.

ZHANG, W.; QI, J.; WAN, P.; WANG, H.; XIE, D.; WANG, X.; AND YAN, G., 2016, An easy-to-use airborne LiDAR data filtering method based on cloth simulation: *Remote Sensing*, Vol. 8, No. 6, 501.

Technical Note

Terms Related to Annual Frequency for Probabilistic Assessments

JEFFREY R. KEATON*

WSP USA, 4600 E Washington St, Phoenix, AZ 85034

Probabilistic assessments are used to quantify many hazardous processes in terms of frequency of occurrence of events of different sizes occurring within specified areas. Hazardous processes quantified in this manner include flood levels at locations along river channels, earthquakes of varying magnitudes within the proximity of population centers, eruptive events at active volcanoes, tsunami runup at coastal locations, heavy precipitation events at specific locations, and many others. The terms annual frequency (AF), annual exceedance probability (AEP), exceedance probability (EP), and average return period (ARP, sometimes called the mean recurrence interval) are related. Both AEP and EP represent the probability that an event equal to or larger than a certain size will occur during a specified period of time, but the specified period for AEP is restricted to 1 year. The difference between the two results lies in the way that outcome and time are considered in the model (Crovelli, 2000); outcomes considered in a discrete time period (i.e., 1 year, or largest flood at a point on a river in a given year) follow a binomial probability model, whereas outcomes aggregated over a continuous time period follow a Poisson probability model (e.g., earthquakes of M > 5 since 1974 with epicenters within 100 km of a specific location). The differences between the two model results are relatively minor, especially considering the uncertainty involving in understanding the details of the hazardous processes. Crovelli (2000) points out that nature is not random because natural events occur for physical reasons (e.g., a flood reaching elevation X at point Y along a river channel), but the reasons are too complex or poorly understood to be modeled deterministically. Randomness, therefore, is a necessary assumption of probability models.

For this discussion, EP = AF for a 1-year time period, t (i.e., AEP); otherwise, EP is attached to the time period of the analysis (e.g., 50-year EP). AF = (number)/year = year^{-1} and ARP = 1/AF are directly related and are plotted as reciprocal values, with the axes labeled on both the bottom and top of the graph in Figure 1. Four pairs of lines are plotted in Figure 1 representing four time periods of interest: $t = 1$, 10,

50, and 100 years. The binomial and Poisson model results are plotted as broken black lines and solid red lines, respectively. The binomial plot for $t = 1$ year is a straight line with a slope of -1 in log-log space (Figure 1) that has identical values on the EP and AF axes and reciprocal values on the ARP axis. The exceedance probability for at least one flood in t years (EP(t)) with a given probability in any one year (i.e., annual frequency or AF expressed as ARP) for the binomial distribution is

$$EP(t) = 1 - (1 - AF)^t; \ ARP \geq 1 \qquad (1)$$

$$AF = 1 - (1 - EP(t))^{1/t}; \ AF \leq 1 \qquad (2)$$

where t is the time period of interest, sometimes called exposure time, and ARP is the average return period that must be greater than or equal to 1 year. For $t = 1$, EP(t) = AF. By inspection, it can be seen in Eq. 1 that when ARP = 1, AF = 1 and EP(t) = 1; however, if ARP < 1, then AF > 1 and EP(t) > 1, which is disallowed in probability models that range from 0 to 1. Therefore, the broken black line representing EP(1) in Figure 1 terminates at EP(t) = AF = ARP = 1 for the binomial probability. For periods of interest $t > 1$, EP(t) approaches 1.

Using the same terms as in the binomial probability model, the Poisson probability model is

$$EP(t) = 1 - \exp(1 - (1/ARP) \times t)$$
$$= 1 - exp(-AF \times t) \qquad (3)$$

$$AF = (-\ln[1 - EP(t)])/t \qquad (4)$$

where exp($\cdot$) represents the base of Napierian logarithms, e, raised to the power of the value inside the parentheses and ln[$\cdot$] is the natural logarithm of the value inside the square parentheses. The Poisson probability model is not restricted by ARP and returns values for EP(t) that approach 1 for ARP < 1 (red line in Figure 1).

The difference between the binomial result and the Poisson result for $t = 1$ year for values of ARP between about 0.2 and 10 years is visible in log-log space, but as ARP exceeds 10 years, the lines appear to be superimposed (Figure 1, broken black and solid red lines for $t = 1$ year). For longer periods of interest, $t = 10$, 50,

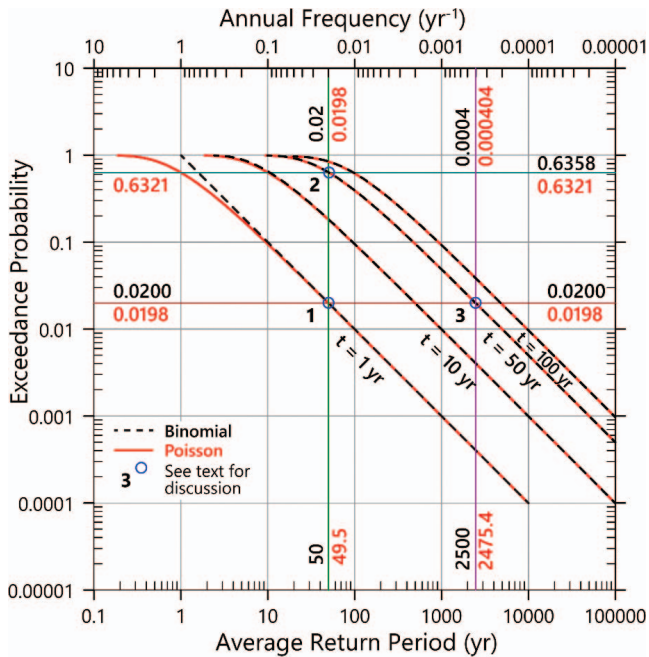*Corresponding author email: jeff.keaton@wsp.com

Figure 1. Comparison of binomial probability model (black numbers and broken black lines) and Poisson probability model (red numbers and solid red lines).

and 100 years, the broken black and solid red lines appear to be superimposed as they become asymptotic to EP = 1. The three blue circles numbered 1, 2, and 3 serve to illustrate the region bounded by (EP = 0.02, ARP = 50), (EP = 0.636, ARP = 50), and (EP = 0.02, ARP = 2,500), respectively. The green, dark red, teal, and purple lines intersect in the blue circles.

At point 1 in Figure 1, AF = 0.02000 when EP = 0.02 and $t = 1$ in the binomial model (Eq. 2); however, EP = 0.0198 when AF = 0.020 and $t = 1$ in the Poisson model (Eq. 3). Furthermore, AF = 0.0198 for EP = 0.02 and $t = 1$ values in the Poisson model (Eq. 4), and ARP = 49.5 when AF = 0.0200 and AF = 0.0198 when ARP = 50.0.

Point 2 in Figure 1 is on the curve for $t = 50$ years where it intersects with the line connecting ARP = 50 years; EP = 0.6358 is on the binomial line, indicating that the so-called 50-year flood (ARP = 50) has an ~63.6 percent chance of occurring at least once during an average 50-year period of time. EP = 0.632 is on the Poisson line at ARP = 50, which is slightly lower than the binomial line. Note that the line representing EP = 0.6358 intersects the curves for $t = 10$, 50, and 100 years at AF = 0.1, 0.02, and 0.01, respectively, which is the same as ARP = 10, 50, and 100.

Point 3 in Figure 1 is on the $t = 50$ years curve at EP = 0.02. This is the exceedance probability term that was used for earthquake ground motion in the International Building Code (IBC, 2000). The intersection of

EP = 0.02 with the binomial curve for $t = 50$ years corresponds with ARP = 2,500 and AF = 0.0004. However, EP = 0.02 intersects with the Poisson curve for $t = 50$ years at ARP = 2,475.4 and at AF = 0.000404 when ARP = 2,500.

In statistical analyses for codes and insurance purposes, earthquakes are treated differently than floods. All earthquakes of approximately magnitude 5 have some potential to begin to cause some damage to reasonably well-constructed buildings on stable sites; therefore, earthquakes are modeled with Poisson statistics for hazard characterization and design provisions in building codes. Additionally, earthquakes can occur as foreshocks, main shocks, and aftershocks. From an insurance perspective, damage to a building from a mainshock would be covered by earthquake insurance policies. Well-constructed buildings might suffer minor damage in a mainshock but be more severely damaged by smaller magnitude aftershocks because of the minor damage caused by the mainshock. Floods are analyzed for administration of flood insurance purchased with annual premiums; therefore, only the most severe inundation hazard with a specific annual likelihood of occurrence at particular locations along river channels is what needs to be characterized. The likelihood of lower levels of inundation is irrelevant for flood insurance.

The flooding studies in the United States typically refer to Federal Emergency Management Agency flood insurance rate maps (FEMA, 2020) as the basis for flood insurance in the United States as areas that are subject to inundation by floods that have a 1 percent chance of being equaled or exceeded during any given year. This inundation chance of EP = 0.01 and $t = 1$ corresponds to ARP = 100 and AF = 0.01 with the binomial model and ARP = 99.5 and AF = 0.01005 with the Poisson model.

Crovelli (2000) describes the Poisson probability model as a first-approximation model and the binomial probability model as an approximation of an approximation. The level of uncertainty in the inputs to extreme flooding incidences suggests that the two models are considered essentially equivalent. While the Poisson model may be more precise, the binomial model has a characteristic that is helpful in communicating exceedance probabilities and average return periods as reciprocals. In other words, a probability of 2 percent in 50 years corresponds to a 2,500-year average return period in the binomial model, rather than a 2,475.4-year return period, as it does in the Poisson model.

REFERENCES

CROVELLI, R. A., 2000, *Probability Models for Estimation of Number and Costs of Landslides*: U.S. Geological

Survey Open-file Report 00-240: Electronic document, available at https://pubs.usgs.gov/of/2000/ofr-00-0249/ProbModels.html

FEDERAL EMERGENCY MANAGEMENT AGENCY (FEMA), 2020, *Flood Insurance Rate Maps*: Electronic document, available at https://www.fema.gov/sites/default/files/2020-07/how-to-read-flood-insurance-rate-map-tutorial.txt

INTERNATIONAL BUILDING CODE (IBC), 2000, *International Building Code 2000*: Electronic document, available at https://codes.iccsafe.org/content/IBC2000

Comment & Reply

Comment on: Association between COVID-19 and Heavy Metal Pollution in Iraqi Cities Determined from Hierarchical Prediction

IRA D. SASOWSKY*

Department of Geosciences, University of Akron, Akron, OH 44325-4101

I recently read the paper "Association between COVID-19 and Heavy Metal Pollution in Iraqi Cities Determined from Hierarchical Prediction" by Aram Mohammed Raheem in the November *Environmental & Engineering Geoscience* issue. It appears to me that the approach used has two fatal flaws (items one and two below) and two major concerns (items three and four) and that the conclusions are not supported by the data. I describe my concerns below, keeping in mind the stated conclusion:

> Based on the results of the proposed statistical models, there is a positive linear relationship between confirmed and death COVID-19 cases with the different types of heavy metal distribution. This indicates that increasing any type of heavy metal concentration beyond the allowable upper limit may result in increasing COVID-19 confirmed and death cases.

1) The crux of the paper is given in Figures 6 and 7, where the author plots cumulative contaminant concentration versus cumulative COVID deaths (both as percentages). It is never valid to make this kind of plot, as it will always show a *false correlation.* As an example, I used a random number generator to create two strings of numbers between 1 and 200, placed these in an Excel sheet, and labeled them "deaths" and "metals." I made a scatter plot of them, and then I created running summations for the values, as the author did with his data, and plotted them against each other. The result is Figure R1, which shows an *r* correlation of 0.98 between these two random sets of numbers when plotted as the cumulative percentage (right-hand graph) and how they would look as a scatter plot (left-hand graph, no correlation).

A more appropriate plot would simply be a scatter plot of the raw data. However, when this is made, using data the author provided for cadmium (Figure R2), it can be seen there is no significant relationship. The conclusions are not supported.

2) The data on heavy metals used are not representative of the regions, at least in many of the cases. They are taken from specifically contaminated sites. It is inappropriate to take data from a specific contamination site and interpret it as being representative of a whole region. Therefore, even if an appropriate statistical method had been applied, and a correlation found, the conclusions would be suspect.

3) There is no documentation that COVID cases *could* be affected by exposure to metals (even though the author states, "This model is based on the fact that the increase in heavy metal contamination can increase the rate of death resulting from reduced human body resistance," without any citation).

4) The title of the article states that a hierarchical prediction is used. I see no evidence of this in the manuscript. Even if it had been used, no utility would be obtained due to the problems listed above.

Beyond the inappropriateness of using contamination data from specific industrial sites to draw conclusions about entire counties, the use of the data sums in the final graphs (which are the crux of the paper) is erroneous; therefore, the conclusions are invalid. There is not a demonstrated link between pollution and COVID cases.
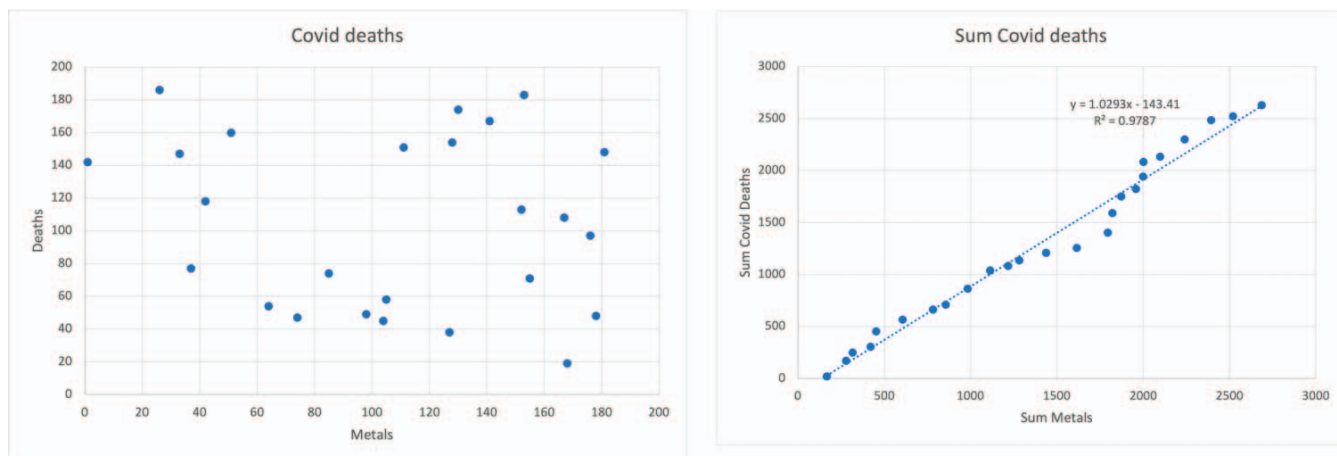
*Corresponding author email: ids@uakron.edu

Figure R1. Demonstration of how a false correlation will result if instead of cross-plotting two variables (left), the sum of values is plotted (right).
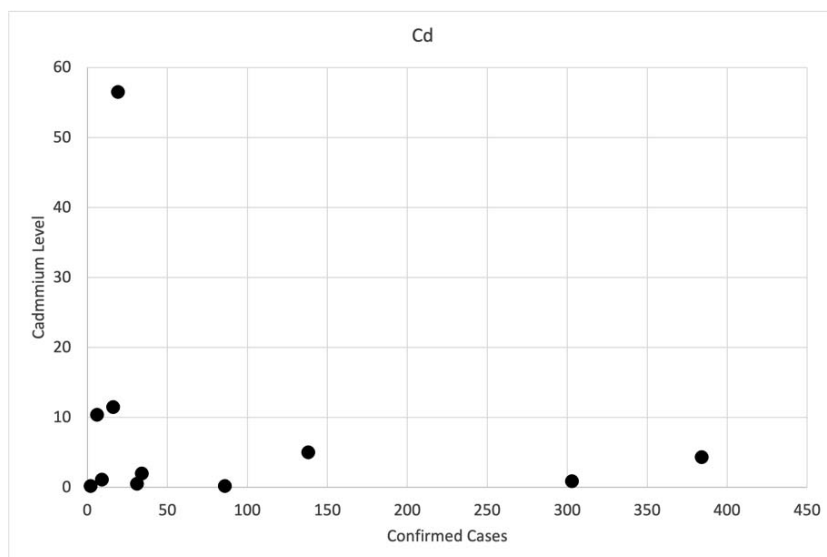

Figure R2. Scatter plot of the author's cadmium data. No correlation; the conclusions of the paper are unsupported.

Reply to Comment on: *Association between COVID-19 and Heavy Metal Pollution in Iraqi Cities Determined from Hierarchical Prediction*

ARAM MOHAMMED RAHEEM*

University of Kirkuk, Iraq

I thank you for this concern regarding my COVID-19 paper. To clarify this concern, several points should be stated as follows:

*Corresponding author email: engaram@yahoo.com; aram_raheem@uokirkuk.edu.iq

1) The data used in the published paper are real data, not random data, and they were collected from original sources.
2) The main principle of this paper is that when there are two humans, one is weak (exposed to heavy metal contamination) and the other is strong (no heavy metal contamination), and both of them are

attacked by the COVID-19 virus, then the first human is expected to get hurt more than the second one. This is logic, and it was verified in the used statistical model.

3) Any statistical model should be built based on logic expectations and depend on real data, and these conditions were satisfied in the used model.

4) The paper has been reviewed by anonymous experts in the field of the study, and their questions have been answered accordingly.

5) To justify any concern about the used statistical model or about the concept, I encourage the writer of the letter to perform a field investigation about the real cases of humans with and without heavy metal contamination who are exposed to the COVID-19 virus. Then, a manuscript can be written discussing the concept, criticizing this statistical model or any other models, and probably coming up with a better model. Indeed, I will be more than happy to read and get the benefit of such a possible written manuscript.

I thank the editorial board, and I do respect any decision that will be made regarding my published paper.